Oxidation of Two Different Pt-Aluminised Bond Coats

By

Friederike Schennach

A thesis submitted to the University of Birmingham

for the degree of

Doctor of Philosophy

School of Metallurgy and Materials

College of Engineering and Physical Sciences

University of Birmingham

January 19, 2012

Acknowledgements

Many thanks go to my supervisors Prof. Ian P. Jones and Prof. Hugh E. Evans who always provided help and guidance, throughout my work on this thesis.

Special thanks go to Dr. Mary Taylor, who's advice, encouragement and support was invaluable.

I'd also like to thank my former colleagues in the High Temperature Oxidation group Dr. Ryan Jackson, Dr. Ian Edmunds and Dr. William Pragnall for thier advice and help around the lab, when I first started out.

Thanks also go to Paul Stanley and Ming Chu for the training they provided for the use of SEMs and TEMs, as well as to Dr. Goeff West from Loughbourough University for his help in producing TEM samples.

This work was funded by the Austrian Academy of Science (ÖAW) in form of a DocfForte studentship.

And last but not least I'd like to thank my parents and my partner Andreas Hörzig. Without their continued support and encouragement, I could not have done it.

Contents

List of Figures

List of Tables

Abstract

Two different Pt-aluminised bond coats, with varying thicknesses and Pt-contents were examined, regarding the influence of bond coat phases on the oxide growth.

This was done in a series of short term (3, 7 and 10 minutes) oxidation experiments at 1100°C. These clearly showed different types of oxide growing on γ-Ni3Al and β-NiAl phases in the low Pt specimens. It could also be shown that the transition from β-NiAl to γ-Ni3Al already occurs at these early stages of oxidation. On the high Pt specimens the same types of oxide are growing on γ-Ni3Al and ξ-PtAl2.

In addition, the high Pt specimens were examined after longer times at temperature (up to 100 hours), to gain information on the bond coat phase transformations happening at high platinum contents.

It could be shown that the chromium content plays an important role with regards to phase stability fields in the ternary Ni-Al-Pt diagram. Oxidation kinetics on these samples show that the oxide is not growing at a parabolic rate, but is characterized by a time exponent of 0.145, which may be attributed to a θ to α a transformation in the oxide.

Chapter 1

Introduction

In many modern industries high temperature enduring materials are used e.g. in the automotive, power generator and aerospace industries. The materials need to survive temperatures above 1000°C and, in the case of engines, thermal cycles. Apart from temperature, corrosion is a severe problem as well as stress. Nickel based super alloys nevertheless are designed to have high creep strength and long lifetime, rather then a good oxidation resistance. The latter is increased by the use of coatings.

The materials used in this study are widely used in various applications, mainly as overlay coatings on high-temperature alloys or as bond coats within thermal barrier coatings. They form a protective alumina layer which grows predominantly by ionic diffusion along oxide grain boundaries. The growth rate of the layer, thus, depends on its microstructure and is expected to increase with decreasing high-angle oxide grain boundaries. High oxide growth rates, either generally or locally, will prejudice the integrity of the coating system by leading to enhanced consumption of aluminium from the coating reservoir and/or to premature spallation of the protective oxide layer.

In the as-produced state, the coating is single-phase, polycrystalline β-(Ni,Pt)Al but, with continued oxidation and aluminium depletion, the structure will become duplex, consisting of blocky β and γ' phases.

The aim of this work was to gain a better understanding of the early stages of oxi-

dation of Pt-aluminised bond coats and the role of platinum. This was investigated by using 2 sets of specimens with different platinum content. One part of the research was done to investigate the influence of the underlying bond coat phases, β and γ', on the oxide formation in short term oxidation experiments. The other part involved a series of experiments with increasing times at temperature, to investigate the behaviour of Pt-aluminised bond coats with a high platinum content. This was done in order to gain information on the oxidation kinetics of high Pt coatings, as well as phase stability and transformation of bond coat phases.

Chapter 2

Literature Review

2.1 Oxidation

Oxidation is the reaction of a metal (M) with oxygen (O) to form an oxide, thus:

$$xM + \frac{y}{2}O_2 = M_xO_y \tag{2.1}$$

There are many factors which influence the oxidation behaviour of a metal, such as temperature, oxygen pressure, reaction rates and kinetics and the properties of the oxide scale forming on the metal surface [3].

Initial oxidation takes place by the adsorption of oxygen onto the metal surface, a process that is later followed by diffusion.

In the following chapters, these factors and processes are discussed in more detail.

2.1.1 Thermodynamics

According to the laws of thermodynamics a reaction only proceeds according to a change in free energy (ΔG) [3, 1]

ΔG is given by:

$$\Delta G = \Delta G^{\circ} - RTlnK \tag{2.2}$$

where ΔG° is the standard free energy change, R the gas constant, T the temperature in Kelvin and K is the equilibrium constant.

If we take the general equation for oxide formation (2.1) and apply it to the law of mass action, we get

$$K = \frac{a_{m_x Oy}}{a^x{}_m a^{\frac{y}{2}}{}_{O_2}} \Rightarrow \frac{a_{m_x Oy}}{a^x{}_m p^{\frac{y}{2}}_{O_2}} \tag{2.3}$$

where a is the activity and P_{O2} the oxygen partial pressure. [3]

In the case of oxide and metal both being solid, a_M and $a_{M_x O_y}$ can be considered unity and the equation can be reduced to

$$K = 1/(p_{O_2})^{\frac{y}{2}} \tag{2.4}$$

We can therefore substitute this for the equilibrium constant in the free energy equation (2.2), which gives

$$\Delta G = \Delta G^{\circ} - RTln\left[\frac{1}{(p_{O_2})^{\frac{y}{2}}}\right] \tag{2.5}$$

In the case of the reaction being at equilibrium, i.e. $\Delta G=0$, the equation can be transformed to

$$\Delta G^{\circ} = RTln\left[\frac{1}{(p_{O_2})^{\frac{y}{2}}}\right] \tag{2.6}$$

and so, the dissociation pressure, $p^*{}_{O_2}$, is given as:

$$p^*{}_{O_2} = exp\left[-\frac{2\Delta G^{\circ}}{yRT}\right] \tag{2.7}$$

In order to compare the oxide formation of different materials, plotting the standard free energy of formation (ΔG°) versus temperature proved useful. This is done in an Ellingham diagram (see figure 2.1) where ΔG° is expressed as kJ mol^{-1} O_2. Therefore oxide stabilities can be compared directly. [3]

The ${p^*}_{O_2}$ values for a certain material can be obtained directly from the diagram by drawing a straight line from the origin marked O, through the free energy line of said material at the temperature of interest, to the scale labelled P_{O2} on the diagram. The same can be done for the pressure ratio H_2/H_2O by drawing a line from the origin H to the scale labelled H_2/H_2O and the equilibrium CO/CO_2 ratio by drawing a line from the origin C to the CO/CO_2 scale.

Other diagrams often used in corrosion research include:

(1) Gibbs free energy versus composition and activity versus composition diagrams, both are used to describe the thermodynamics of solutions.

(2) Vapour-species diagrams, where the vapour pressure of a compound is shown as a function of a variable e.g. the partial pressure of a gaseous phase.

(3) Two-dimensional, isothermal stability diagrams which map stable phases, either in systems with one metallic and two reactive, non-metallic phases, or in systems with two metallic phases and one reactive, non-metallic phase.

(4) Three-dimensional, isothermal stability diagrams, which show the stable phases for a system with two metallic and two reactive, non-metallic components.

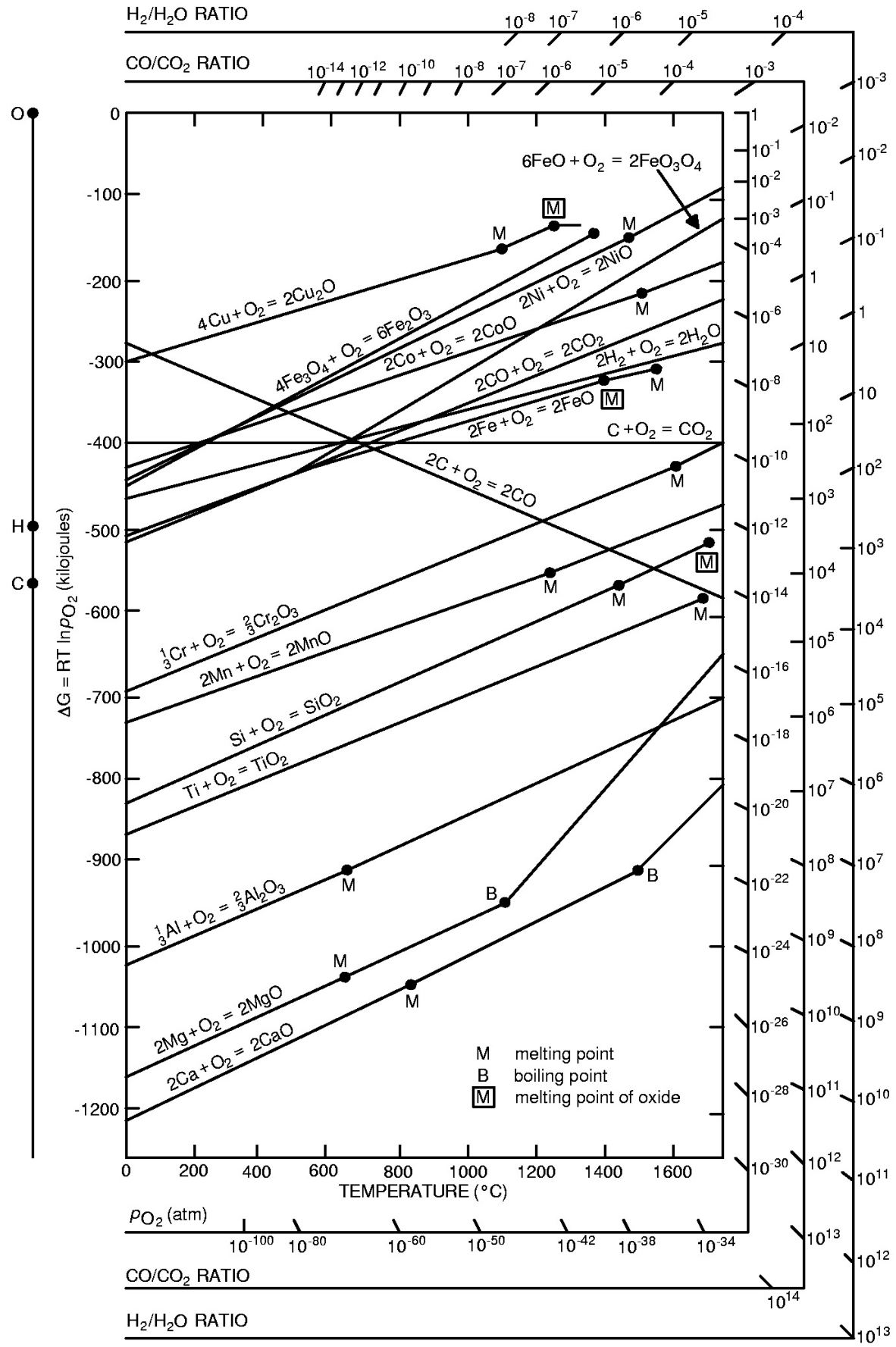

Figure 2.1: Ellingham Diagram, showing the standard free energy of formation as a function of temperature, for selected oxides [1].

2.1.2 Initial oxide formation

Adsorption

The accumulation of gas molecules onto the surface of a solid is called adsorption. This process is the initial step of any reaction between a metal and a gas. On a clean metal surface there is an average of 10^{15} adsorption sites per square centimeter. According to the kinetic gas theory [3] it would take about 2 seconds for a monolayer of adsorbed gas to form on a clean metal surface at room temperature and a gas pressure of 10^{-6} Torr. To obtain a clean surface the pressures would have to be considerably lower than 10^{-6} Torr. Therefore, unless performed in ultra high vacuum, all experiments on metal-gas reactions were made on surfaces that already had a thin oxide film or at least a layer of adsorbed gas before the start of the actual experiment.

Adsorption leads to a decrease of free energy, the adsorbed gas molecules or atoms lose a degree of freedom which also results in a decrease of entropy. A decrease in both free energy and entropy leads necessarily to a decrease in enthalpy, therefore adsorption is a exothermic process.

There are two different processes that fall under the term adsorption: physisorbtion and chemisorption. In the first one the gas is bound to the metal surface by physical or Van der Waal forces. In the second one the gas forms a chemical bond with atoms on the surface, therefore transferring electrons.

It is not always possible to distinguish between physical and chemical adsorption. One way of doing it is by looking at the heat produced by the reaction. For physisorption this is usually less than 10 kcal/mol, whereas for chemisorption it can amount up to more than 100 kcal/mol [3].

Also physical adsorption takes place without an activation energy and happens as soon as gas molecules or atoms impinge on the surface. Chemisorption on the other hand is

usually slower and needs an activation energy to proceed. It is also dependent on the crystallographic orientation of the surface phases, as well as edges, holes and defects. It usually only proceeds until a mono layer of gas is formed on the surface, where as physisorption may also produce multi layers.

Methods to study adsorption include flash desorption, field emission microscopy, field ion microscopy, low-energy electron diffraction, high-energy electron diffraction and infrared techniques.

Initial oxide formation

Oudar [2] formulated three steps of initial oxide formation (see figure 2.2):

(1) In a first step the surface is covered via chemisorption. As mentioned above this process usually stops when a continuous mono layer is formed.

(2) Epitaxial nuclei appear on the surface and start a lateral growth, until the surface is covered in nuclei.

(3) The oxide now starts a uniform growth over the entire surface.

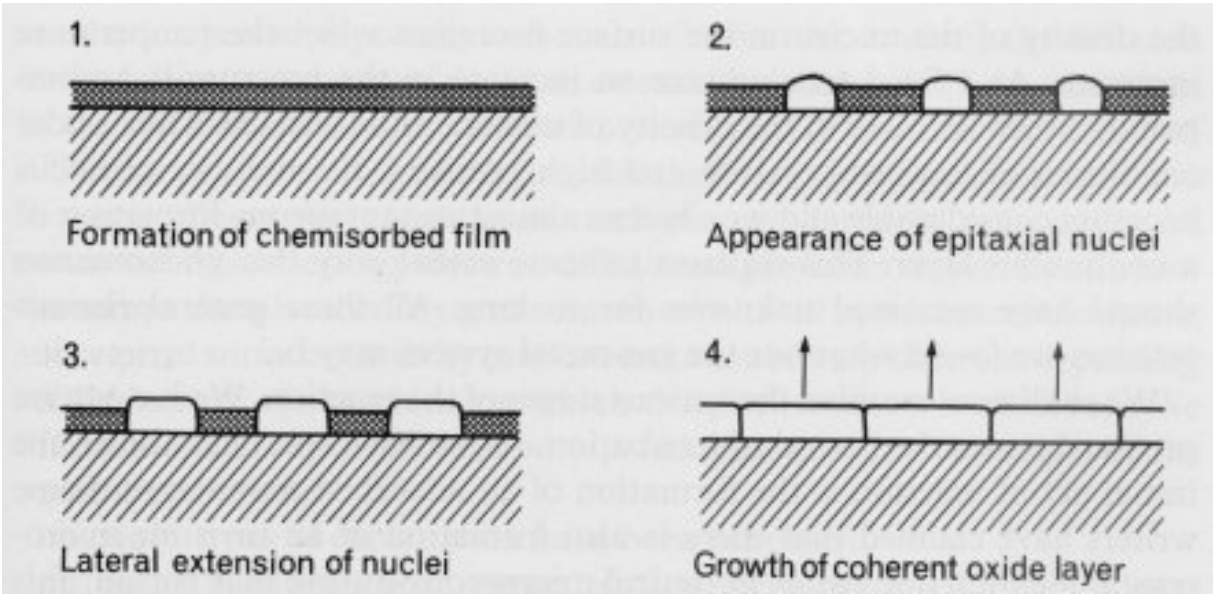

Figure 2.2: Stages of oxidation from first adsorption to a continuous layer [2]

2.1.3 Defect structures

Diffusion through solids occurs either along line and surface defects or through point defects in the oxide lattice.

Line and surface defects are grain boundaries and dislocations. Point defects include vacancies, misplaced atoms and interstitial atoms.

Point defects

Thermodynamics show that in a crystal above 0K, point defects will always occur. They both increase internal energy and entropy of the system. When the free energy of the system is at its minimum, the concentration of defects is in equilibrium. In principle all types of defects will be formed, but different systems and types will have different free energies of formation, therefore particular solids will have predominant defect types.

There are neutral and charged point defects. The latter are either positive (anion vacancies or cation interstitial ions) or negative (cation vacancies or anion interstitial ions for example. These charged point defects always come in pairs to ensure electron neutrality of the crystal.

Point defects in stoichiometric compounds

In stoichiometric crystals there are two major kinds of defects. To illustrate those the notations of Kröger [11] are used:

V_O: anion vacancy

V_M: cation vacancy

O_i: anion interstitial

M_i: cation interstitial

Schottky defects contain equal amounts of anion and cation vacancies (V_O and V_M) within the crystal, see figure 2.3.

The defect equilibrium for Schottky defects can be calculated thus:

$$nil \rightleftharpoons V_{\ddot{O}} + V''_M \tag{2.8}$$

Where nil stands for a perfect crystal, each dot indicates a positive charge, each prime sign a negative charge on the defects.

At a relatively small number of defects compared to the total number of lattice sites, the defect equilibrium can be written thus

$$N_{V\ddot{O}} * N''_{VM} = K_S \tag{2.9}$$

where $N_{V\ddot{O}}$ represents doubly charged anions and N''_{VM} represents doubly charged cations and K_S is the equilibrium constant.

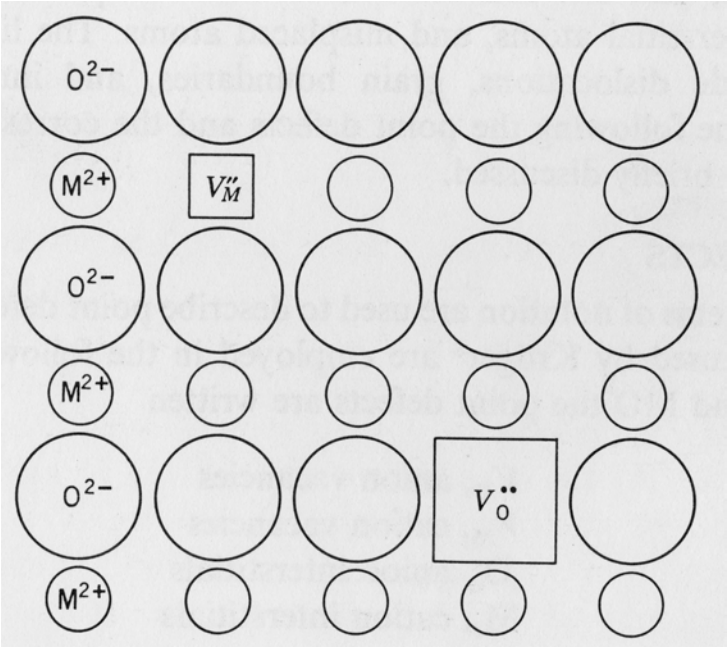

Figure 2.3: Schematic illustration of a Schottky defect structure [3]

With the relation

$$K_S = exp\left(\frac{-\Delta G_S}{RT}\right) = exp\frac{\Delta S_S}{R} exp\left(\frac{-\Delta H_S}{RT}\right) \tag{2.10}$$

K_S can be related to the molar free energy of formation of such a doubly charged defect (ΔG_S). Where ΔH_S is the molar enthalpy of formation and ΔS_S is the molar entropy of formation of the Schottky defect pairs.

Frenkel defects are limited either to the anion or cation lattice with pairs of vacancies and interstitial atoms for the same component ($V_O + O_i$ or $V_M + M_i$), see figure 2.4.

The equations for the formation of doubly charged Frenkel defect pairs in the cation lattice can be written thus

$$nil \rightleftharpoons M_i^{\cdot\cdot} + V_M'' \tag{2.11}$$

and for equilibrium

$$N_{M}{}_i^{\cdot\cdot} * N_{VM}'' = K_F = exp\left(\frac{-\Delta G_F}{RT}\right) = exp\frac{\Delta S_F}{R} exp\left(\frac{-\Delta H_F}{RT}\right) \tag{2.12}$$

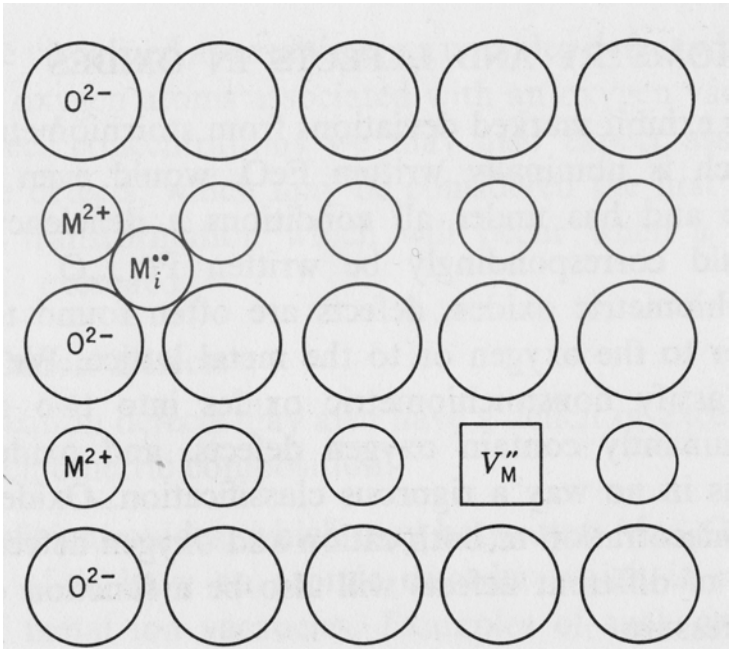

Figure 2.4: Schematic illustration of a Frenkel defect structure (Kofstad [3])

Non-stoichiometric compounds

Non-stoichiometry is usually associated with only one type of defect, therefore the electron neutrality of the crystal has to be obtained by the formation of complementary valence electrons or electronic defects. Oxides usually deviate strongly from stoichiometry, mostly their defects are either confined to the oxygen or to the metal lattice. They can therefore be roughly categorised as oxides with cation defects and oxides with anion defects. The temperature and partial pressure dependence of the components influences the extent of non-stoichiometry of a crystal. If we assume an oxygen deficient oxide, the non-stoichiometry reaction can be written as

$$MO \rightleftharpoons MO_{1-x} + \frac{x}{2}O_2^{(g)} \tag{2.13}$$

which shows that the non-stoichiometry in oxygen deficient oxides increases with decreasing oxygen pressure. In contrast the non-stoichiometry increases with increasing oxygen partial pressure for oxides with excess oxygen.

Oxides with Anion Defects

In the case of oxygen vacancies equation 2.13 can be transformed to

$$O_O \overset{K_1}{\rightleftharpoons} V_O^x + \frac{1}{2}O_2^{(g)} \tag{2.14}$$

where V_O^x stands for a neutral oxygen vacancy and K_1 is the equilibrium constant.

Electrical neutrality has to be maintained in a crystal, the removal of a doubly charged oxygen ion means that two negatively charged electronic defects or electrons have to be formed. A neutral oxygen vacancy can therefore be considered as a doubly charged oxygen vacancy with two trapped electrons, which can be freed:

$$V_O^x \overset{K_a}{\rightleftharpoons} V_{\dot{O}} + e^- \tag{2.15}$$

$$V_{\dot{O}} \overset{K_b}{\leftrightharpoons} V_{\ddot{O}} + e^- \tag{2.16}$$

where e^- marks the "free" electron and K_a and K_b are equilibrium constants.

The concentration of oxygen vacancies shows a dependence on oxygen pressure between ${p_{O_2}}^{-1/2}$ and ${p_O}^{-1/6}{}_2$. [3]

In case of oxygen excess (formation of oxygen interstitials) the equation is as follows:

$$\frac{1}{2}O_2^{(g)} \overset{K_2}{\leftrightharpoons} O_i^x \tag{2.17}$$

$$O_i^x \overset{K_c}{\leftrightharpoons} O_i' + e^+ \tag{2.18}$$

$$O_i' \overset{K_c}{\leftrightharpoons} O_i'' + e^+ \tag{2.19}$$

The concentration of interstitial oxygen has an oxygen pressure dependence of ${p_O}^{1/2}{}_2$ to ${p_O}^{1/6}{}_2$, whereas that of electron holes lies in between ${p_O}^{1/4}{}_2$ and ${p_O}^{1/6}{}_2$. [3]

Oxides with Cation Defects

The reactions for non-stoichiometric oxides with metal deficits (= metal vacancies) can be written thus:

$$\frac{1}{2}O_2 \overset{K_3}{\leftrightharpoons} V_M^x + MO \tag{2.20}$$

$$V_M^x \overset{K_g}{\leftrightharpoons} V_M' + e^+ \tag{2.21}$$

$$V_M' \overset{K_h}{\leftrightharpoons} V_M'' + e^+ \tag{2.22}$$

where K_3, K_g and K_h are equilibrium constants.

The concentration of electron holes shows a dependence on oxygen pressure between ${p_O}^{1/4}{}_2$ and ${p_O}^{1/6}{}_2$. The concentration of a metal deficit ranges from ${p_{O_2}}^{1/2}$ for neutral vacancies to ${p_O}^{1/6}{}_2$ for doubly charged vacancies. [3]

Effects of foreign ions on defect equilibria

The presence of foreign ions in an oxide can greatly affect the defect equilibria. This effect can be explained as a valence effect.

In the case of n-type oxides ($M_{b+n}O$ or MO_{a-x}), the addition of cations with a higher valence than that of the parent oxide will decrease the concentration of oxygen vacancies for MO_{a-x} or the concentration of metal ions for $M_{b+n}O$. The addition of cations with a lower valence on the other hand increases the defect concentrations respectively.

In the case of p-type oxides ($M_{b-m}O$ or MO_{a+y}), the addition of cations with a higher valence increase the concentration of metal ion vacancies for $M_{b-m}O$ or the concentration of interstitial oxygen for MO_{a+y}. The addition of cations with a lower valence on the other hand decreases the defect concentrations respectively.

Corresponding rules can be set up for the addition of foreign anions. However, these rules do not apply if the foreign ions enter the parent oxide as a misplaced ion or on an interstitial position.

2.1.4 Diffusion

Diffusion through solids can only take place due to defects in said solid. The process of bulk diffusion (also called lattice diffusion) proceeds through point or lattice defects. Line and surface defects such as grain boundaries or dislocations provide paths for grain boundary , short circuit and surface diffusion.

The latter have a lower activation energy and therefore provide faster diffusion paths, which makes them increasingly important at lower temperatures.

Apart from the necessary diffusion paths, a difference in chemical potential is necessary as a driving force [3, 12]. Fick formulated his first law to define the diffusion coefficient

$$J = -D\left(\frac{\partial c}{\partial x}\right)_t \tag{2.23}$$

where D is the diffusion coefficient, c is the concentration of the diffusion species at the plane, J the flux and $\partial c/\partial x$ is the concentration gradient normal to the plane. D therefore is a flow rate, usually given in square centimeters per second.

Fick's first law however only applies for a fixed concentration gradient. In order to take a change of concentration over time into account we have to use Fick's second law

$$\frac{\partial c}{\partial t} = \frac{\partial}{\partial x}\left(D\frac{\partial c}{\partial x}\right) \tag{2.24}$$

If the diffusion coefficient is independent of the concentration, equation 2.24 becomes

$$\frac{\partial c}{\partial t} = D\frac{\partial^2 c}{\partial x^2} \tag{2.25}$$

where c is the concentration, t the time, D the diffusion coefficient and x the position.

Diffusion in oxides

At high temperatures bulk diffusion is the main mechanism. This means, that oxides with a low diffusion coefficient and therefore slow lattice diffusion are preferable in high temperature materials. Figure 2.5 shows a comparison between self-diffusion coefficients of cations at various temperatures, where alumina (Al_2O_3) has the lowest.

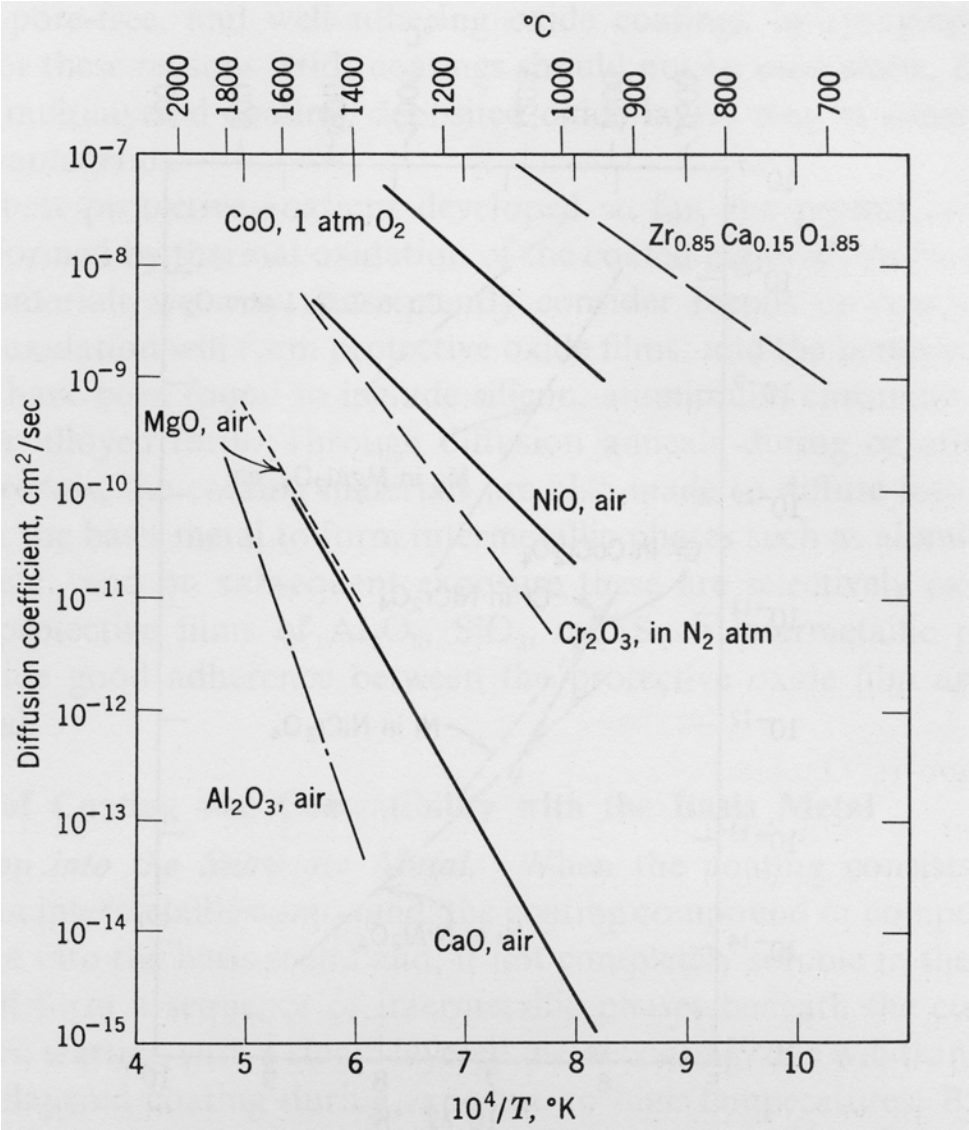

Figure 2.5: A comparison between diffusion coefficients for various oxides over temperature. (Kofstad [3])

2.1.5 Kinetics

The kinetics of oxidation have been thoroughly examined in various studies. In order to relate reaction rates to temperature and oxygen pressure as well as composition, structure and growth of the formed oxides. Most of the studies in this area correlate changes in oxide thickness or weight gain over time.

Oxidation reaction rates can follow different laws: parabolic, linear, logarithmic, inverse logarithmic and combinations of these.

Logarithmic and Inverse-logarithmic Rate Equations

Logarithmic growth rates are typical for low temperature oxidation (<300°C) of a large number of metals. The reaction proceeds very rapidly at first and then slows down to very low or even negligibly small values.

The direct logarithmic equation is

$$x = k_{log} \log (t + t_0) + A \tag{2.26}$$

The inverse logarithmic equation is

$$\frac{1}{x} = B - k_{il} \log t \tag{2.27}$$

where x either represents the amount of oxygen consumed per unit surface, the amount of metal transformed to oxide or the thickness of the oxide film. t stands for time, k_{log} and k_{il} are rate constants and A and B are constants.

Parabolic Rate Equation

At high temperature a large variety of metals show a parabolic growth rate. It's differential form is

$$\frac{dx}{dt} = \frac{k'_p}{x} \tag{2.28}$$

after integration it can be written thus

$$x^2 = 2k'_p t + c_p \tag{2.29}$$

where k'_p and k_p are the parabolic rate constants and c_p is the integration constant.

A comparison of the parabolic rate constants versus temperature for various oxide formers was published by Hindam and Whittle [4], which shows that Al_2O_3, Cr_2O_3 and SiO_2 have the lowest growth rates.

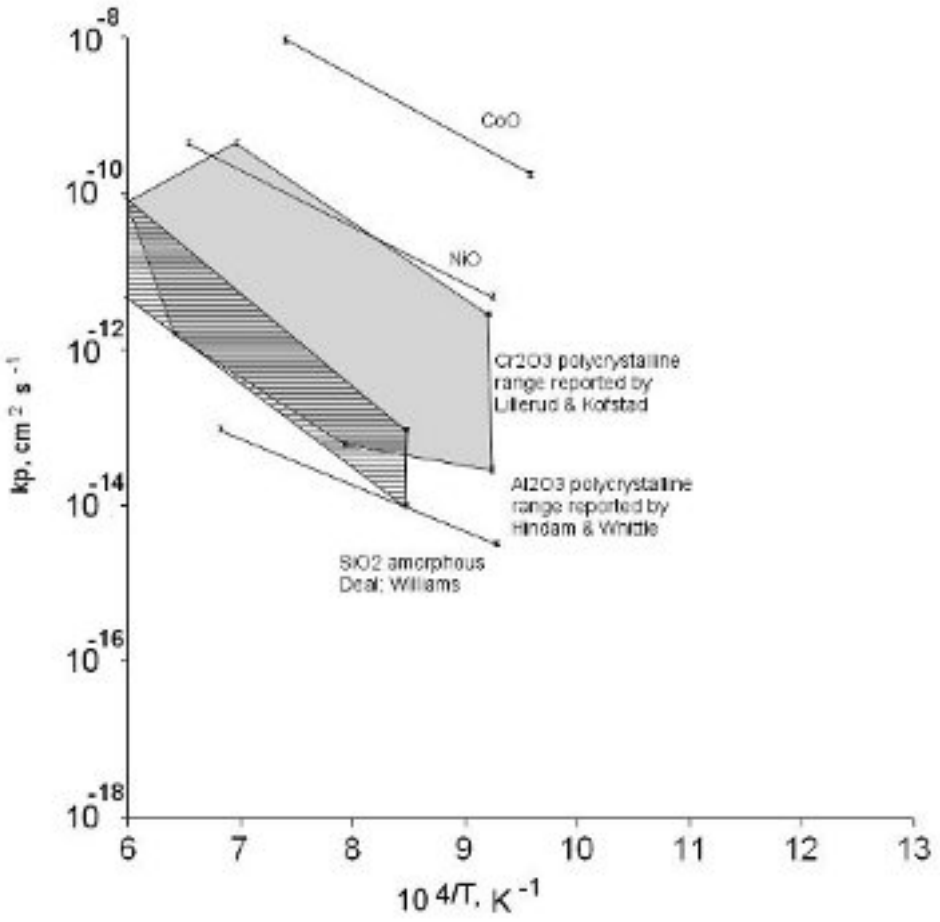

Figure 2.6: A comparison of the parabolic rate constant, k_p, for the growth of various oxide layers (redrawn after Hindam and Whittle [4])

The diffusion mechanisms at high temperature, which are determined by this reaction rate are explained in more detail in the section on Wagner's theory of oxidation.

Linear Rate Equation

The rate of linear oxidation is constant with time as opposed to parabolic and logarithmic, which both decrease over time. The equation is as follows

$$\frac{dx}{dt} = k_l \tag{2.30}$$

which after integration can be written

$$x = k_l t + c_i \tag{2.31}$$

where k_l is the linear rate constant and c_i the integration constant.

Wagner's theory of oxidation

Wagner's theory of oxidation [13] applies to systems with a compact oxide scale, where either the diffusion of reacting ions, or a transport of electrons across the growing scale are the rate-determining processes. The scale is assumed to differ only slightly from stoichiometry and to be relatively thick. It is further assumed that there is a thermodynamic equilibrium within the scale, as well as between all phases at the oxide-gas interface as well as at the metal-oxide interface. The driving force of the reaction therefore is the free energy change caused by the oxide formation. This leads to concentration gradients of the reactants within the oxide. (See figure 2.7)

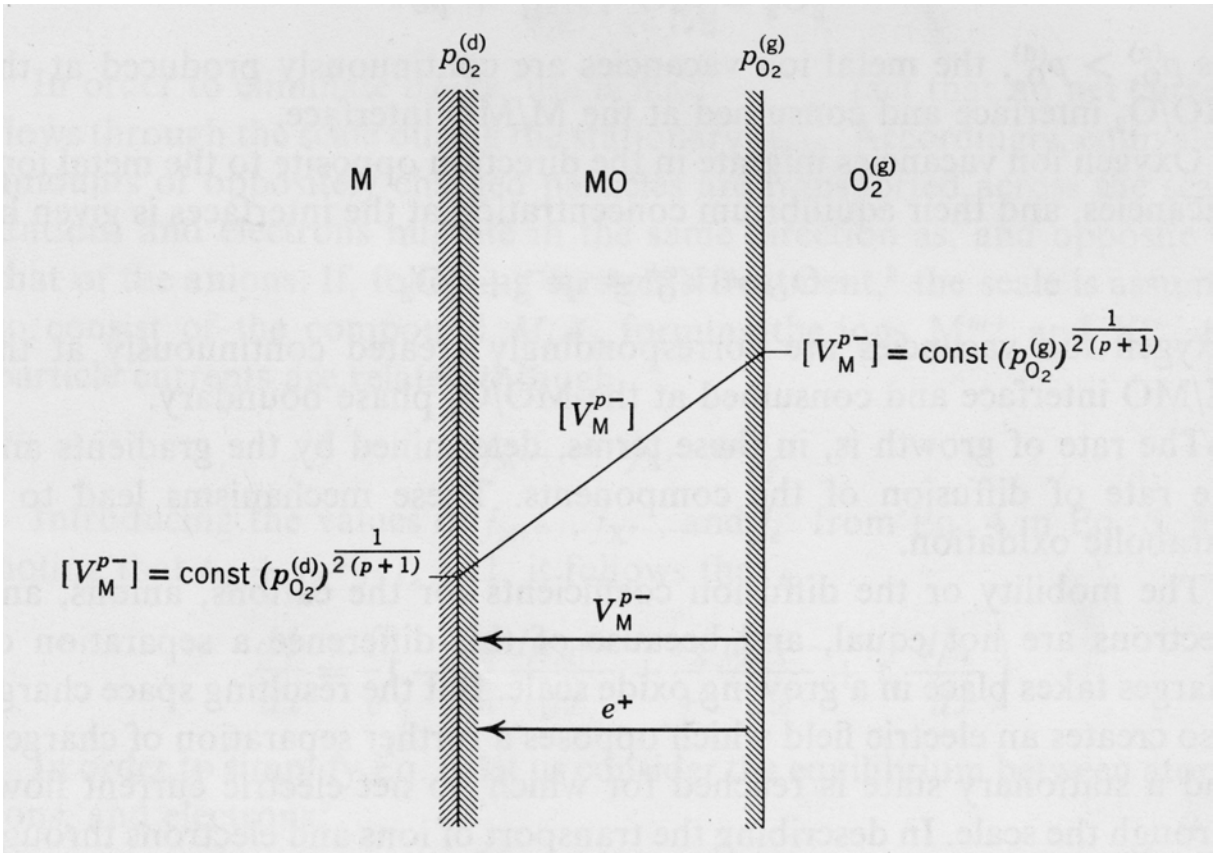

Figure 2.7: Schematic diagram showing the concentration gradient of metal ion vacancies and the transport processes in an oxide scale with mostly metal ion vacancies (Kofstad [3]).

At the metal-oxide interface the partial pressure of oxygen is equal to the dissociation pressure of the oxide in contact with the metal (in fig. 2.7 represented as $p_{O}^{(d)}{}_2$), and at the oxide-oxygen interface the partial pressure of oxygen equals that of the oxygen pressure in the gas (in fig. 2.7 represented as $p_{O}^{(g)}{}_2$).

This produces a gradient within the scale, which means that, e.g. in an oxide scale with metal ion vacancies, the metal ions will diffuse outwards through the scale to the oxide-gas interface, while the vacancies move in the opposite direction.

Because of the fact that $p_{O}^{(g)}{}_2$ is larger than $p_{O}^{(d)}{}_2$, metal ion vacancies are continuously produced at the oxide-gas interface, transported through the scale and consumed at the metal-oxide interface. The reverse process is happening to the oxygen ion vacancies.

Due to this transport of charged ions an electrical field will develop within the scale,

leading to a transport of electrons through the scale to maintain neutrality.

Wagner therefore used both electrical and chemical potential gradients as driving force for the diffusion of ions through a thick oxide scale [13]. This flux of a particle (i) is given as

$$J_i = -\frac{C_i D_i}{kT}\left(\frac{d\mu_i}{dx} + z_i q \frac{d\phi}{dx}\right) \tag{2.32}$$

where C_i is the concentration of the particle, D_i is its diffusion coefficient, $\frac{d\mu_i}{dx}$ the chemical potential gradient, z_i is the valence of the particle, q_i its electronic charge and $\frac{d\phi}{dx}$ the electrical field.

Evans and co-workers demonstrated the influence of stress on the kinetics of oxidation for an oxide, such as ZrO_2, in which oxygen vacancies dominate [14, 15]. The flux of vacancies through a stressed oxide is given thus

$$J_v \propto \frac{D_v}{\xi}\left[C_1 exp\left(\frac{\sigma_H \Delta\Omega}{kT}\right) - C_n\right] \tag{2.33}$$

where D_v is the diffusion coefficient, ξ the oxide thickness, C_n is the concentration of vacancies at the oxide surface, C_1 is the concentration of vacancies at the oxide/metal interface and the term σ_H describes the change of the free energy of formation of defects, where σ_H is the hydrostatic component of the local stress and $\Delta\Omega$ is the local change in volume.

The above equation can be simplified, due to the fact that the vacancy concentration at the oxide/metal interface is much greater than at the oxide/gas interface [14, 15]:

$$\frac{d\xi}{dt} = \frac{D_\circ{}^{diss}}{\xi} exp\left(\frac{\sigma_H \Delta\Omega}{kT}\right) \tag{2.34}$$

where $D_\circ{}^{diss}$ is the diffusion coefficient of oxygen at the dissociation pressure.

2.1.6 The need for coatings

Over the years, materials used in engines were continually improved to withstand higher temperatures (see fig. 2.8). A first big step was the change from wrought to cast, directionally-solidified materials [16]. The most recent development are single-crystal alloys. While these superalloys are specifically designed for their mechanical properties, e.g. creep and fatigue resistance, their oxidation resistance is relatively poor. Even though some superalloys initially form a protective oxide layer, once this is damaged and removed from the surface, the residual near-surface concentration of the oxidising element is too low to reform the layer and rapid, catastrophic oxidation occurs.

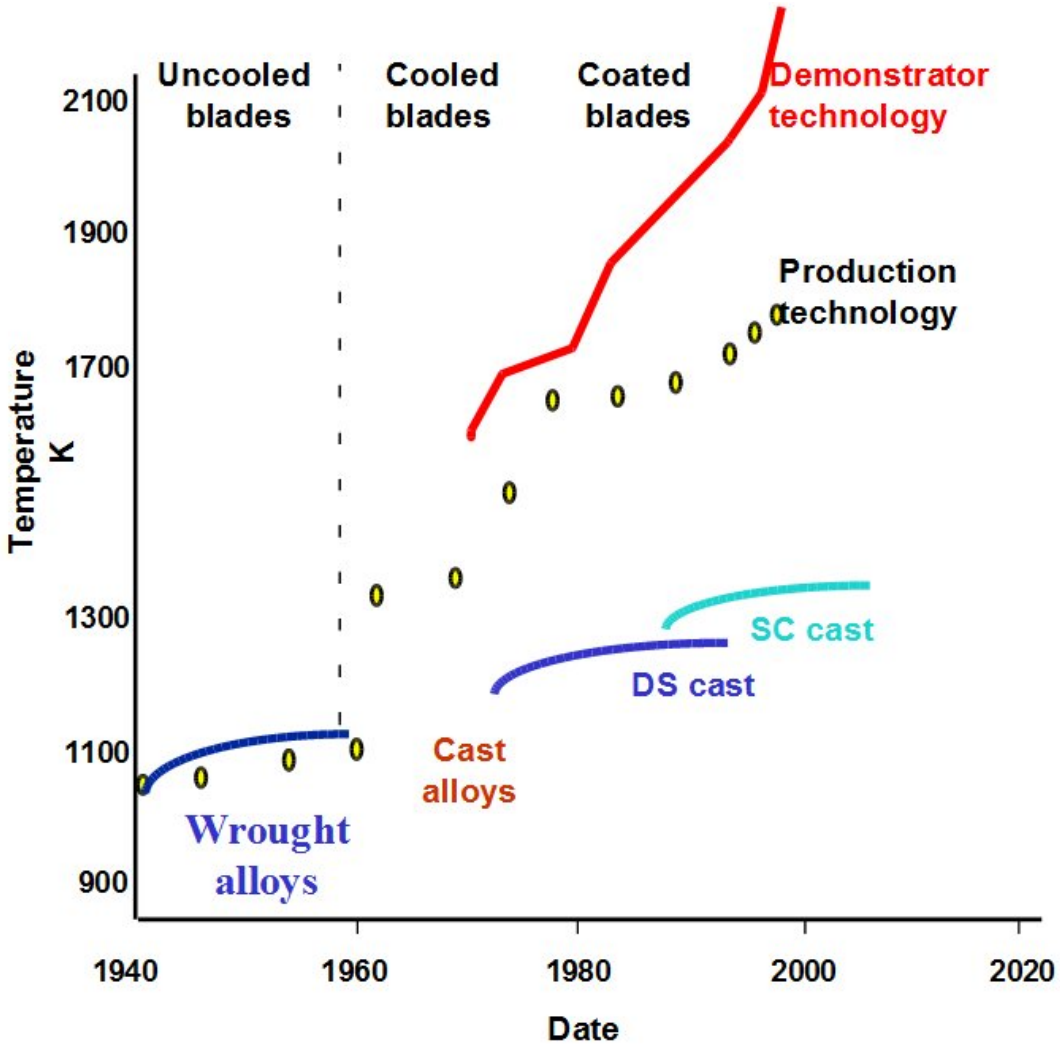

Figure 2.8: Development of materials in engines, showing the increase in temperature over the years, courtesy of Rolls Royce.

2.1.7 Protective oxide scales

In order to have a good oxidation protection, the formation of a slow growing, stable oxide layer that also shows a good adherence to the coating is necessary. A lot of research was done in this area and showed that the best protection is offered by chromia, silica and alumina [4] (see also figure 2.6). Of these three, alumina is the best for high temperature oxidation protection, as chromia can be converted to CrO_3 at temperatures above $950°C$ and silica, although being protective to temperatures around $1800°C$, is not chemically stable in moist environments.

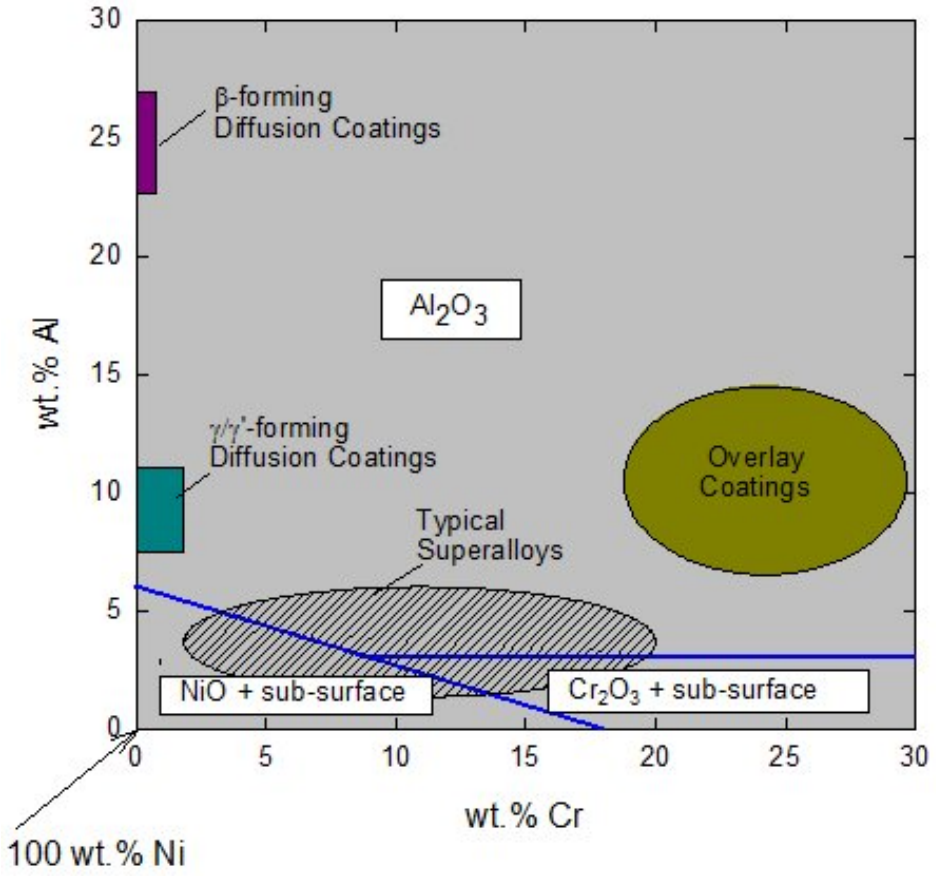

Figure 2.9: A schematic map, showing different alumina forming alloys and coatings at temperatures between 1000° and 1200°C in the Ni-Cr-Al system [5]

Overlay coatings

Overlay coatings contain enhanced amounts of beneficial elements such as aluminium and chromium and are deposited onto the surface of a superalloy by various methods,

such as air plasma spraying (APS), high-velocity oxy-fuel spraying (HVOF), physical vapor deposition (PVD) and electron beam physical vapor deposition (EB-PVD). These methods produce a distinct coating layer, with little interdiffusion with the underlying substrate [17]. The method of deposition also influences the morphology of the coating. Plasma sprayed coatings exhibit a layered structure. Particle surface oxidation can occur during spraying and oxides can be present within the coating which can reduce it's lifetime. [18] Coatings deposited by EB-PVD however, form vertical columns, with practically no oxide forming. However the boundaries between columns can act as weaknesses under mechanical stresses.

One very common example for this type of coating are MCrAlY coatings. Where M is Ni and/or Co, the coatings should have a β/γ structure, with β being either NiAl or CoAl and γ being a fcc solid solution, either Ni- or Co-rich. The actual microstructure however, depends not only on the composition, but also on deposition temperature and cooling rate. There is a 4-phase reaction for Ni-rich phases, that occurs around $980°C$ [19]

$$\beta + \gamma \rightarrow \gamma' + \alpha \tag{2.35}$$

α is the α-Cr solid solution, γ' is Ni_3Al and β and γ are the phases described above.

There are also variations of MCrAlY coatings, where other elements are added to improve either the alumina formation, the mechanical properties or adherence. They include silicon, hafnium, titanium, but also tantalum, molybdenum, niobium, rhenium and zirconium.

Other examples for overlay coatings are Ti-Al alloys [20, 21], FeCrAlY and SiCrAlY coatings [22], SMART MCrAlY coatings [23, 24] and oxide overlay coatings [25].

Diffusion coatings, focusing on Pt-aluminide bond coats

Diffusion coatings are usually produced by pack-cementation processes or by vapour transfer of the active element onto the component at elevated temperatures. Due to the diffusion of the active element into the substrate, there is less variety of composition possible

than with overlay coatings [17, 26].

A widely used form of diffusion coating are aluminide coatings. They are applied by either high- or low-Al activity pack cementation. High activity aluminising is done at temperatures between 800 and 1000°C and produces a layer of Ni_2Al_3 by inward diffusion of aluminium. This is then subjected to further heat treatment to transform the Ni_2Al_3 to NiAl. Low activity aluminising directly produces a continuous layer of NiAl by outward diffusion of nickel. These types of coatings always exhibit an interdiffusion zone at the substrate-coating interface.

Platinum can be added to this type of coating by depositing a thin layer onto the substrate before aluminising. It forms a (Ni,Pt)Al layer. Standard coatings incorporate up to 8 at.% Pt. The benefits of platinum will be discussed later in chapter 2.2.10.

Combined thermal barrier coatings (TBC)

Apart from oxidation and corrosion resistance, which is provided by the coatings mentioned above, another important feature in modern turbines is the need to protect the materials from high temperatures. The solution to this, is to apply a second ceramic coating (top coat) over the overlay or diffusion coating (bond coat) and the thermally grown oxide (TGO), together forming a so called thermal barrier coating (see figure 2.10).

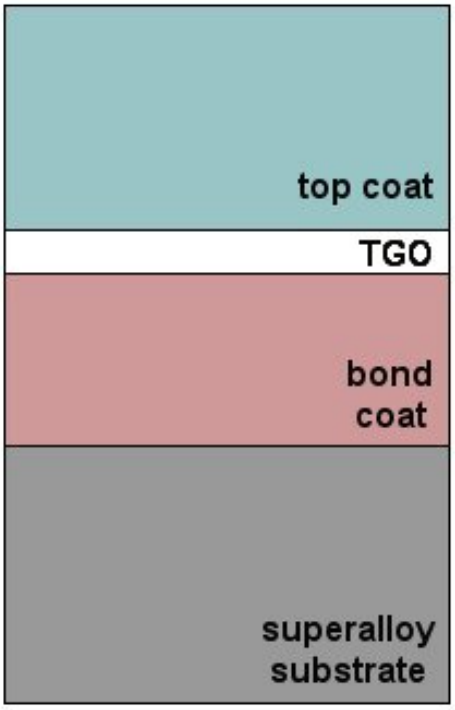

Figure 2.10: Schematic cross-section through a thermal barrier coating. Showing all the layers as discussed above.

The top coat usually consists of yttria-stabilised zirconia (YSZ), with an yttria content of about 7-8 wt.%. This layer has a thermal conductivity that is about one magnitude lower than that of alumina. In cooled turbine blades, temperature drops of around $150°C$ can be achieved over a 250-300μm thick top coat.

The production method of the top coat depends on the application and is usually air plasma spraying for larger, land based turbine blades. Smaller engine blades are coated by electron-beam vapour deposition.

The YSZ top coat does not, however, provide oxidation protection. This role, together with attaching the top coat to the substrate, is taken on by the bond coat. The oxide growing between top and bond coat is referred to as the thermally grown oxide (TGO).

2.1.8 Chemical failure due to aluminium depletion

As mentioned earlier, oxidation reduces the aluminium reservoir in the alloy. With increasing oxidation times, this will lead to a point where the growth of alumina can no longer be maintained. Within the alloy this leads, for example, to a transformation from

the aluminium rich $\beta - NiAl$ over $\gamma' - Ni_3Al$ to finally $\gamma - Ni$ phases near the metal-oxide interface. Aluminium depletion of the bond coat not only occurs by oxide formation, but also by interdiffusion with the underlying substrate. The effects of interdiffusion, however, are a lot more complex to model, though attempts have been made [27, 28, 29, 30].

2.1.9 Al-Ni-Pt phase diagram

To better interpret the role of platinum in the Al-Ni-Pt system, Gleeson and co-workers published an experimental ternary diagram [6] (see fig. 2.11). They used diffusion couples to determine which phases would develop at 1100°C and 1150°C. They showed that $\xi - PtAl_2$ and $\beta - NiAl$ have relatively large phase fields, as well as a compound phase, $\alpha - NiPt(Al)$, which shows an ordered face centered tetragonal crystal structure. The solubility limit of platinum in $\beta - NiAl$ and $\gamma' - Ni_3Al$ is 30-35 at. % at 1100°C. At 1150°C this solubility limit lies between 32-40 at.% of platinum. [31]

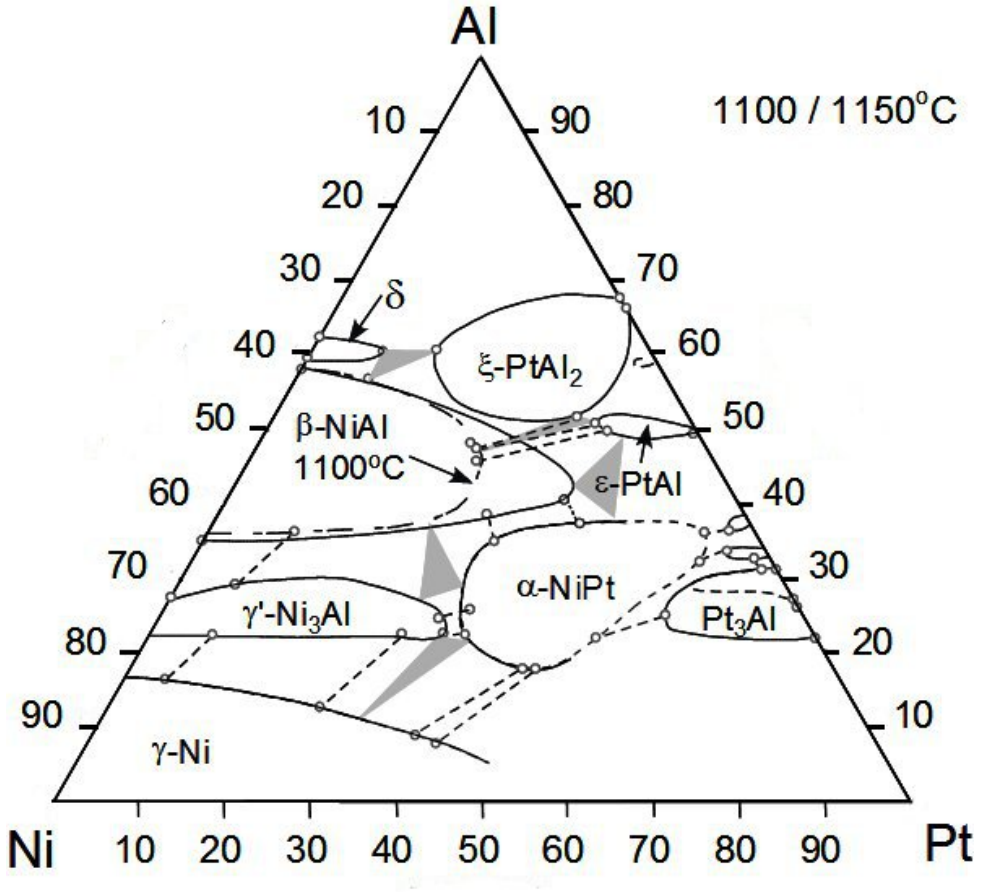

Figure 2.11: Experimental ternary Al-Ni-Pt diagram by Gleeson and co-workers [6].

2.1.10 The role of platinum

The role of platinum has been examined in many studies, with authors finding it has various beneficial effects on alloys and coatings.

The first commercial coating that contained platinum was LDC-2 [12]. It was manufactured by depositing a thin layer of platinum (between 2 and 10 μm) on the substrate, either by electroplating or PVD. Then the component was heat treated, either in vacuum or inert atmosphere at 850 to 1050°C to improve the adherence of the platinum on the substrate. In a next step aluminisation took place, either by pack, above-the-pack or CVD processes [12]. The finished coating was then subject to further heat treatments to make sure the desired microstructure and phase distribution was achieved.

Studies by Lehnert and Meinhardt [32] and Deb et al. [33] found that platinum improved oxidation capability by a factor 4 and the resistance against hot corrosion of type I by a factor 2 [12].

Initially platinum was used in aluminide coatings to create a diffusion barrier against aluminium, diffusing from the coating into the substrate [12]. But analysis afterwards showed that platinum did not act as diffusion barrier after all, though it did improve the overall performance of the coating.

It was found to improve oxide scale adherence. Fountain et al. [34] put this improvement down to a reduction of growth stresses in the oxide scale.

Zhang and co-workers [35, 36] suggest that the platinum interacts with sulphur in a kind of gettering effect, thereby countering its negative effects on scale adherence. They also attribute the positive influence of platinum to less void formation [37]. Several possibilities are discussed, like the presence of Pt strengthens the boning at the metal oxide interface and thereby preventing or slowing the growth of voids up to a point. Although the actual mechanism remains unclear, the authors showed that Pt greatly reduces the driving force for void formation [37].

Tawancy et al [38, 39, 40] found that platinum increases the coating stability towards inward diffusion of aluminium or the outward diffusion of nickel. It eliminates chromium-rich precipitates in the outer layers of the coating. Unlike in solid solution,

where chromium has beneficial effects, it reduces oxidation resistance when it's congregated as precipitates. Platinum also prevents refractory elements like Mo, V and W from diffusing from the alloy into the outer layers of the coating and so improves the coatings stability against interdiffusion between itself and the substrate. They also state that it improves the thermal stability and the capability for selective aluminium oxidation, thereby producing a purer, slower growing alumina scale.

Tawancy and Al-Hadhrami put this effect down to the fact that platinum works as a 'cleanser' [41] of the oxide-bond coat interface. They put this cleaning effect down to the deceleration of the kinetics of interdiffusion between the bond coat and the underlying superalloy. They find that the purer alumina scale also increases the adherence of the ceramic top coat. They also state that the not every platinum rich phase provides this better adherence. Pt-rich γ' was found to promote a longer coating life than a mixture of $PtAl_2$ and β [41].

Platinum also acts as a stabiliser for the β phase and prevents the transition from β to γ' due to thermal cycling [12]. Bose also states that it suppresses interfacial void formation and ties up aluminium in Pt-Al compounds, which is lowering the aluminium activity. This leads to a reduction in the driving force of nickel diffusing from the substrate into the coating.

Platinum reducing the activity of aluminium in the coating was also observed by Gleeson et al. [6]. This is looked at in detail by Marino and Carter [42, 43], who did first-principles density functional theory calculations and predict that platinum enhances the diffusion of nickel and aluminium in bulk $\beta - NiAl$. The stabilising effect that platinum has on defects, lowers the activation energy of these diffusion mechanisms [42].

Felten and Pettit [44] say that platinum improves the alumina scale adherence by forming an irregular oxide-alloy interface. They also state that the presence of platinum improves the self-healing of the alumina scale after spalling, provided the spallation is not too massive [44].

2.1.11 Microstructure of bond coat phases

NiAl

NiAl is an intermetallic compound, with a B2 structure (space group $Pm\overline{3}m$), an isomorph of CsCl. It is widely used in high-temperature components due to its high melting temperature, good oxidation resistance, high thermal conductivity and low density [45]. On cooling martensitic transformation can occur, see below.

Martensite

The martensitic phase transformation is a solid to solid transformation. While cooling, the lattice changes suddenly at a certain temperature. This process occurs without diffusion and the relative position of the atoms stays the same, although the unit cell undergoes a significant distortion. On reheating, at a certain temperature, the martensitic phase abruptly changes back to its original lattice. [7]

A typical feature of martensite, that is easily observable is its microstructure. Figure 2.12 shows the formation of said microstructure, where Fig. 2.12(a), the original high temperature phase, has a square lattice, the martensitic phase has two possible rectangular lattice variants Fig. 2.12(b) and Fig. 2.12(c) it can transform into. There is no reason for the original square lattice to transform into a single variant of martensite. Therefore different parts of the crystal transform into different variants, and the crystal takes on an entirely new shape. However, this new shape must be coherent with unbroken rows of atoms across the interfaces between variants. Such a coherent mixture of variants can be seen in Fig. 2.12(d). [7]

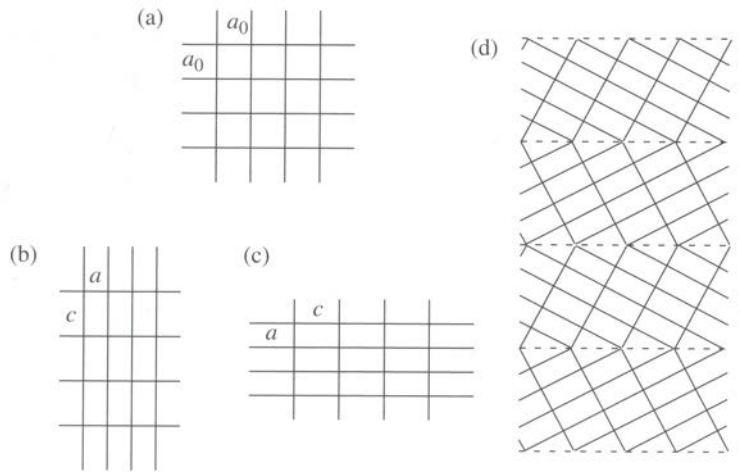

Figure 2.12: Fig. 1: A schematic illustration of martensitic transformation. (a) original grain (b,c) variants of martensite (d) arrangement of the variants in a martensite grain [7]

This microstructure has a length-scale range from a few nanometers to tenths of millimetres. The actual size depends on the material, specimen size, grain size and grain history [7].

In $NiAl$, martensitic transformation occurs at rapid cooling. According to Rosen and Goebel [46] the requirements for the formation of martensite are nickel contents greater than 63 at% and temperatures above 1000°C. A compilation of literature data gives an overview of the dependence of alloy composition and transformation temperature M_S (see figure 2.13) and shows large discrepancies in the measured M_S in $NiAl$ alloys [8].

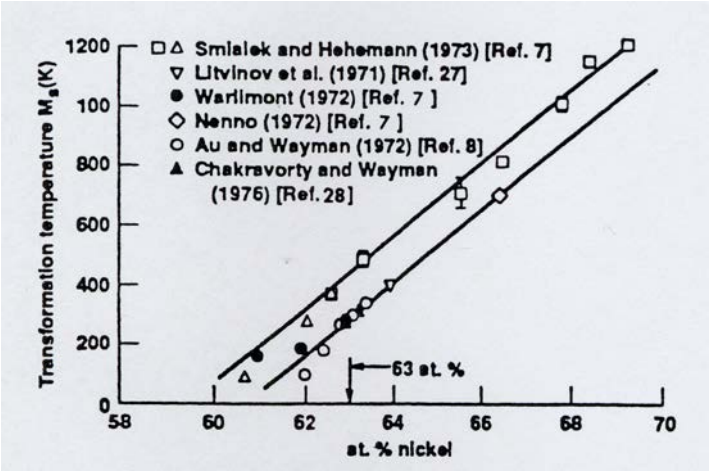

Figure 2.13: Literature data on the dependence of M_S on alloy composition [8]. There is an error in the original paper, the value 100 on the y-axis should be 1000.

Another factor for martensite formation is a cooling rate fast enough to suppress the transformation from β to γ'. Quenching is not always necessary, as martensite can also be fond in air-cooled specimens [47]. The critical cooling rate was established by Chen et al [48] to be less than 25°C per minute. They also found that the molar volume of the β-phase is roughly 2% larger than that of martensite. Other studies give values between 2.32 and 1.94% for the volume decrease of martensite.[47] This shrinkage is also regarded as one reason for oxide spallation, as it produces linear formation strains [49, 48]. Newer studies [50] with a focus on the influence of platinum show that high Pt contents increase the temperature range where martensite transformation occurs and at the same time Pt decreases the thermal expansion. These effects are likely related to the Ni-site preference of platinum, which decreases the shear moduli, raises the M_S temperature and increases the bulk modulus, restricting thermal expansion [50].

X-ray diffraction of the martensitic phase shows it to be an "ordered" AuCu-type, which is a face centered tetragonal structure (fct), Strukturbericht $L1_0$, space group P/4 mmm [46].

Ni_3Al

Ni_3Al has an ordered $L1_2$ structure, which consists of two sub lattices. The a-Sublattice consists of the face centres and has three times the number of lattice sites than the b-sublattice, which consists of the cube corners.

$PtAl_2$

$PtAl_2$ has a CaF_2-type structure with the space group Fm3m and has more than 12 atoms in the unit cell [51]. Suess et al [52] did an extensive study into the phase stability of the $PtAl_2$ in the Pt-Al-Cr system, where they identifies invariant reactions and present a ternary diagram.

2.2 Alumina scale

2.2.1 Microstructure of alumina phases and phase transformation

There are several transitional oxides, that will with time transform into the stable $\alpha - alumina$ [53]. This transformation is usually considered to occur in the following sequence [54, 55]:

$$\gamma - Al_2O_3$$
$$\downarrow$$
$$\delta - Al_2O_3$$
$$\downarrow$$
$$\theta - Al_2O_3$$
$$\downarrow$$
$$\alpha - Al_2O_3$$

$\gamma - Al_2O_3$ is can be described as defect spinel structure (cubic, space group $Fd\overline{3}m$), where 32 oxygen anions form a $2 \times 2 \times 2$ array of face-centered cubic subcells [56, 57].

The $\delta - Al_2O_3$ is considered to be a superlattice of $\gamma - Al_2O_3$, it has been described as tetragonal as well as orthorhombic, the detailed atomistic structure, however, remains unknown [56].

$\theta - Al_2O_3$ is an isomorph of $\beta - Ga_2O_3$, monoclinic symmetry with the space group $C2/m$ [56, 57].

The stable $\alpha - Al_2O_3$ is trigonal with rhombohedral centering (space group $R\overline{3}c$). The anions form a hexagonal closed packing, the cations are in octahedrally coordinated interstitial sites [58].

These transient oxides form at the early stages of oxidation, before transforming to the stable and slow growing $\alpha - Al_2O_3$. There are different opinions on where the nucleation of $\alpha - Al_2O_3$ actually happens. Yang et al. [58] showed this to happen at the oxide/metal

interface. This was later confirmed by Svensson, Angenete and Stiller [59], who also stated that the nucleation sites were different for different coatings. Earlier studies by Brumm and Grabke [60] as well as Doychak and Ruehle [61], however, showed that the transformation takes place at the oxide/gas interface.

Tolpygo and Clarke [62] looked at the alumina phases and their spatial distribution in the oxide scales with photo-stimulated luminescence spectroscopy (PSLS). They showed that the scale initially consisted entirely of $\theta - Al_2O_3$. With longer oxidation times at 1000°C nuclei of $\alpha - Al_2O_3$ started to appear also at the oxide/metal interface. They also observed that whiskers of $\theta - Al_2O_3$ retained their morphology even after transforming to $\alpha - Al_2O_3$.

Chapter 3

Experimental Procedure

In this section specimen compositions will be provided and details given of the sample preparation, the various analysis techniques used and the experimental setup for the oxidation testing. Since two different specimen sets were used, this section contains three main parts, the first two dealing with each specimen set and the third describing the TEM sample preparation, which was the same for the specimens from both sets.

3.1 Low Pt specimens

The first set of samples consisted of a conventional thermal barrier coating on a substrate of CMSX 4 (composition given in table 3.1), provided by Chromalloy United Kingdom Limited.

	Ni	Co	W	Cr	Al	Ta	Re	Hf	Ti	Mo	Nb
CMSX4	Bal.	9.8	6.4	6.4	5.6	6.5	3.0	0.1	1.0	0.6	0.4

Table 3.1: Composition (wt.%) of CMSX4.

The bond coat was a standard platinum aluminised one, which had trenches with different depths cut into them (see figure 3.1). These were only significant for a previous study and any samples cut for this work were taken well away from the trenches. The top coat was yttrium stabilised-zirconia, deposited by EBPVD in five stages. The total coating thickness was 140 μm (see figure 3.2(a)). These specimens had been used in a different study, where long term oxidation experiments had been carried out: the tests

led to spallation of the thermally grown oxide (TGO) and top coat, leaving the substrate with an aluminium depleted bond coat, which was ideally suited for this study (see figure 3.2.(b)).

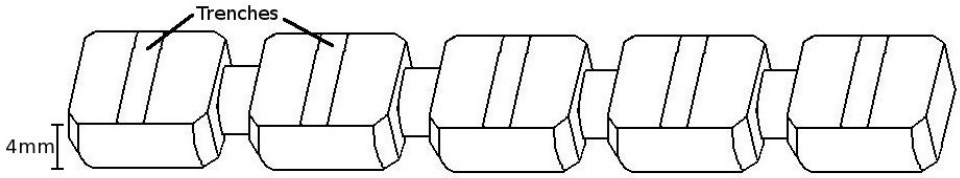

Figure 3.1: Schematic figure of the low Pt specimen.

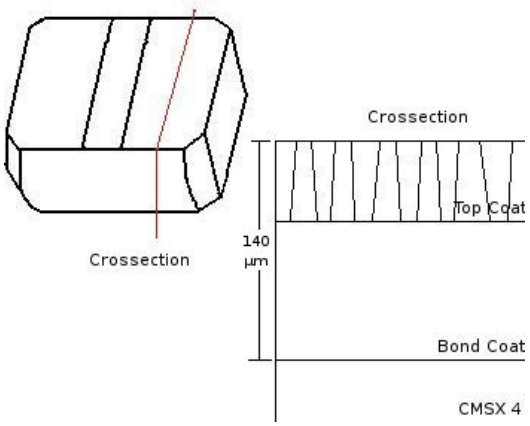

(a) Cross section, showing the specimen with the top coat still intact.

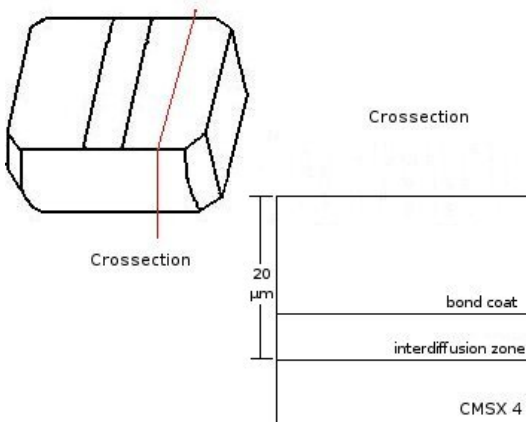

(b) Cross section, showing the specimen after extended oxidation testing, as it was used in this study.

Figure 3.2: Schematic of cross sections, showing the effect of an earlier long term oxidation experiment prior to this study.

Specimen geometry

The specimens were produced from a 10.3mm diameter and 127mm long rod of CMSX4. One side was machined flat to provide a flat surface (see figures 3.1 and 3.2). This was done for an earlier study. Recesses were made along the length of the rod, such that sectioning into small specimens could be easily achieved later. All surfaces were coated. The rounded bottom of the rod was subsequently ground to produce a flat surface, this was done for ease of handling. This also removed the bond coat on this particular side of the specimen. After this procedure the specimens were 4 mm thick. The bond coat thickness is about 20 μm.

Sample preparation

For initial analysis a whole piece (10.2 x 10.3 x 7.3 mm) was cut off and the surface polished with diamond lubricant; starting with 20 minutes with each 6 μm, 3 μm and finished with 1 μm.

All further low Pt specimens were then cut into cross sections as indicated in figure 3.2, well away from the trenches, leaving pieces of 4 by 10 by 1.5 mm (see figure 3.3).

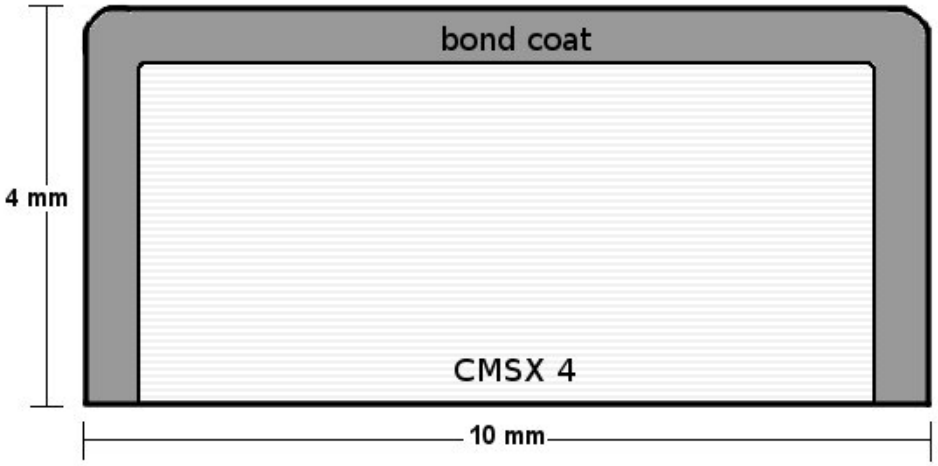

Figure 3.3: Schematic of the low Pt specimen.

The cutting was done using an acutom precision cutter with an aluminium oxide cut-off wheel. They were then glued onto specially made holders using Araldite, ground with decreasing grits from 400 to 1200 and subsequently polished with diamond lubricant for 20 minutes, starting at 6 μm, going down to 3 μm and then 1 μm with a final polishing for 20 minutes in activated colloidal silica.

Oxidation testing

The oxidation testing was done in a vertical furnace (see fig. 3.4) in laboratory air. The experiments were carried out at 1100°C for 3, 7 and 10 minutes at temperature. The furnace was preheated to 800°C to ensure rapid heating. Some preliminary testing was also done at 1100°C for 15 minutes.

Figure 3.4: Vertical furnaces used for oxidation testing.

The time from inserting the specimens into the furnace, to the furnace reaching 1100°C was measured each time and on average was two minutes (See fig. 3.5). From then on the time of the actual experiment was recorded. After that, the furnace was switched off, lowered and the specimen was left in the silica pan to cool for 2 minutes before being transferred to an alumina boat for cooling down to room temperature; the whole cooling process took about 5 minutes.

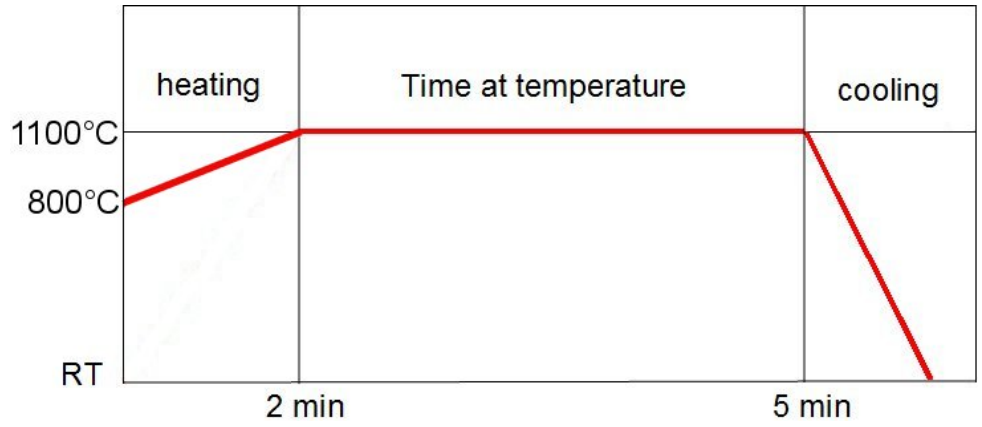

Figure 3.5: The graph shows the thermal history of the specimens, from inserting it into the preheated furnace at 800°C, until it reaches 1100°C. From that point the time at temperature is measured, with the subsequent cooling time after lowering the furnace.

All samples were ground and polished as described above prior to testing.

3.2 High Pt specimens

The second set of specimens (hereafter called Set B), was supplied by Turbine Surface Technologies Ltd (TSTL) and consists only of the CMSX 4 matrix with a platinum modified nickel-aluminium bond coat. This bond coat contained higher platinum levels (approximately 15 at.%) and a thicker bond coat (thickness 100 μm) than conventional Pt-aluminide diffusion coatings, to examine the effects of platinum on the Ni-Al-Pt system.

Specimen geometry

The specimen were supplied in the form of three 132 mm long rods. Each had a diameter of 8mm and, due to manufacturing reasons, a 15mm long uncoated end (see figure 3.6).

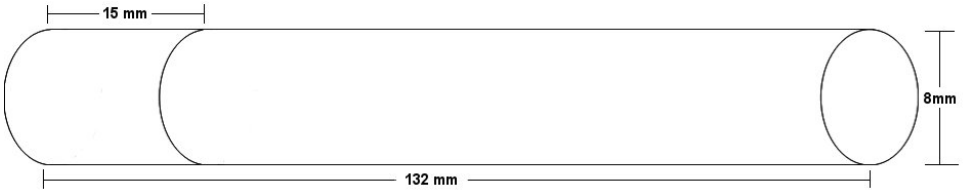

Figure 3.6: Schematic of the rods (not to scale).

3.2.1 Sample preparation

The rods were cut into 2mm thick pieces using an acutom precision cutter with an aluminium oxide cut-off wheel. These were then glued onto holders and ground with decreasing grits from 250mm to 1200mm and subsequently polished with diamond lubricant, starting at 6 μm, going down to 3 μm, then 1 μm and with a final polishing for 20 minutes in activated colloidal silica prior to testing. A schematic of the specimens dimensions can be seen in figure 3.7

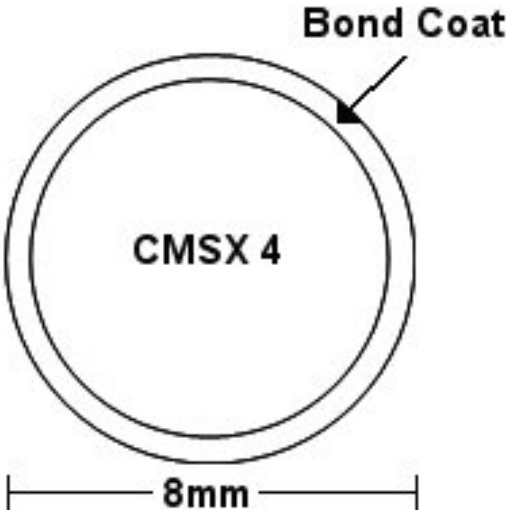

Figure 3.7: Schematic showing the dimensions of the high Pt specimens (not to scale).

Oxidation testing

Two different oxidation series were applied to the high Pt specimen. The first series used a vertical furnace (see fig. 3.4) following the same procedure as described for the low Pt specimens (1100°C for 3, 7 and 10 minutes).

A second series was carried out in order to determine oxidation kinetics. These tests were done in a horizontal furnace (fig. 3.8) at 1100°C for 100, 75, 50, 25, 20, 15, 10 and 1 hour in laboratory air. The specimens were placed in alumina boats and inserted into the preheated furnace (to 1100°C) to ensure rapid heating of the samples. After oxidation, the samples were left to cool in the furnace, since testing showed that this reduced spallation on cooling. A graph of the measured cooling rate can be seen in fig. 3.9.

Figure 3.8: Horizontal furnace used for oxidation testing.

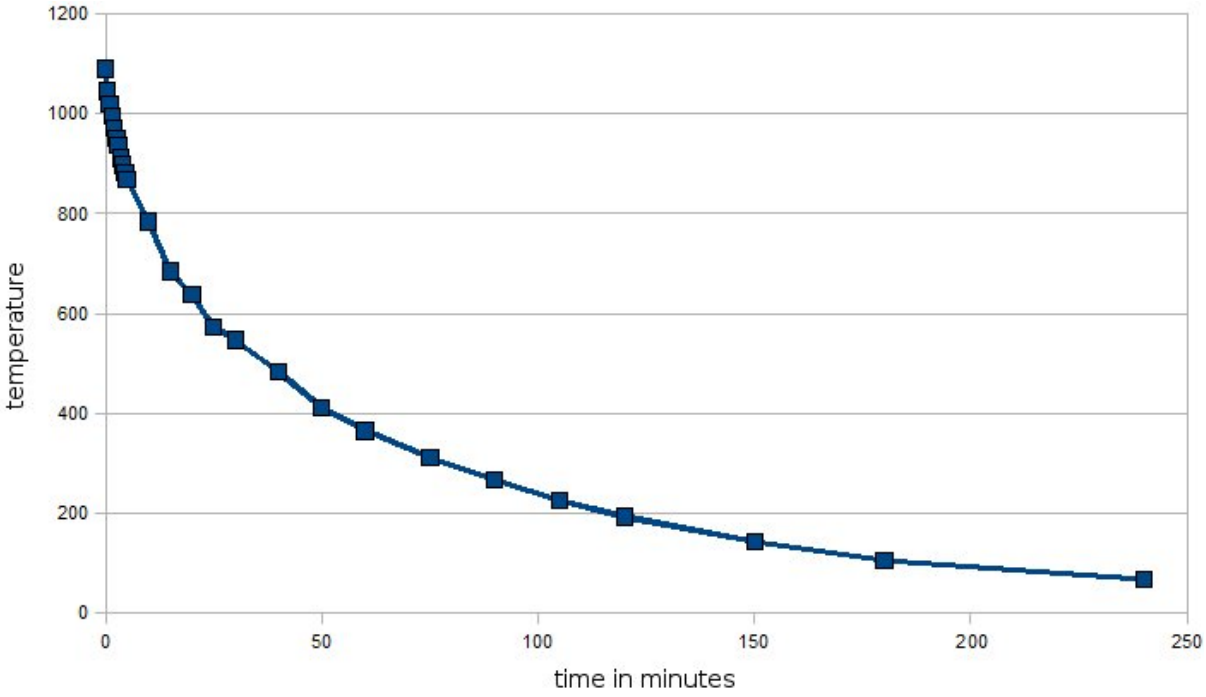

Figure 3.9: Cooling rate of the horizontal furnace.

The furnace temperature was measured using a calibration thermocouple. These measurements showed that the actual temperature within the furnace was 40 degrees lower than the temperature shown on the furnace controls. The temperatures were adjusted accordingly.

No mass gain measurements were carried out, but the specimens were sectioned to obtain oxide thicknesses.

3.2.2 TEM sample preparation

In order to choose an interesting area for TEM investigation, e.g. phase boundaries of two different phases in the bond coat with overlying oxide layer, the sample preparation was carried out using ion beam milling in a FIBSEM. This work was mostly done at Loughborough University under the supervision of Dr. West.

First, a protective layer of platinum was deposited onto the oxide surface using electron beam deposition. Due to the rough surface of the oxide, a second, thicker platinum layer was deposited using the ion beam (see figure 3.10a). Then the sample was tilted in order

to mill trenches on either side of the platinum strip, leaving the area of interest intact. (figure 3.10b)

The next step was to cut through the sample, leaving only a small piece attached (figure 3.10c). Then, after a needle was inserted and welded to the sample (figure 3.10d), it was finally cut loose and could be lifted from the specimen and welded onto a copper grid. (figure 3.10e)

This sample was then electron transparent (figure 3.10f).

3.2.3 Analysis techniques

Electron microscopy

Three different scanning electron microscopes were used, providing different resolutions depending on the requirements of the various areas on the specimens. For general purposes, low resolution images and EDS phase characterisation, a JEOL 6060 SEM with a tungsten filament was used. A Philips XL-30 microscope with a LAB6 filament was used for low resolution imaging of the newly grown alumina.

For high resolution images of the alumina crystals, a JEOL 7000F microscope with a field emission gun was used. This provides a very stable high density, narrow electron beam. It was also used for high resolution imaging of the cross sections of the oxidised samples.

In addition the JEOL 7000F is fitted with an EBSD camera, which provided grain orientation maps of the bond coat phases and aided in the identification of oxide phases.

Transmission electron microscopy was carried out on a FEI TecnaiF20 field emission TEM. The work included imaging, EDS point analysis, STEM line scans and elemental maps, both techniques using a new drift detector supplied by Oxford Instruments, and electron diffraction.

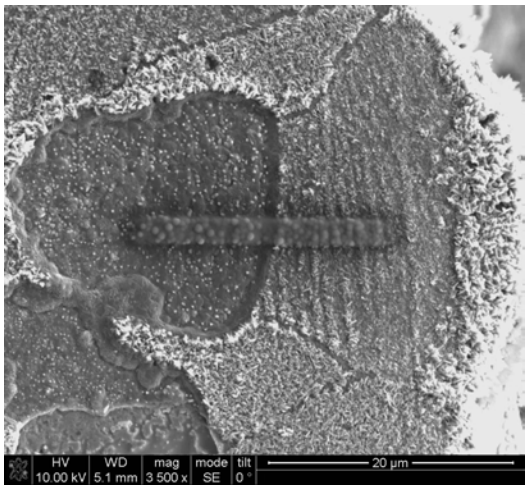

(a) SE image: plan view of the oxide layer after the deposition of a protective Pt strip.

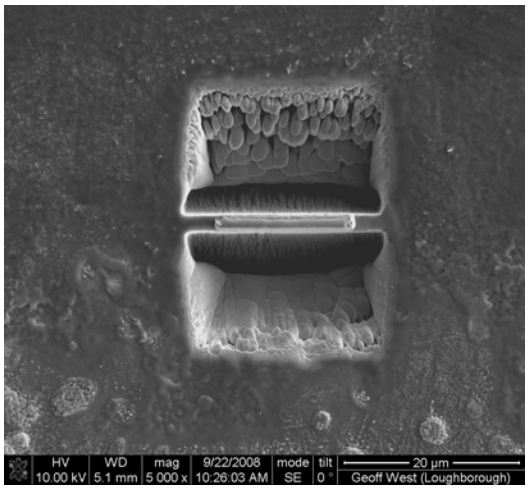

(b) Ion beam image after milling, showing the trenches above and below the area of interest.

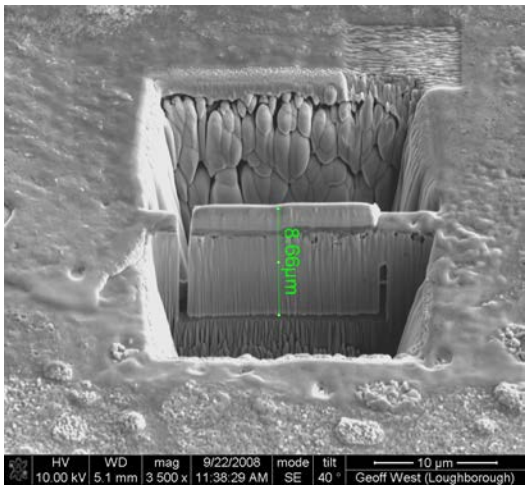

(c) SE image: Preparation for lift out, the TEM sample is only attached to the specimen by a bridge on the right hand side.

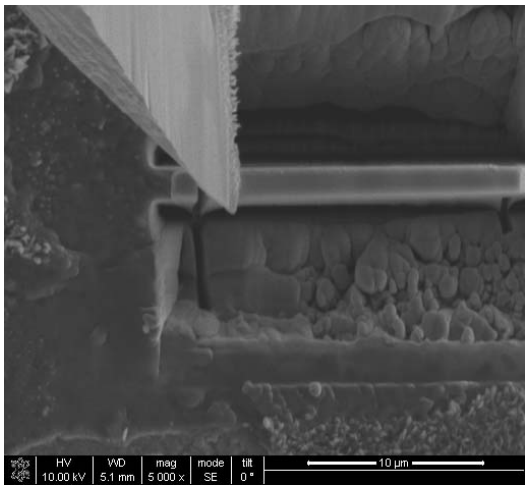

(d) SE image of the inserted needle for the lift out procedure.

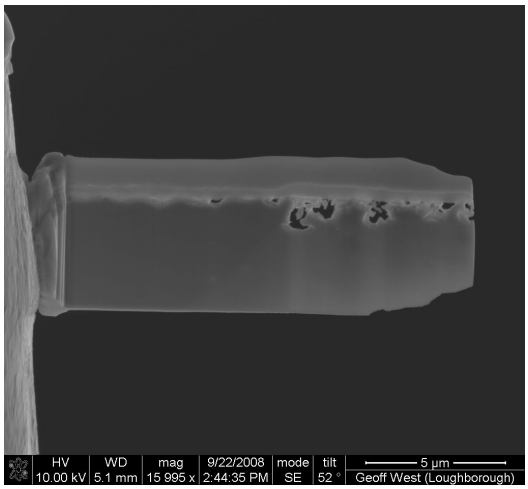

(e) SE image, showing the specimen welded to a copper grid.

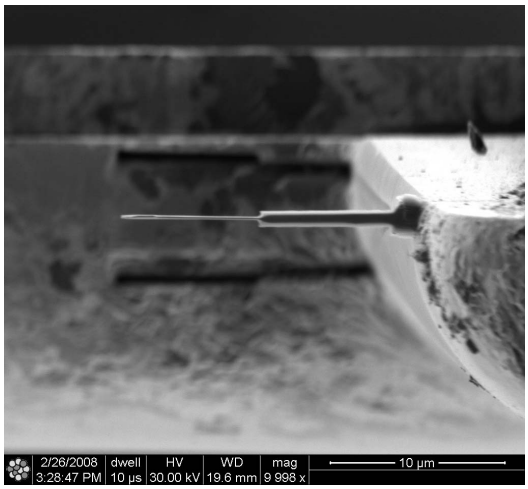

(f) Ion beam image, showing the TEM sample after the final thinning of the left hand side of the sample.

Figure 3.10: The different steps of TEM sample preparation by focused ion beam milling.

Chapter 4

Experimental Results

The results of various experiments and examinations undertaken in this study will be presented in this chapter.

4.1 SEM characterisation of the as-received specimen

4.1.1 low Pt specimens

The low-Pt specimens were, after polishing as described above, characterised by scanning electron microscopy (SEM) imaging and Energy-dispersive X-ray spectroscopy (EDX analysis). The whole coating is about 85μm thick, with a 45μm thick interdiffusion zone at the bond coat - substrate interface and a 40μm thick zone consisting of $NiAl$ and Ni_3Al grains. The grain size varies from 10 to 40μm for both phases (see fig. 4.1). The smaller, white phases seen in the interdiffusion zone in figure 4.1 are precipitates, containing Cr, Co, Ni, W and Re in various concentrations(see table 4.2). These form due to the interdiffusion between superalloy and bond coat, where the heavy elements are not soluble in $\beta - NiAl$ [63]. Others find they contain Ta, Co, Cr and Mo [64, 65, 66]. Molins et al [66] describe the development of precipitates, depending on the exposure time to high temperatures. In the as-recieved state the NiPtAl bond coat they were studying consisted only of $\beta - NiAl$. After oxidation for 1 hour at 1100° they find precipitates occuring at

grain boundaries. They could also show that sulphur is present around these precipitates. Oxidation for 10 hours leads to the formation of α-Cr precipitates. [66].

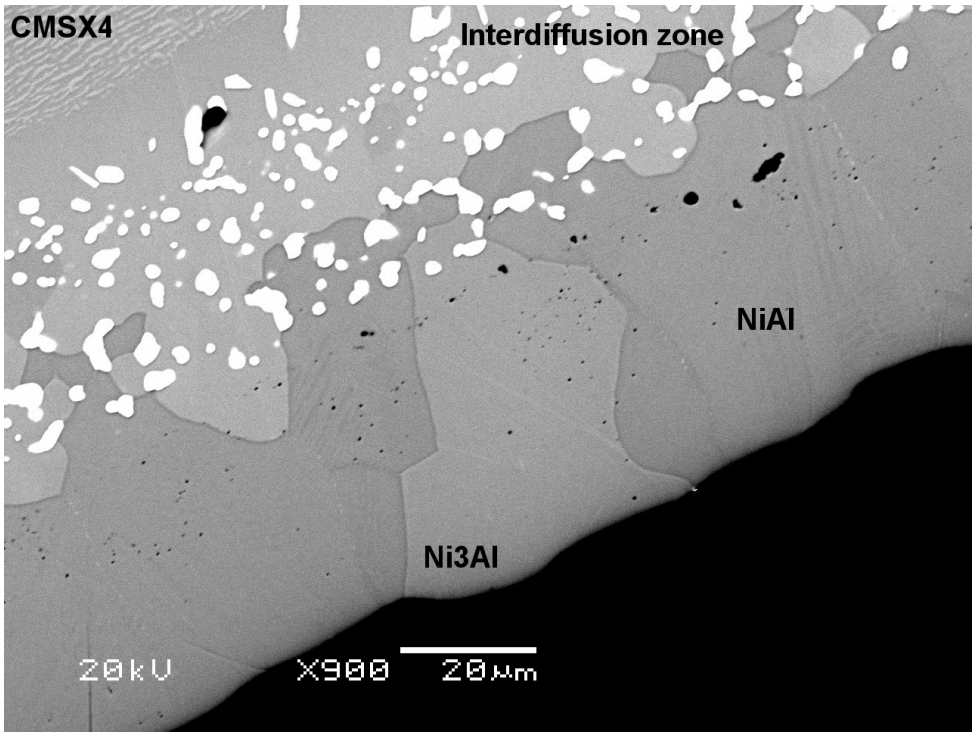

Figure 4.1: Cross section BSE micrograph, showing the typical morphology of the as received low Pt specimens.

Specimen chemistry

The chemistry of the bond coat was investigated using EDS analysis in both a JEOL 6060 and a JEOL 7000 SEM.

Image analysis, point analysis and line scans were carried out. The micrographs clearly show the presence of two different bond coat phases. They were identified as β - $NiAl$ and γ' - Ni_3Al. A typical analysis of both phases is shown in table 4.1.

γ' - Ni_3Al		β - $NiAl$	
Element	Atomic %	Element	Atomic %
Al	22.3	Al	33.0
Ti	1.4	Ti	0.7
Cr	3.9	Cr	5.6
Co	8.1	Co	6.5
Ni	60.5	Ni	49.3
Pt	3.6	Pt	5.0

Table 4.1: Typical analysis of the bond coat phases.

Cr	Co	Ni	W	Re
21.59	17.3	22.9	22.4	15.5
26.38	14.6	18.7	20.2	20.1

Table 4.2: Typical analysis of precipitates in atomic %.

Figure 4.2 shows the composition of the bond coat phases on the experimental Ni-Al-Pt ternary diagram produced by by Gleeson at Al [6]. All elements other than aluminium and platinum were added onto the nickel, to incorporate a system that has more elements than the ideal ternary. This reveals that the composition of the γ' - Ni_3Al phases lies near the lower limit of the Ni_3Al single phase field. The composition of the β - $NiAl$ is very low in aluminium, placing it in the 2 phase field just below the $NiAl$ stability field, indicating that it is unstable and likely to transform to Ni_3Al. This can be seen in figure 4.3, where even after very short term the transformation occurs.

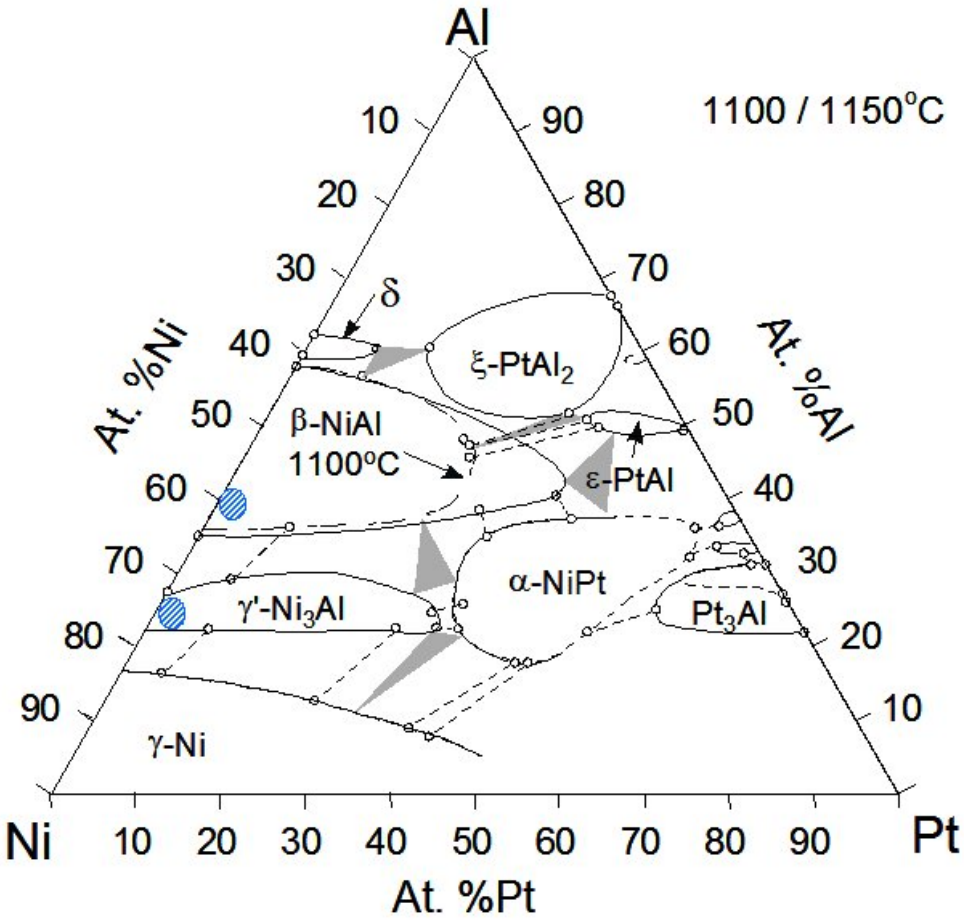

Figure 4.2: Experimental ternary Ni-Al-Pt diagram by Gleeson at al [6]. The blue circles show the composition of the bond coat phases.

In order to investigate the bond coat phases close to the metal/oxide interface, specimens were carefully polished after short term oxidation experiments to remove the oxide. They show the formation of Ni_3Al-nuclei within the $NiAl$ grains, that begin to form due to aluminium depletion during oxidation. This was done after 3 and 7 minutes at 1100°C. The structures seen in figure 4.3 appeared after 3 minutes of oxidation, there is ,however, no marked difference to the 7 minutes experiment.

The Ni_3Al-nuclei appear prominently at phase boundaries between $NiAl$ grains, but also as thin, elongated grains within $NiAl$; however they don't appear near phase boundaries with Ni_3Al grains.

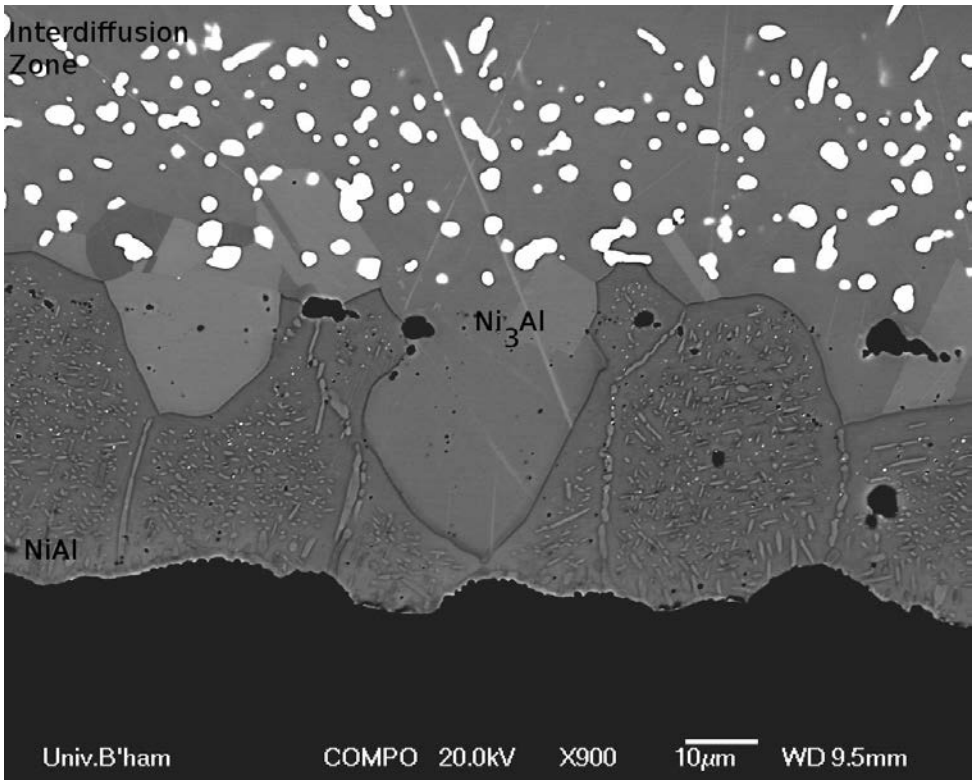

Figure 4.3: The low Pt coating after a short heat treatment. The further aluminium depletion shows in the formation of precipitates withing the $NiAl$.

4.1.2 High Pt specimens

The high Pt specimen had a very thick bond coat, with an average thickness of 145μm. The bond coat has 3 zones of different thicknesses, the outer zone with a Pt content of 15-20 at.% which is about 45μm thick; an inner zone with a lower Pt content of about 5 at.% with a thickness of 80μm and an interdiffusion zone at the bond coat - CMSX4 interface which is on average 19μm thick (see fig. 4.4)

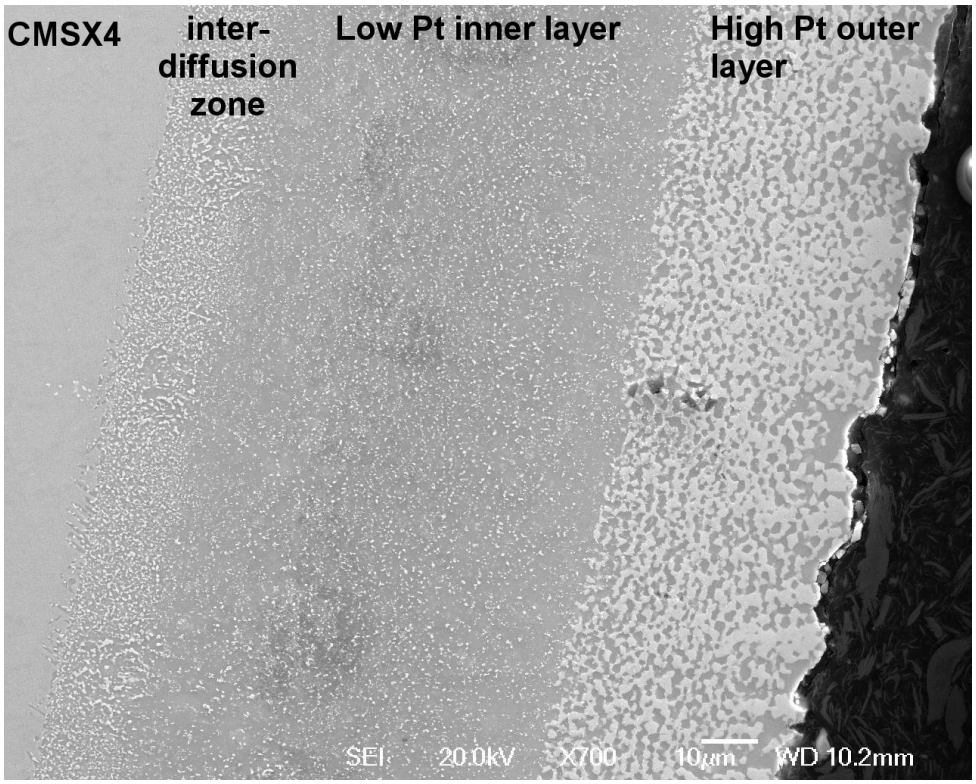

Figure 4.4: Cross section BSE micrograph, showing the typical morphology of the as received high Pt specimens.

Specimen chemistry

The bond coat had a very high platinum content: the phases formed are $PtAl_2$ and $NiAl$. It had roughly two different layers. The outer layer had a high platinum content and showed the two phase structure, the inner layer was low in platinum, with the platinum content decreasing towards the bond coat/substrate interface. A typical analysis is given in table 4.3.

The chemical composition of these different zones and phases is shown in figure 4.5. superimposed in the ternary diagram [6]. For the purpose of bringing an analysis that contains considerably more than 3 elements into a ternary diagram, all elements other than aluminium and platinum have been added to nickel. Typical microstructures are shown in figures 4.4 and 4.6.

ξ - $PtAl_2$		β - $NiAl$ (outer layer)		β - $NiAl$ (inner ayer)	
Element	Atomic %	Element	Atomic %	Element	Atomic %
Al	55.8	Al	46.3	Al	49.6
Cr	3.3	Cr	9.3	Cr	1.1
Co	2.1	Co	3.4	Co	5.9
Ni	16.6	Ni	19.0	Ni	42.0
Pt	22.2	Pt	13.7	Pt	1.3

Table 4.3: Typical analysis for bond coat phases in the outer and inner layer of the high Pt coating.

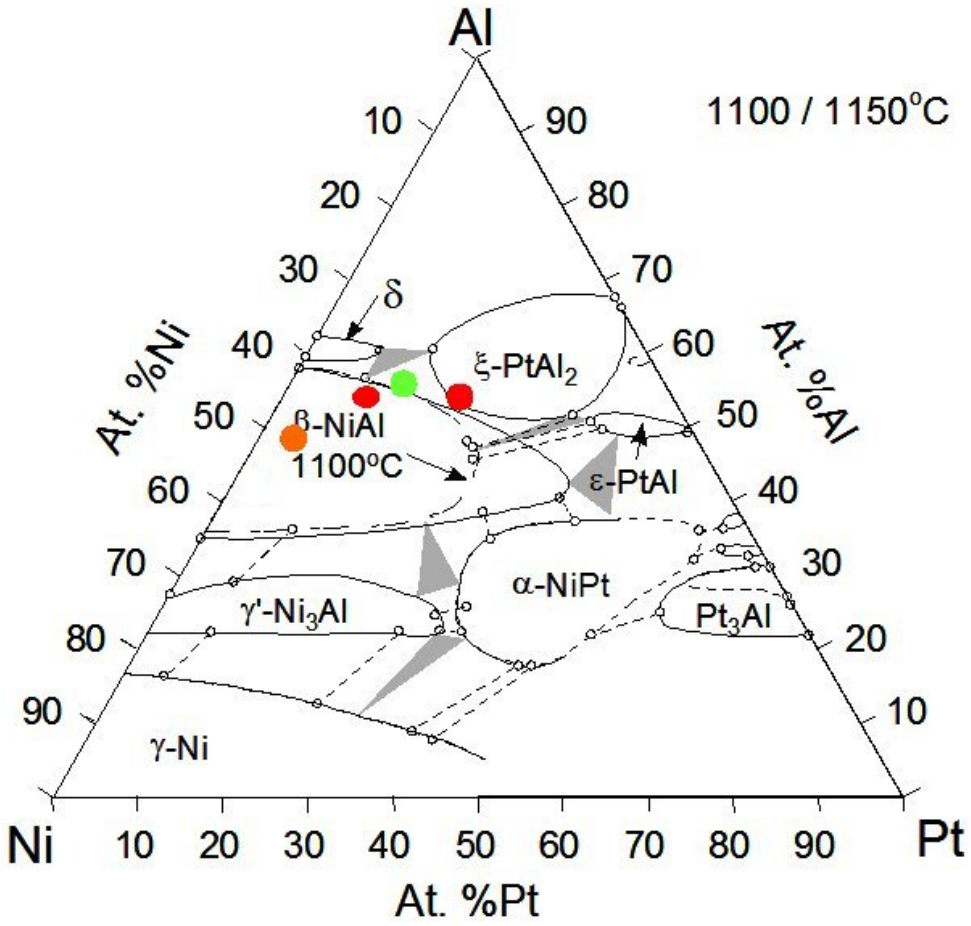

Figure 4.5: Ternary Ni-Al-Pt diagram of Gleeson et al [6]. Indicated in green is the bulk composition of the outer layer of the coating. The red dots show the composition of the $NiAl$ and $PtAl_2$. The orange dot shows the composition of the second layer, with a significant decrease in platinum.

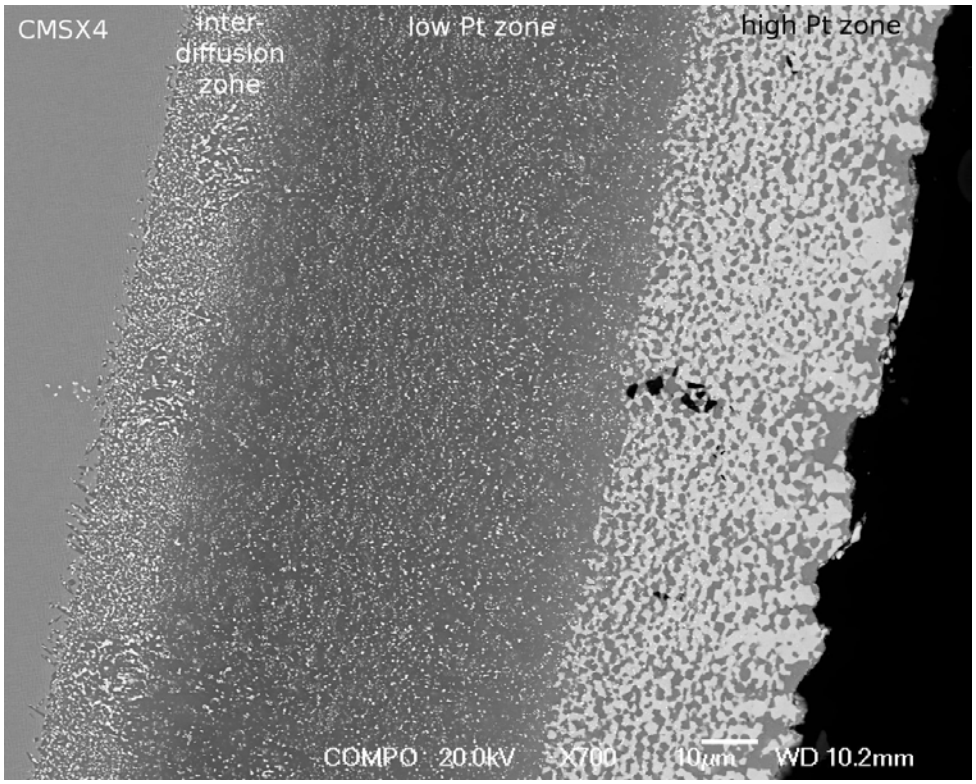

Figure 4.6: BSE cross-section showing the as received condition of the high Pt specimen.

As can be seen in figure 4.6 the low Pt zone exhibits quite a large amount of very small precipitates, the largest of which are about 0.4μm. They are high in chromium, but too small to get a reliable EDX analysis of them in the SEM. The grain size of the $PtAl_2$ and $NiAl$ grains within the outer high Pt layer ranges between 4.1μm at the outside and 0.7μm at the interface between high and low Pt zone.

4.2 SEM characterisation of oxide surfaces

After the oxidation experiments described in the chapter on experimental procedure the oxide surfaces were characterised by SEM imaging. The markers '$\beta - grain$', '$\gamma' - grain$' and 'grain boundary' in the micrographs below always refer to the underlying bond coat phases, not to the oxide layer actually depicted.

4.2.1 Low Pt specimens

Preliminary testing

A first preliminary oxidation test on the low Pt specimens was made for 10 minutes at 1100°C. The surface of the specimen away from the bond coat was marked with scratches and micrographs were taken of the whole length of the bond coat, to select a distinct Ni_3Al grain before oxidation. The marks were deep enough to still be identified, even under a continuous oxide layer. Investigation after oxidation showed that after such a short period of time at temperature the the bond coat grains below the oxide layer could be easily identified, since the morphology of the oxide was different depending on the underlying bond coat phase and phase boundaries (see figures 4.7 and 4.8) No high resolution images were taken at this stage.

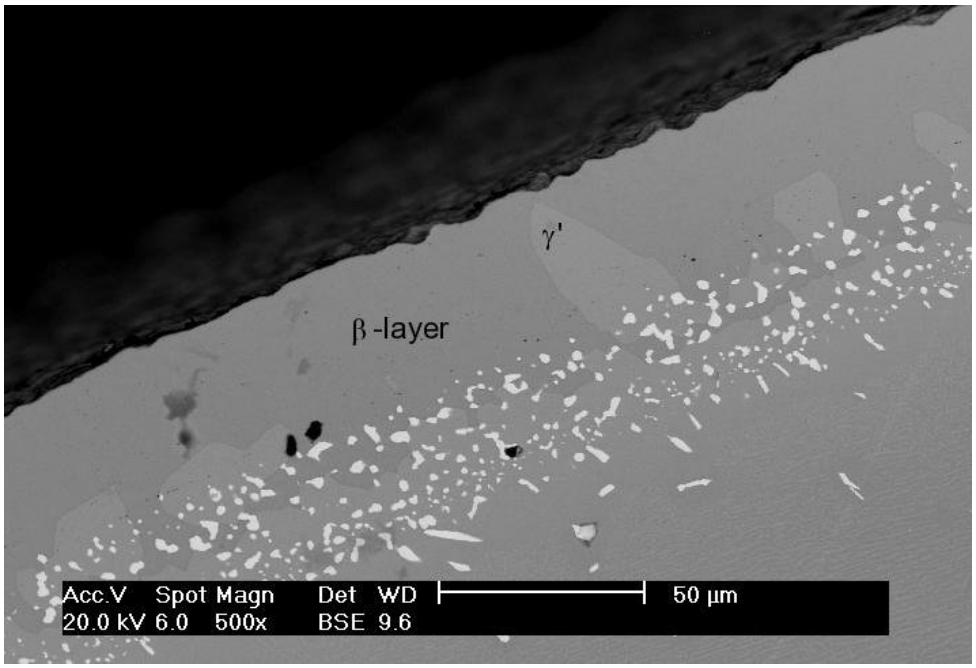

Figure 4.7: BSE micrograph of the Ni_3Al grain marked for re-identification after oxidation for 10 min at 1100°C.

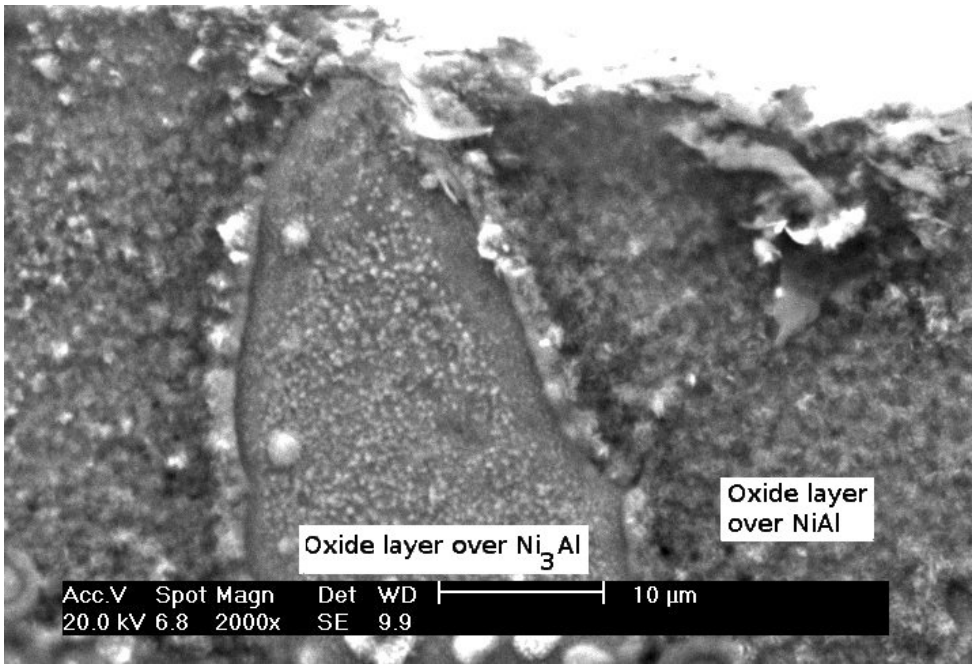

Figure 4.8: The difference in oxide morphology clearly shows the outline of the underlying bond coat phases, as well as the phase boundary.

After this first testing the use of scratch-marks was deemed unnecessary and therefore no longer utilised.

Oxidation for 3 minutes at 1100°C

SEM micrographs taken after oxidation testing for 3 minutes at 1100°C revealed that already after such a short time at temperature a continuous oxide layer is formed. High resolution imaging shows the distinct difference in oxide morphology, depending on the underlying bond coat phase. Even after such short times at temperature cracking and spalling was observed in some specimens.

Figures 4.9 to 4.16 all show a plan view of the oxide layer. Figure 4.9 gives a good overview, the right hand side of the micrograph shows the typical morphology of oxide grown on top of a γ'-grain, flat rectangular grains forming a continuous layer, with some grains protruding over it. The left hand side shows the typical platelet shaped oxide grains,which grow over β-grains. These platelets are either arranged like roof tiles or as whiskers.

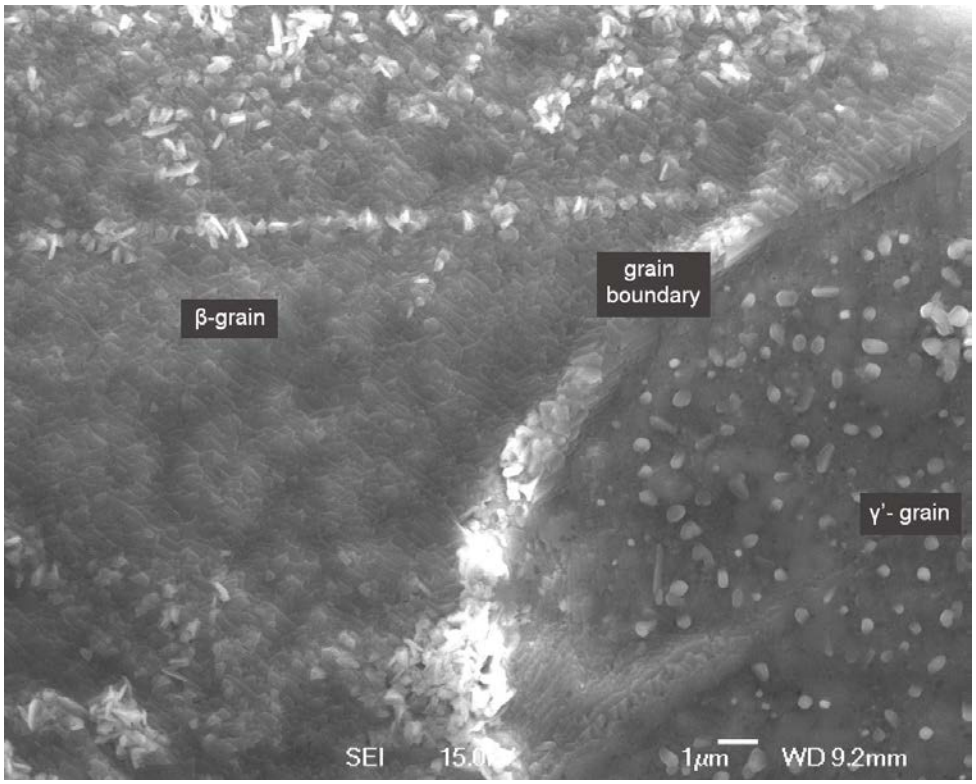

Figure 4.9: SE image giving an overview of the oxide layer after 3 minutes at temperature.

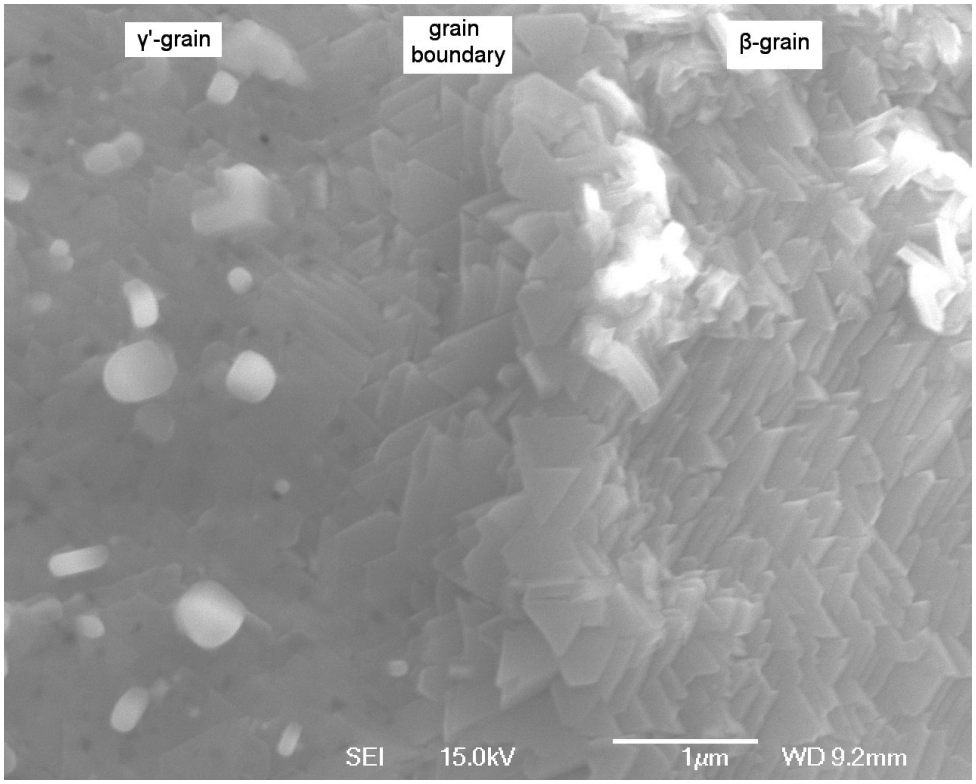

Figure 4.10: High resolution SE image showing a more detailed view of the oxide layer on top of a phase boundary between $NiAl$ and Ni_3Al.

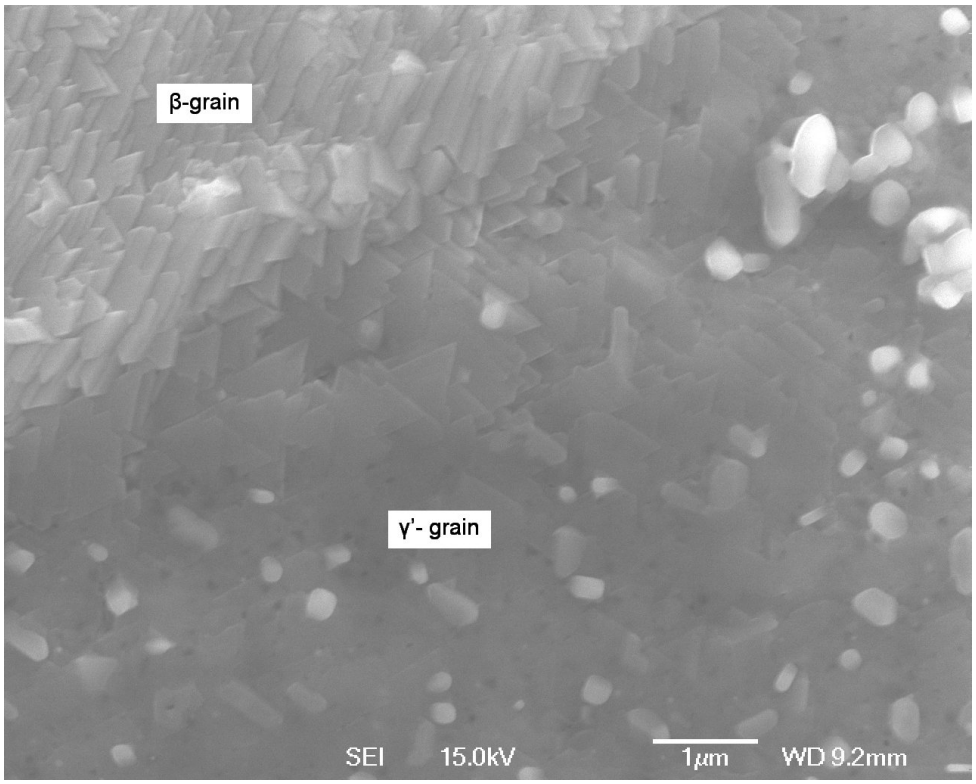

Figure 4.11: Clearly visible in the top part of this micrograph is the roof tile like arrangement of the oxide growing on top of $NiAl$, in contrast to the larger rectangular oxide growing on top of Ni_3Al.

High resolution imaging reveals more details of the oxide morphology along phase boundaries between $NiAl$ and Ni_3Al in the bond coat. Phase boundaries between these phases typically grow ridges of oxide platelets as can be seen in figures 4.9 and 4.10. The oxide grown on grain boundaries between $NiAl$ grains do not exhibit any distinct features, but the shape of the oxide platelets grown on different $NiAl$ grains varies slightly (see fig. 4.12).

Figure 4.12 also shows one of the larger spalled areas, which occur even after short times at temperature (in this particular case 3 minutes). Cracks within the oxide layer can be seen in fig. 4.13.

As an additional tool to identify the bond coat phases underneath the thin oxide layer, sets of SE and BSE images were taken from the same area. The oxide layer is thin enough for the composition of the underlying phases to be seen in the BSE mode (see figures 4.14 and 4.15).

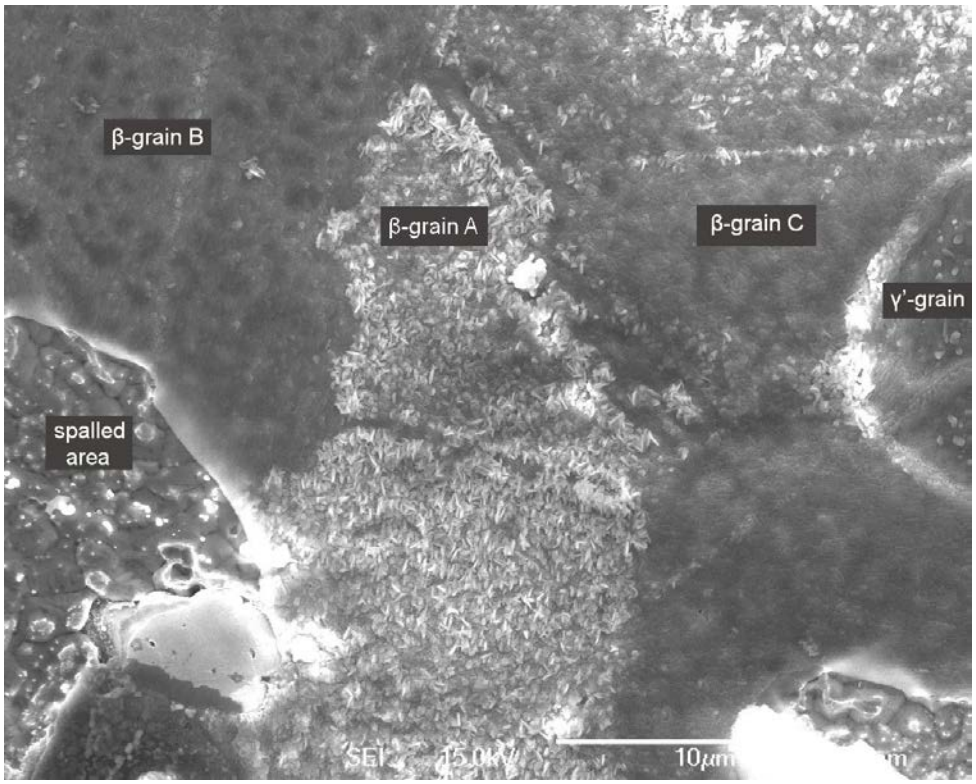

Figure 4.12: Overview of the oxide layer grown on different bond coat phases. On the left hand side is a quite large spalled area.

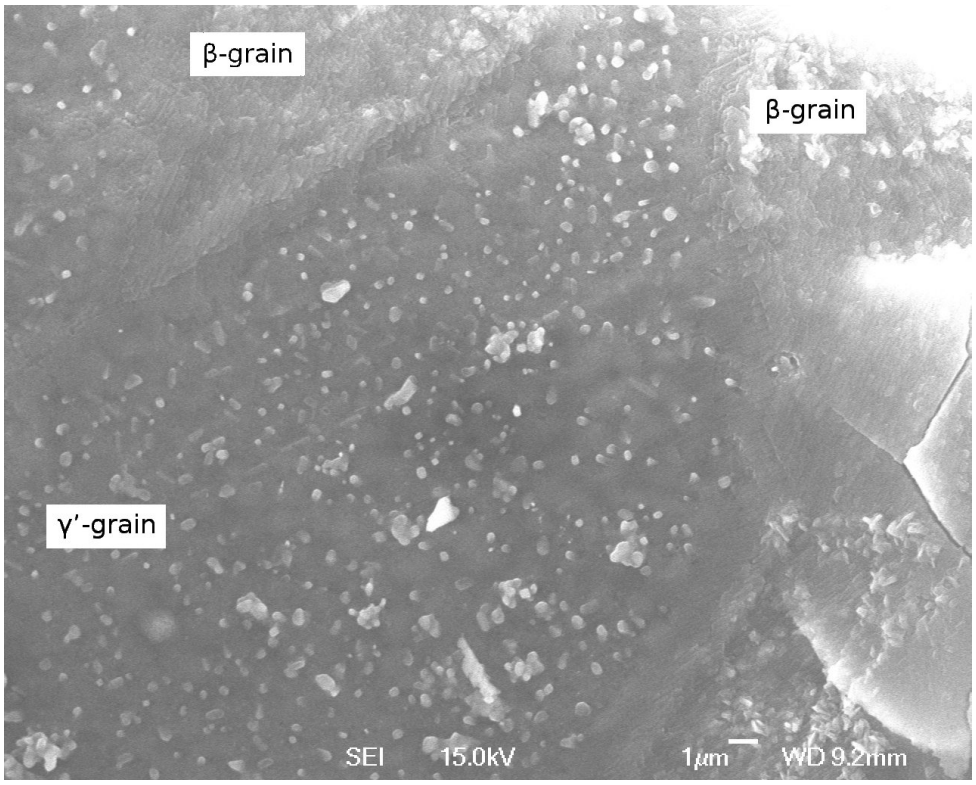

Figure 4.13: Typical oxide morphology of oxide growing on Ni_3Al. On the right hand side the micrograph shows cracks in the oxide layer; in this particular case within oxide grown on $NiAl$.

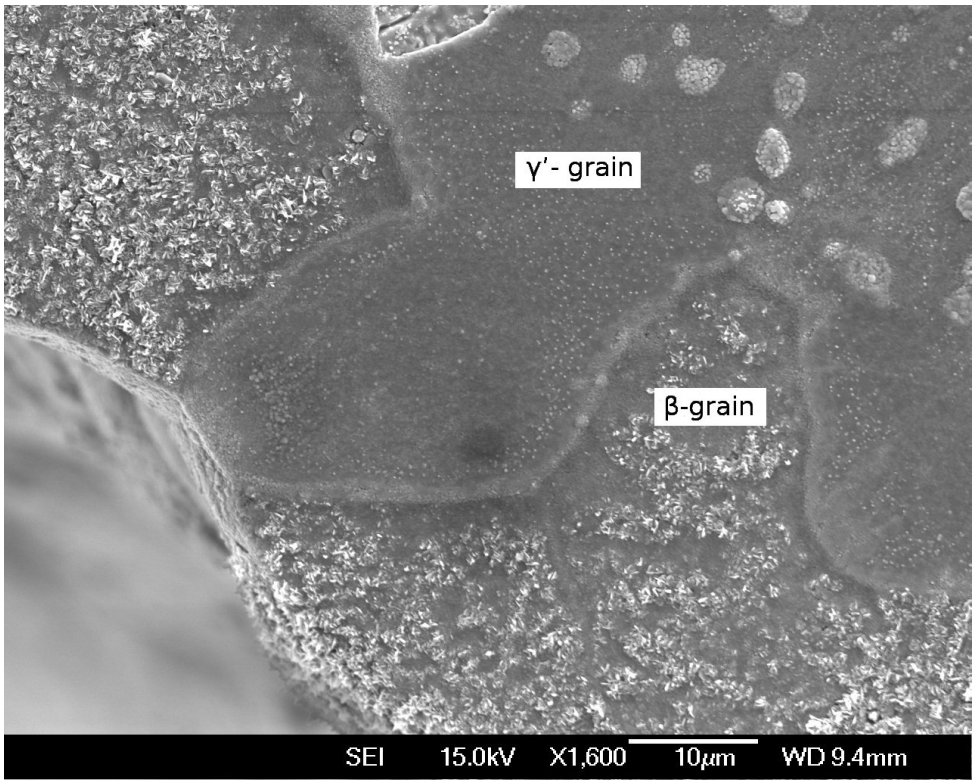

Figure 4.14: SE micrograph showing an overview of the oxide layer grown on different bond coat phases.

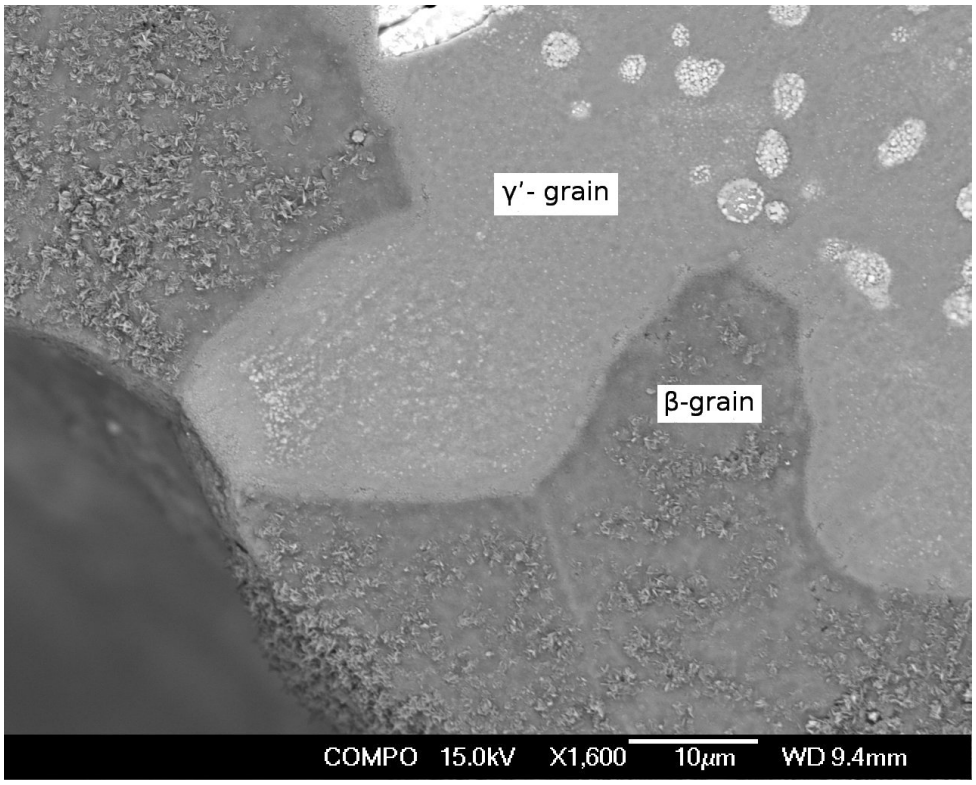

Figure 4.15: BSE micrograph of the same area than fig. 4.10. The difference in contrast showing the composition of of the underlying bond coat phases is visible through the thin oxide layer making them easy to identify.

Oxidation for 7 minutes at 1100°C

After oxidation for 7 minutes at 1100°C the oxide morphology changes slightly, but there is still a distinct difference between oxide growing on $NiAl$ and oxide growing on Ni_3Al. The oxide on top of $NiAl$ still grows into platelets about 250nm in diameter that form clusters on slightly larger (450nm) rectangular grains (fig. 4.16). In the oxide grown on top of Ni_3Al individual oxide grains can not be easily distinguished from SEM imaging (figures 4.17 and 4.18). The surface of the oxide layer on top of Ni_3Al shows a number of small voids (see fig. 4.16, 4.17 and 4.19 - 4.21). There are also larger voids that can be seen through out the oxide layer, which maybe connected to small scale spallation or pre-existing voids within the bond coat (see fig. 4.16).

The identification of bond coat phases below the oxide layer with BES imaging becomes less indicative due to the thicker oxide layer, but there is still sufficient amount of back scattered electrons from the bond coat reaching the detector to confirm which bond coat phase lies beneath a certain type of oxide (figures 4.20 and 4.21).

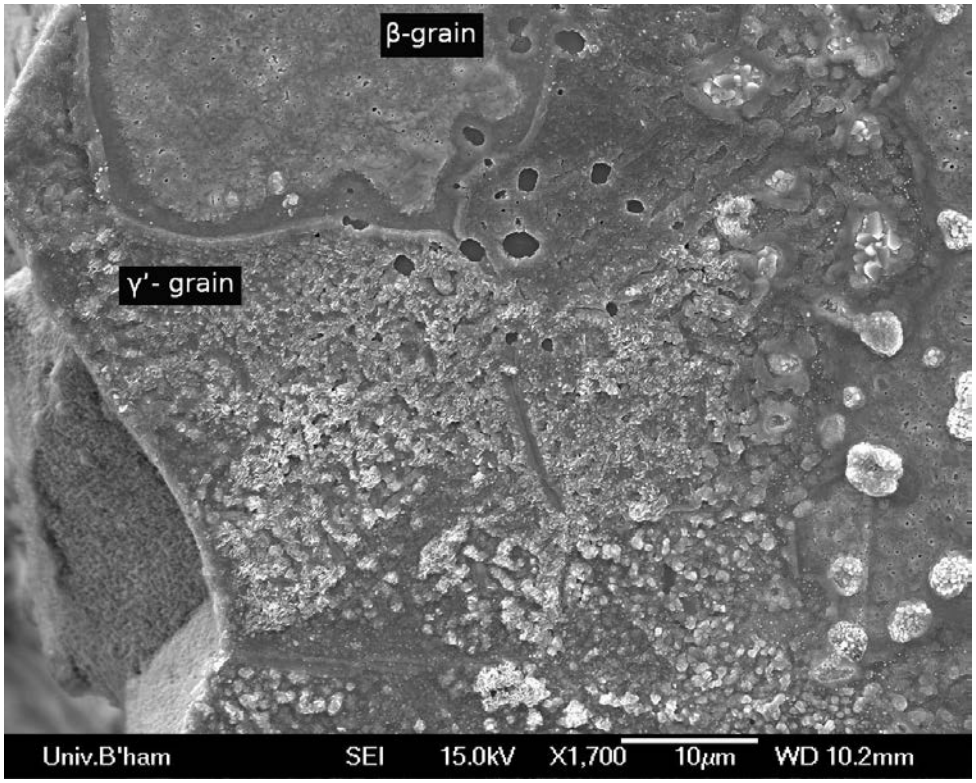

Figure 4.16: SE micrograph showing an overview of the oxide growing on different bond coat phases after oxidation for 7 minutes at 1100°C.

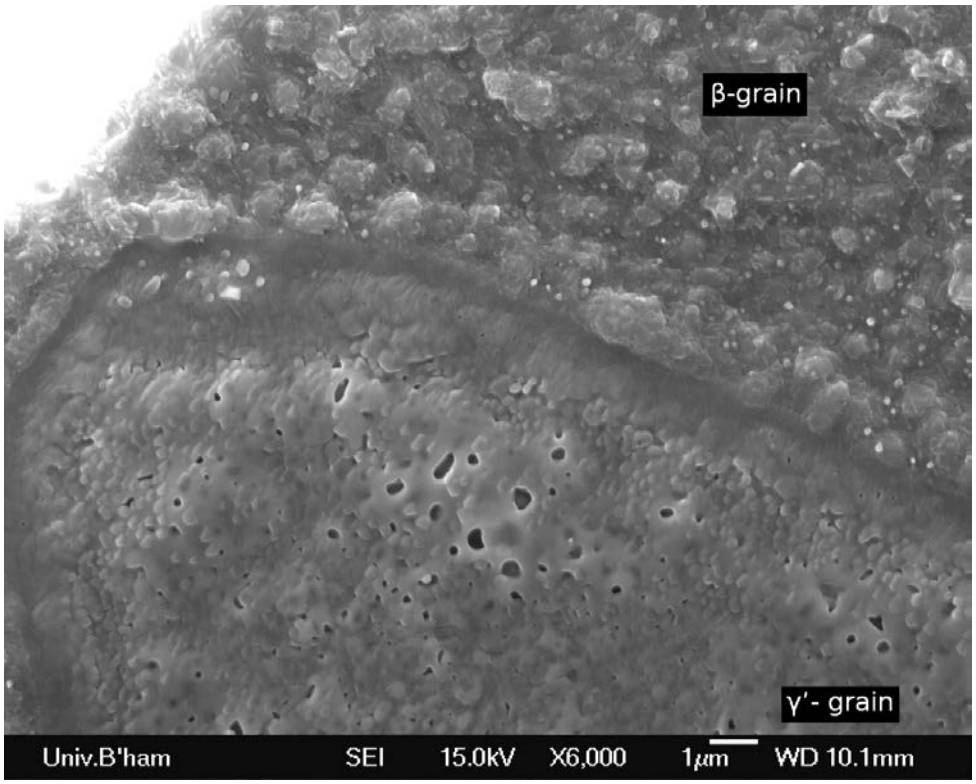

Figure 4.17: SE micrograph showing the distinct difference in oxide morphology between oxide grown on $NiAl$, Ni_3Al and along phase boundaries.

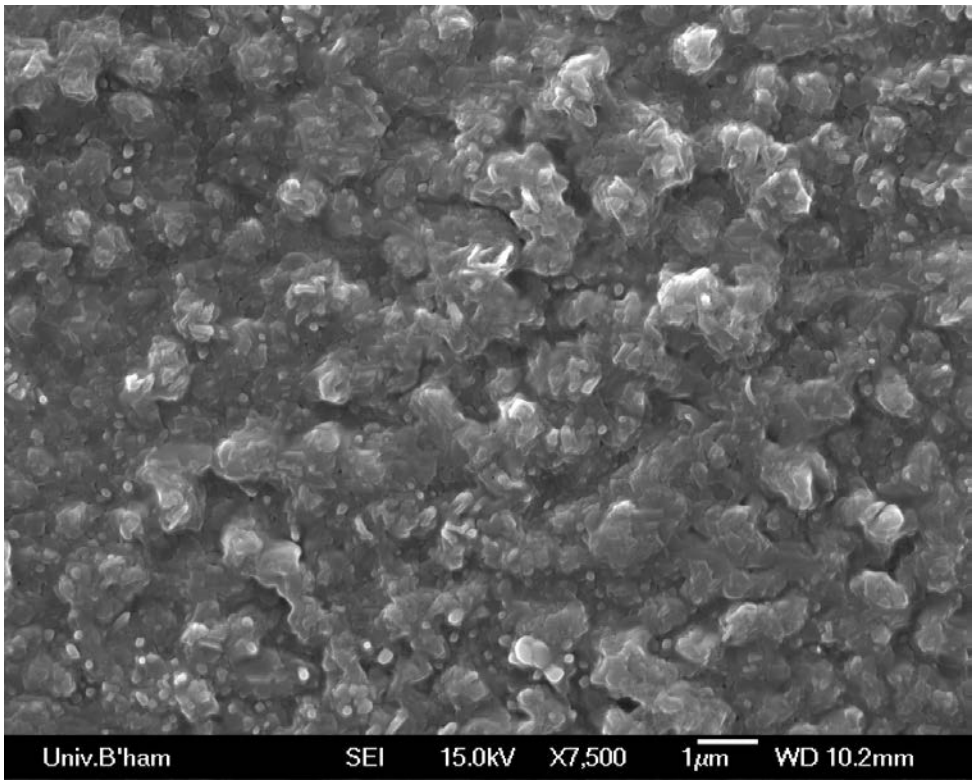

Figure 4.18: High resolution image of oxide grown on a β-grain.

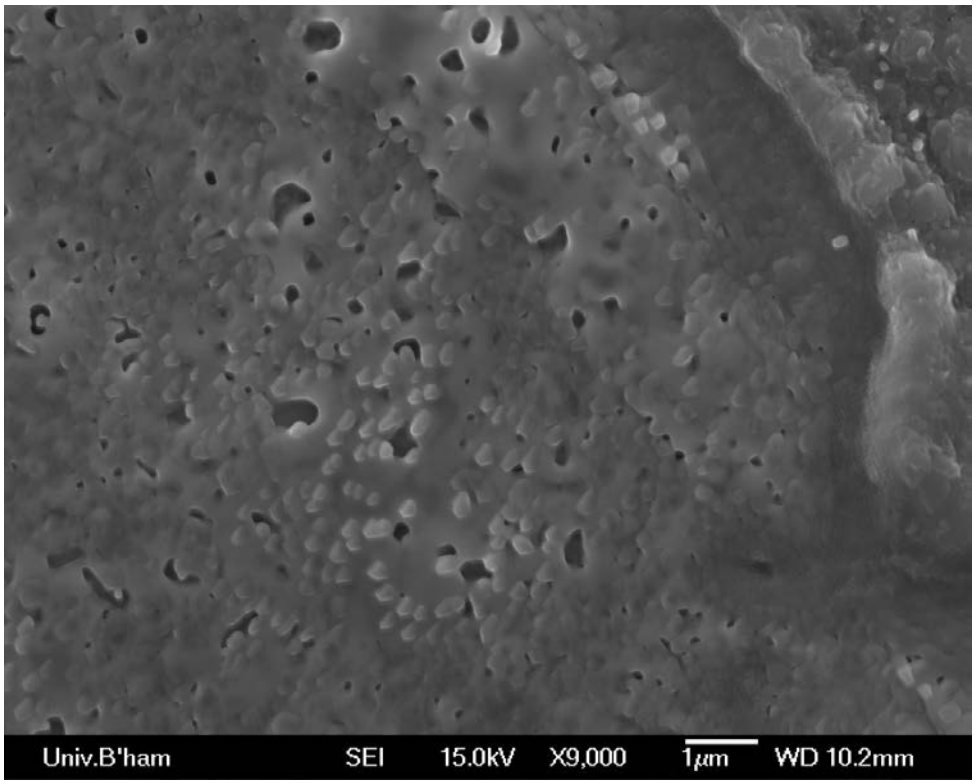

Figure 4.19: High resolution image of oxide grown on a γ'-grain.

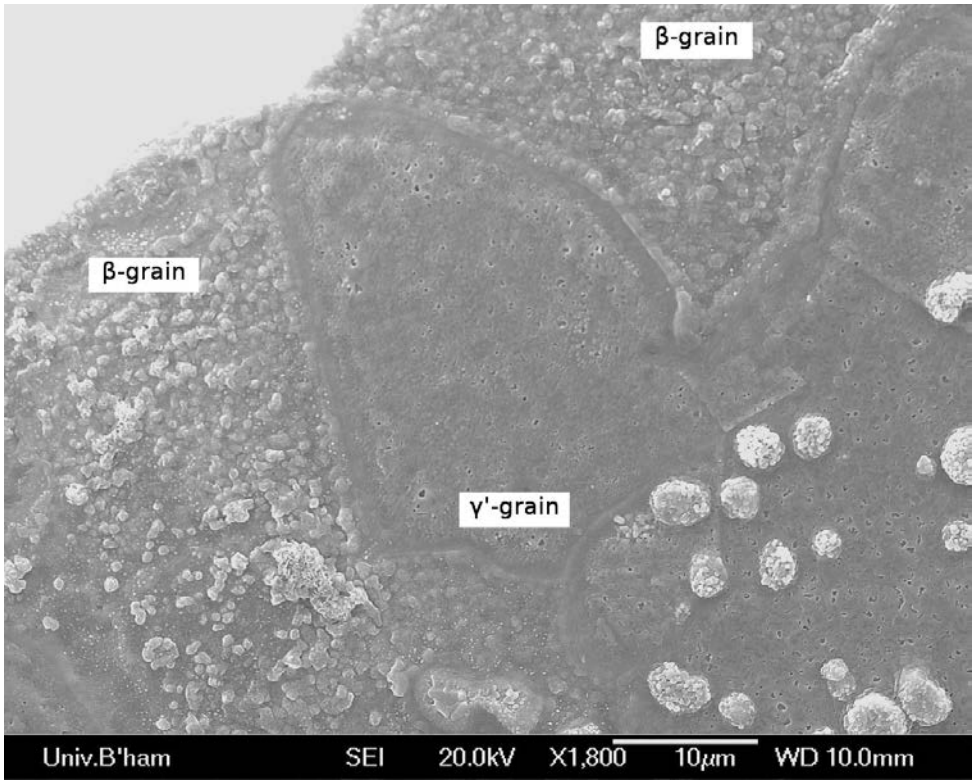

Figure 4.20: Overview of the Oxide layer growing on $\beta - NiAl$ grains and a $\gamma' - Ni_3Al$ grain.

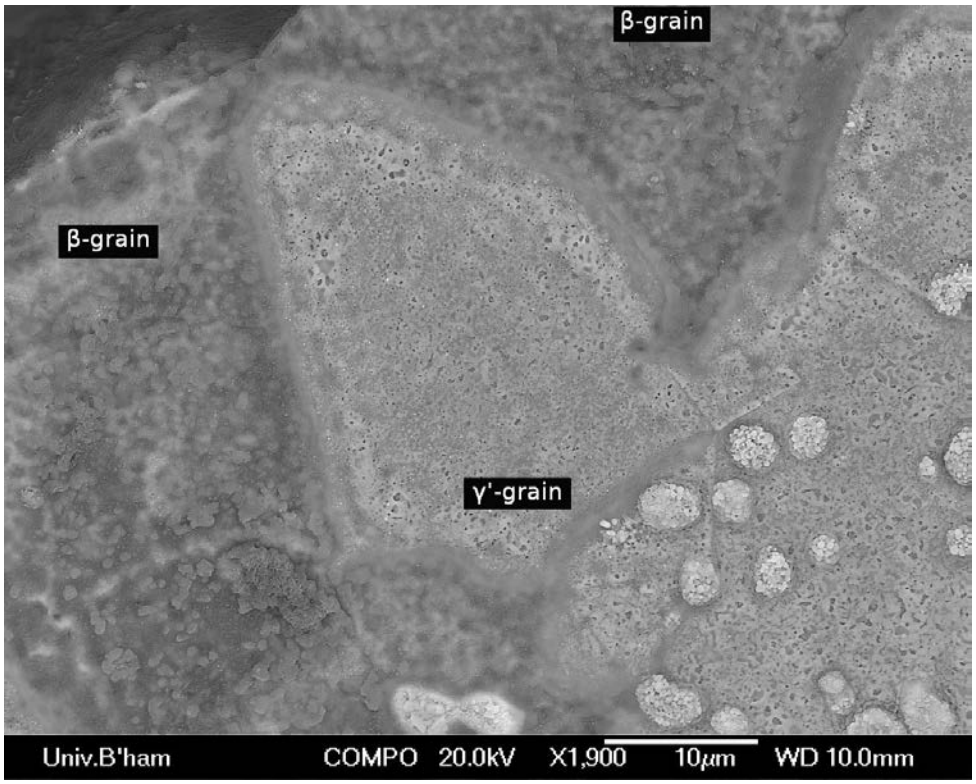

Figure 4.21: BSE micrograph showing the composition of the underlying bond coat phases, through the oxide layer.

4.3 High Pt specimens

4.3.1 Oxide morphology

Oxidation for 3 minutes

The oxide layer growing on top of the high Pt bond coat after 3 minutes at 1100°C is also continuous, like on the low Pt specimens. There is less spallation in comparison to the low Pt specimens and the spalled areas are mainly on top of the interdiffusion zone at the bond coat/super alloy interface (see overview in figure 4.22).

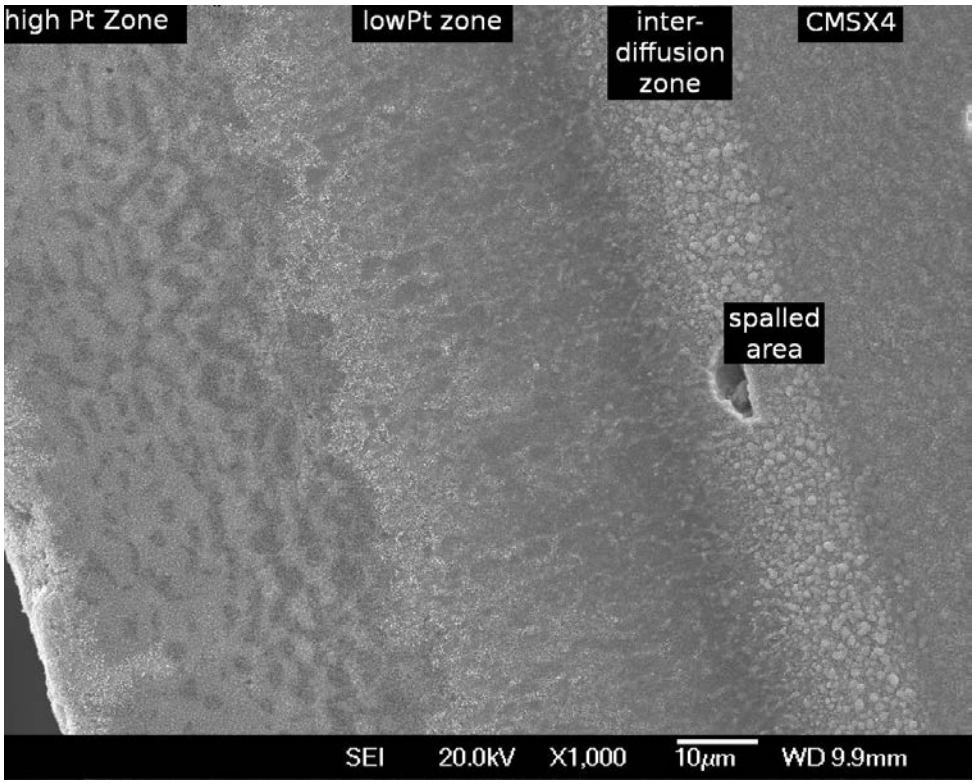

Figure 4.22: Overview over the oxide layer grown on top of the high Pt coating after 3 minutes at temperature.

After 3 minutes at temperature the two phase structure of the underlying bond coat can be seen through the thin oxide layer (see figures 4.22 and 4.23). There are no differences in oxide morphology between the two phases of the outer, high Pt, layer of the coating. On both $NiAl$ and $PtAl_2$ the oxide grows into platelets and whiskers, very similar to the oxide growing on top of $NiAl$ in the low Pt specimens (figures 4.23 and 4.24). The platelets are between 260nm and 70nm in diameter.

This morphology changes slightly with decreasing platinum and aluminium content within the inner, low PT, layer of the coating. Here the oxide grains are angular, forming a more even layer without any protruding whiskers (see figures 4.25 and 4.26). The grain size varies between 340nm for the larger and 50nm for the smaller ones.

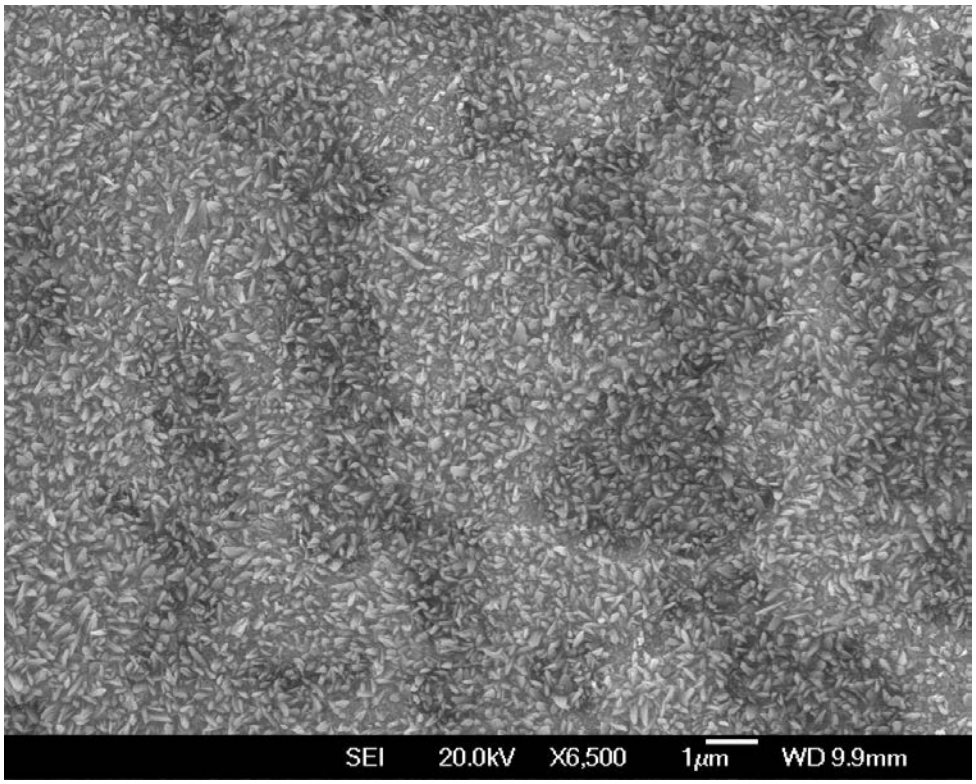

Figure 4.23: SE image of the oxide morphology on top of the outer, hi Pt, bond coat layer. The oxide grows in whiskers, similar to the oxide growing on NiAl on the low Pt specimens.

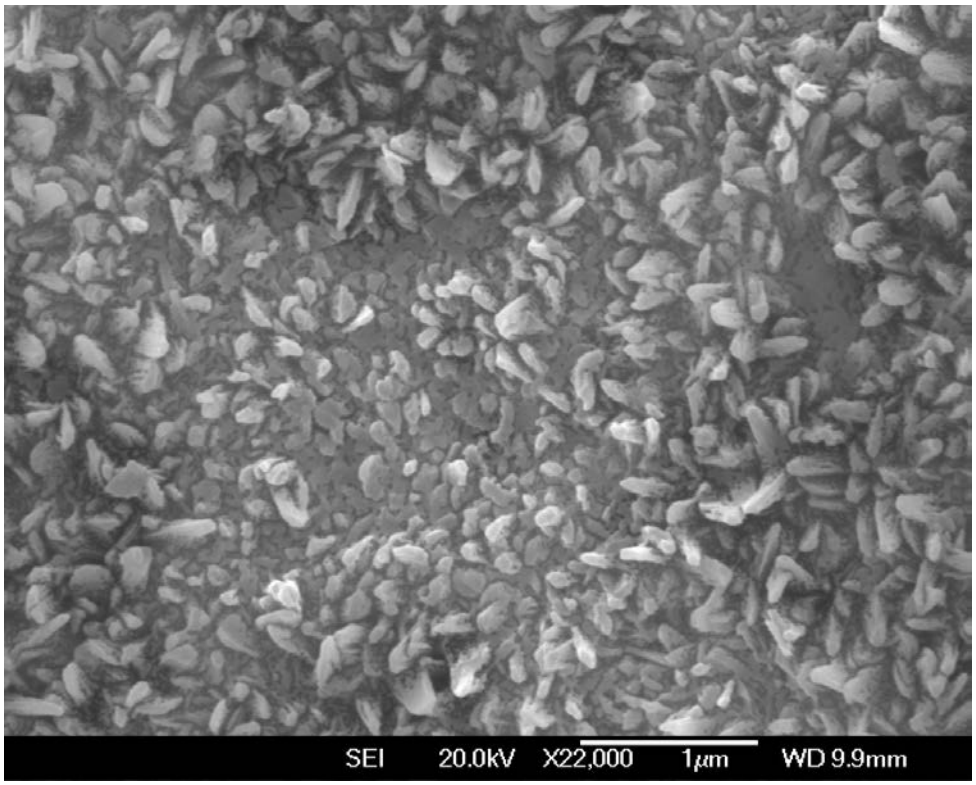

Figure 4.24: High magnification image of the oxide grown on the high Pt zone of the bond coat, showing the platelet and whisker shape of the oxide crystals.

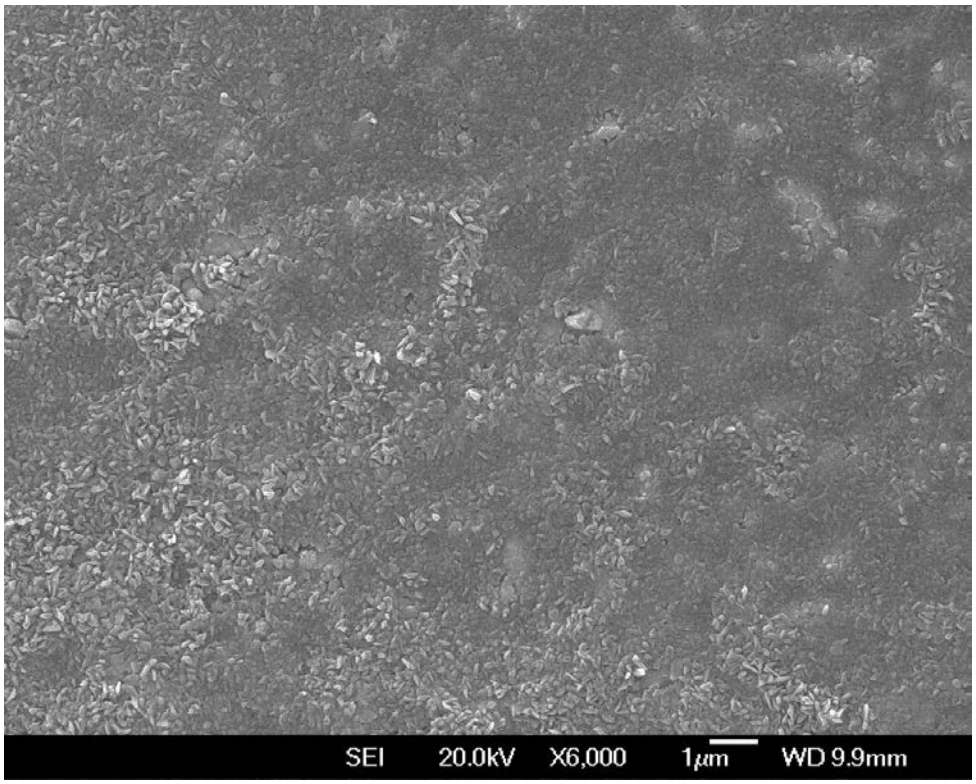

Figure 4.25: Oxide grown on top of the inner, low Pt, zone of the bond coat, showing larger, more angular grains as compared to the oxide growing on the high Pt zone.

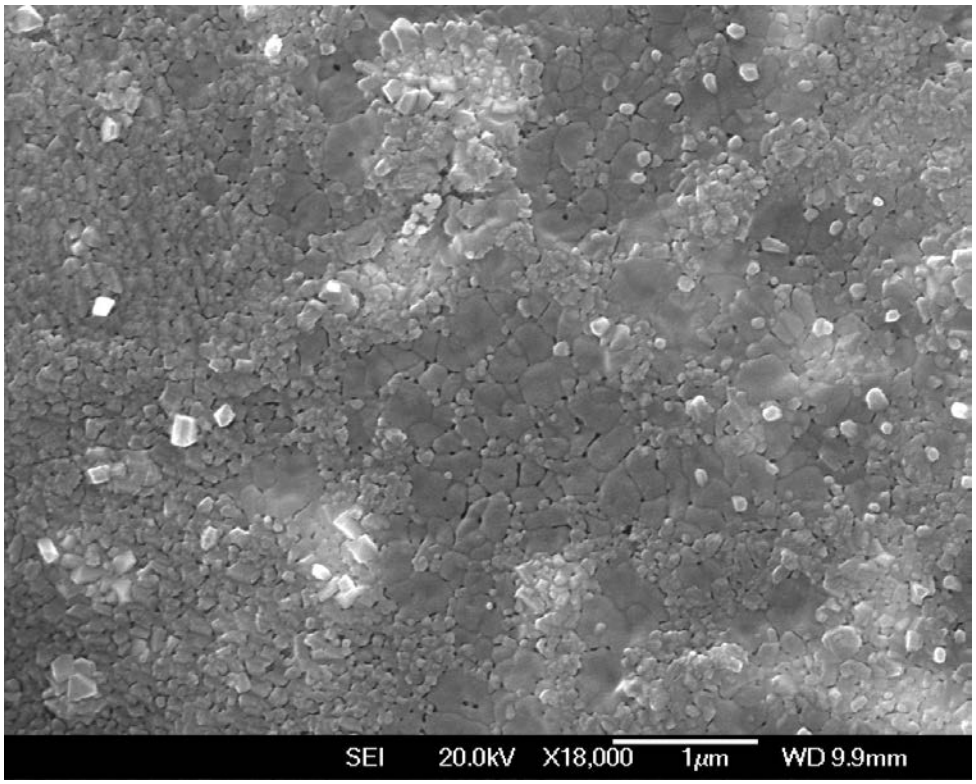

Figure 4.26: High magnification image of the oxide grown on the low Pt zone of the bond coat.

Oxidation for 10 minutes

After oxidation for 10 minutes at 1100°C the over all oxide morphology does not change significantly. The oxide growing on the high Pt zone of the coating forms platelets and whiskers and the oxide growing on the low Pt zone forms rectangular grains. There is more spallation and the formation of small voids within the oxide layer (see figure 4.27).

The structure of the underlying bond coat can no longer be seen through the oxide layer as was the case after 3 minutes at temperature.

Figures 4.28 to 4.31 show higher magnification micrographs of the oxides. In Figure 4.28 the platelet and whisker morphology of the oxide on the high Pt outer zone can be seen. The interface between high and low Pt zone can not be clearly defined, there is a gradual change in oxide morphology. The white arrows in figure 2.29 indicate the likely location of the interface. Figures 4.30 and 4.31 show the oxide morphology on top of the interdiffusion zone and the CMSX4 substrate.

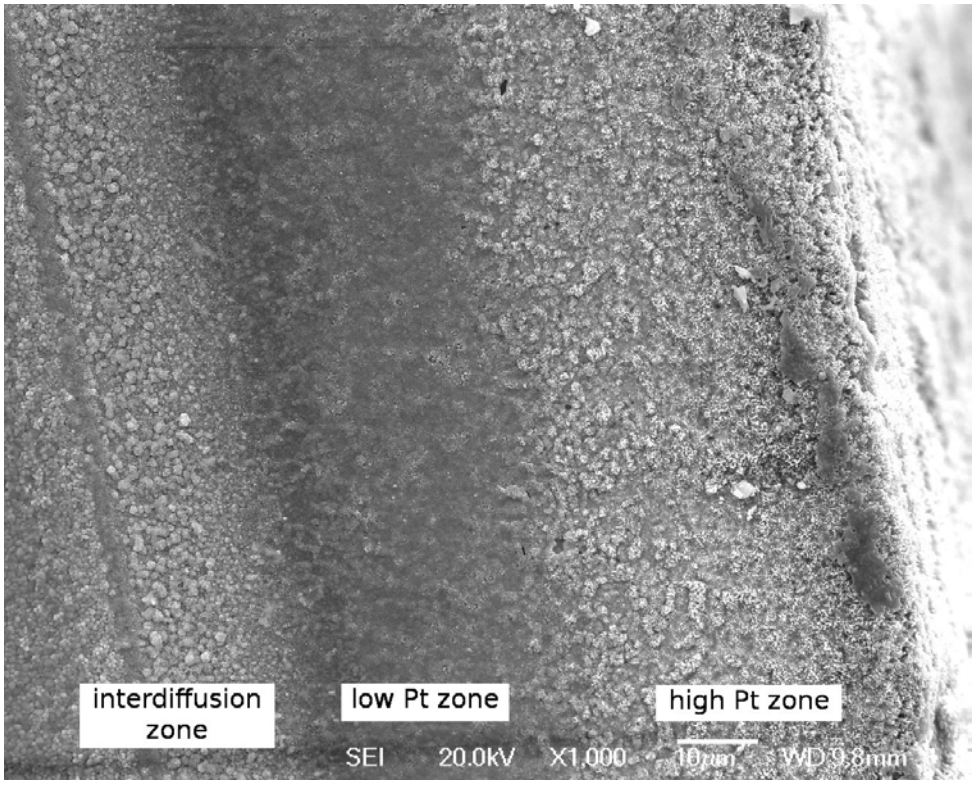

Figure 4.27: Overview after 10 minutes at 1100°C

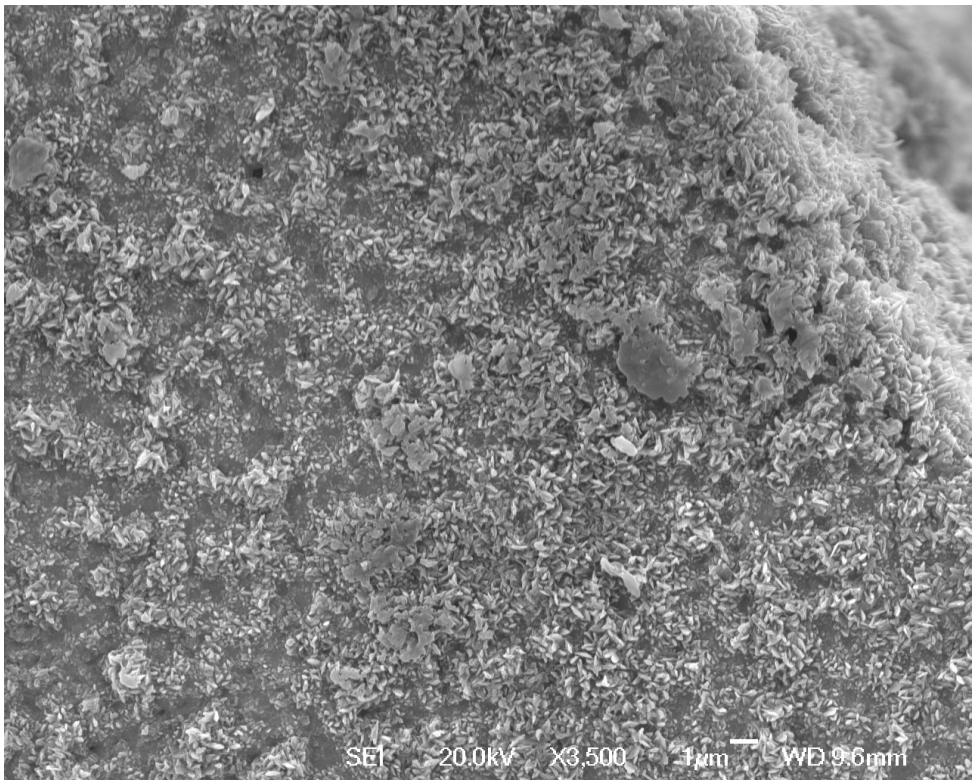

Figure 4.28: Oxides grown on top of the high Pt zone, forming whiskers and platelets.

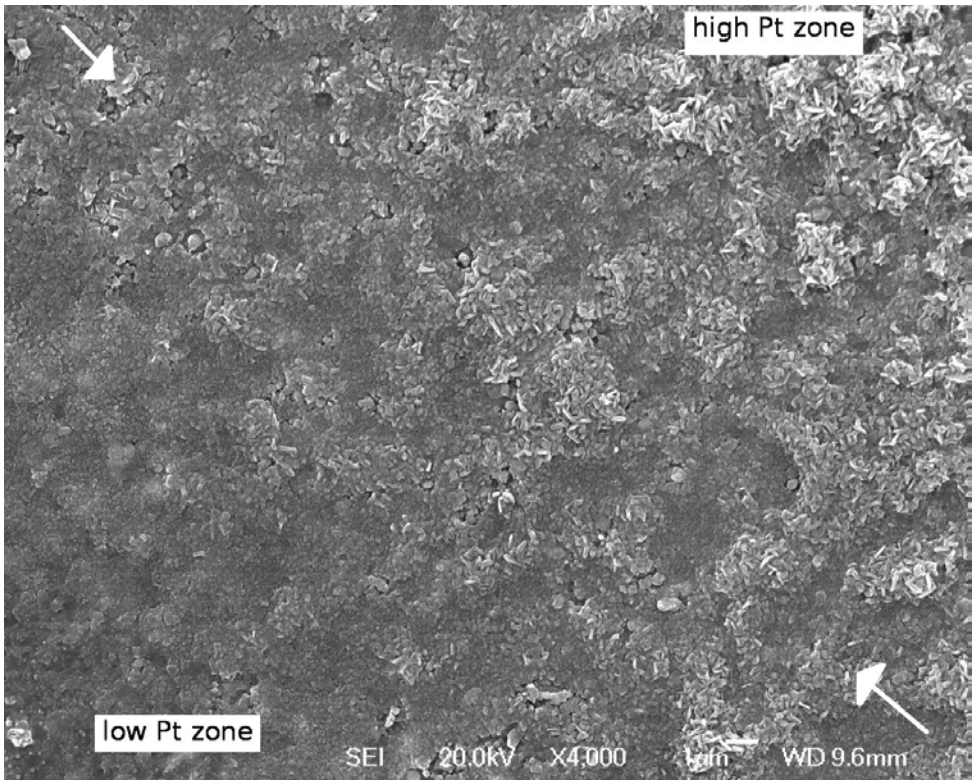

Figure 4.29: Oxides growing on top of the high Pt/low Pt zone interface. The interface runs from the top left corner of the image to the bottom right corner. The top right part of the image shows the whiskers typical for oxide grown on the high Pt zone. Towards the bottom left corner the oxide morphology gradually changes to smaller angular grains, typical for oxide grown on the low Pt zone. Throughout the area are small voids within the oxide layer. The white arrows indicate the course of the interface.

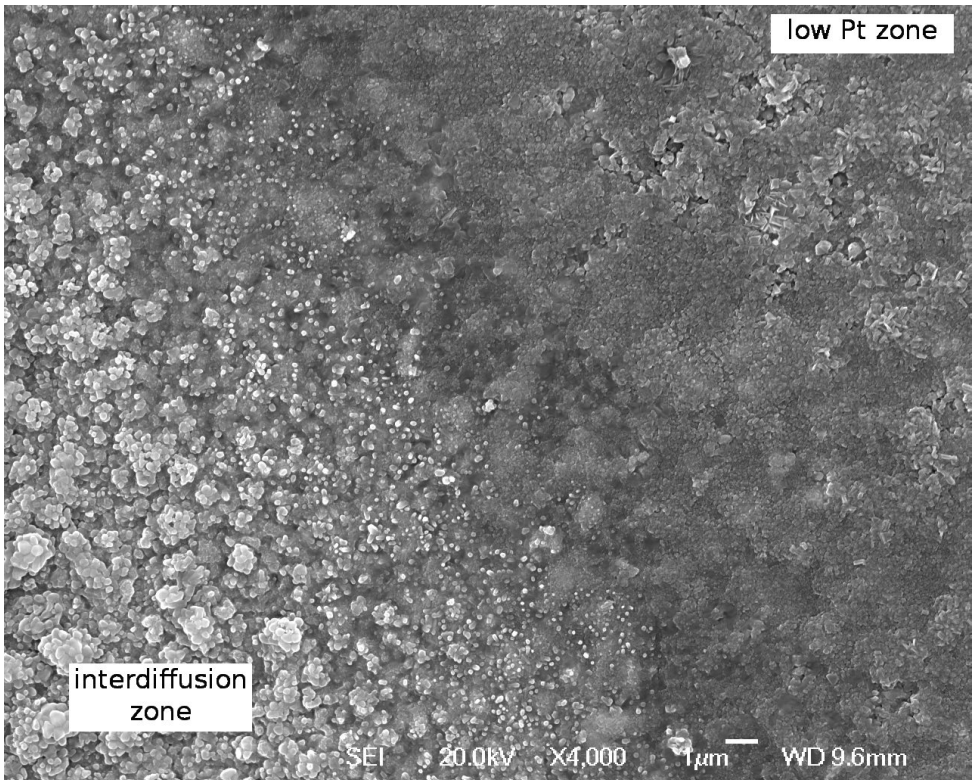

Figure 4.30: Oxide morphology on top of the interdiffusion zone and low Pt zone.

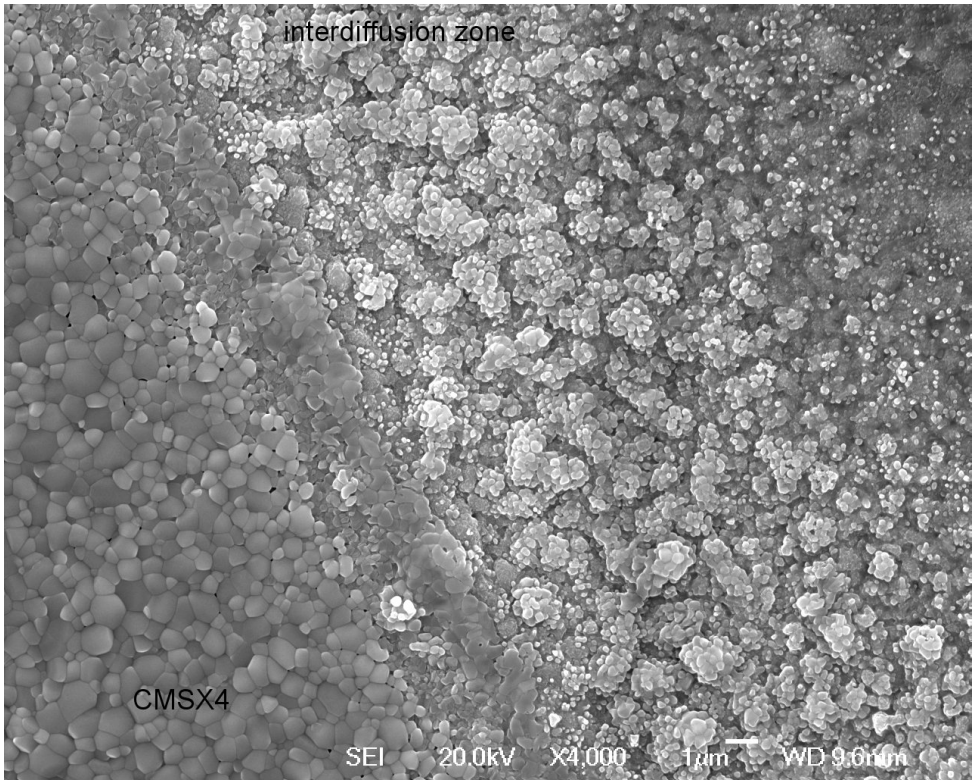

Figure 4.31: Oxide morphology on top of the super alloy (CMSX4) and the interdiffusion zone

4.4 An investigation of the behavior of high-Pt bond coats at 1100°C

With the high-Pt specimens a further series of experiments was carried out in order to investigate the development of the bond coat with increasing aluminium depletion. The specimens were cut and polished as described above and then oxidised at 1100°C for different times. Starting with 1 hour, then 5, 10, 15, 20, 25, 50, 75 and 100 hours. The aim was to compare these experimental results with the well known ternary Ni-Al-Pt diagram by Gleeson et al [6] (see figure 2.11), since most experiments so far have been carried out in the low platinum section of said diagram.

After the oxidation experiments, the samples were sectioned and investigated in an SEM for imaging and EDX analysis. These results are going to be presented in this section.

4.4.1 Bond coat development as observed with BSE imaging and EDX analysis

1 hour at 1100°C

As can be clearly seen from figure 4.32, after 1 hour of oxidation at 1100°C, the morphology of the bond coat is not very different from the as received specimens (compare with figure 4.4), the chemistry however is already different, due to aluminium depletion. The bond coat still consists of 2 different layers: (a) an outer high-Pt zone with the 2 $NiAl$ phases, that differ in platinum content. A high-Pt one, which looks white in figure 4.32 and a phase with lower platinum content, which appears grey in the micrograph. (b) The inner low-Pt zone with $NiAl$ and finely dispersed precipitates on a sub-micron scale. Although too small, to be accurately analysed by EDX, these precipitates are rich in chromium, cobalt and heavy elements like tungsten and rhenium.

The outer zone is on average 115μm thick, the grains on the bond coat/oxide interface are the largest with a diameter up to 10μm. The grain size decreases towards the interface between high- and low-Pt zone, where the average diameter is at 2μm. The inner zone is roughly double the size of the outer zone, with an average thickness of 200μm. No individual grains can be seen with either SE or BSE imaging, therefore no grain size could be determined for this zone.

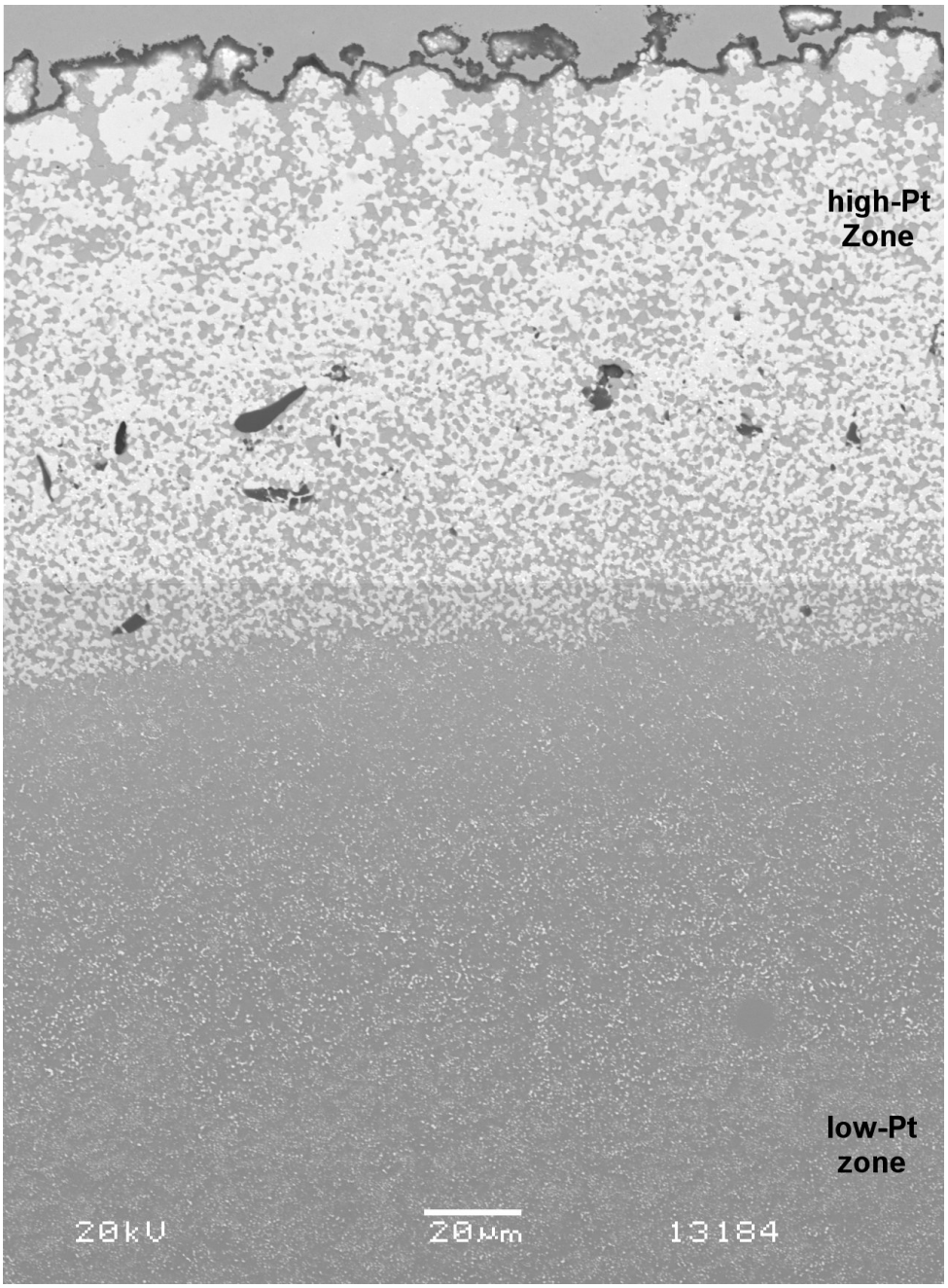

Figure 4.32: BSE micrograph of the high- and low-Pt zone of the bond coat after 1 hour at 1100°C.

A line of EDX analysis from the oxide/bond coat interface to the CMSX4 substrate was taken, to investigate the element distribution throughout the coating (see figure 4.33). The platinum levels in the outer zone of the coating differ, depending which of the two phases is measured. The high-Pt (white) phase has an average platinum content of 18 at.%, the low-Pt (grey) phase has an average platinum content of 11 at.%.

Upon reaching the low-Pt zone of the coating, the overall platinum content decreases continually from an average of 6 at.% at the interface between high- and low-Pt zone to 1 at.% at the interface with the interdiffusion zone.

The nickel content undergoes an opposite development, increasing from an average of 22 at.% at the oxide/bond coat interface to 42 at.% at the interface between low-Pt and interdiffusion zone.

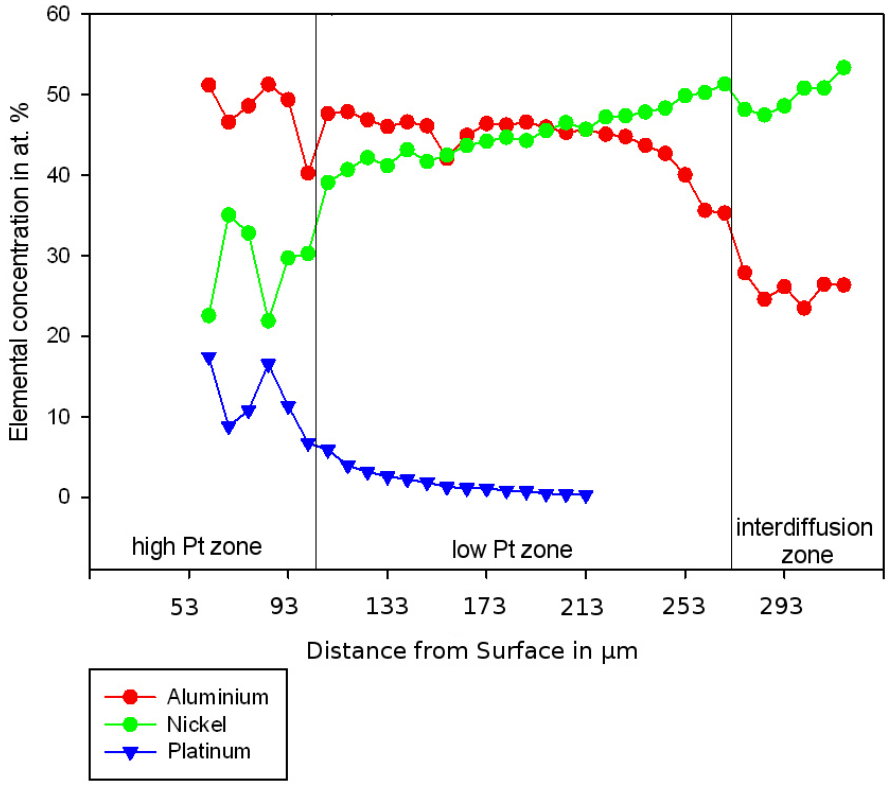

Figure 4.33: Line scan giving the amounts of Al, Ni and Pt from the coating surface to the superalloy, after 1 hour at 1100C.

5 hours at 1100°C

After oxidation for 5 hours at 1100°C the bond coat is still divided into a high- and low-Pt zone (see fig. 4.34). Both zones have grown inwards, the outer high-Pt zone is now 145μm thick, the inner low-Pt zone has an average thickness of 220μm.

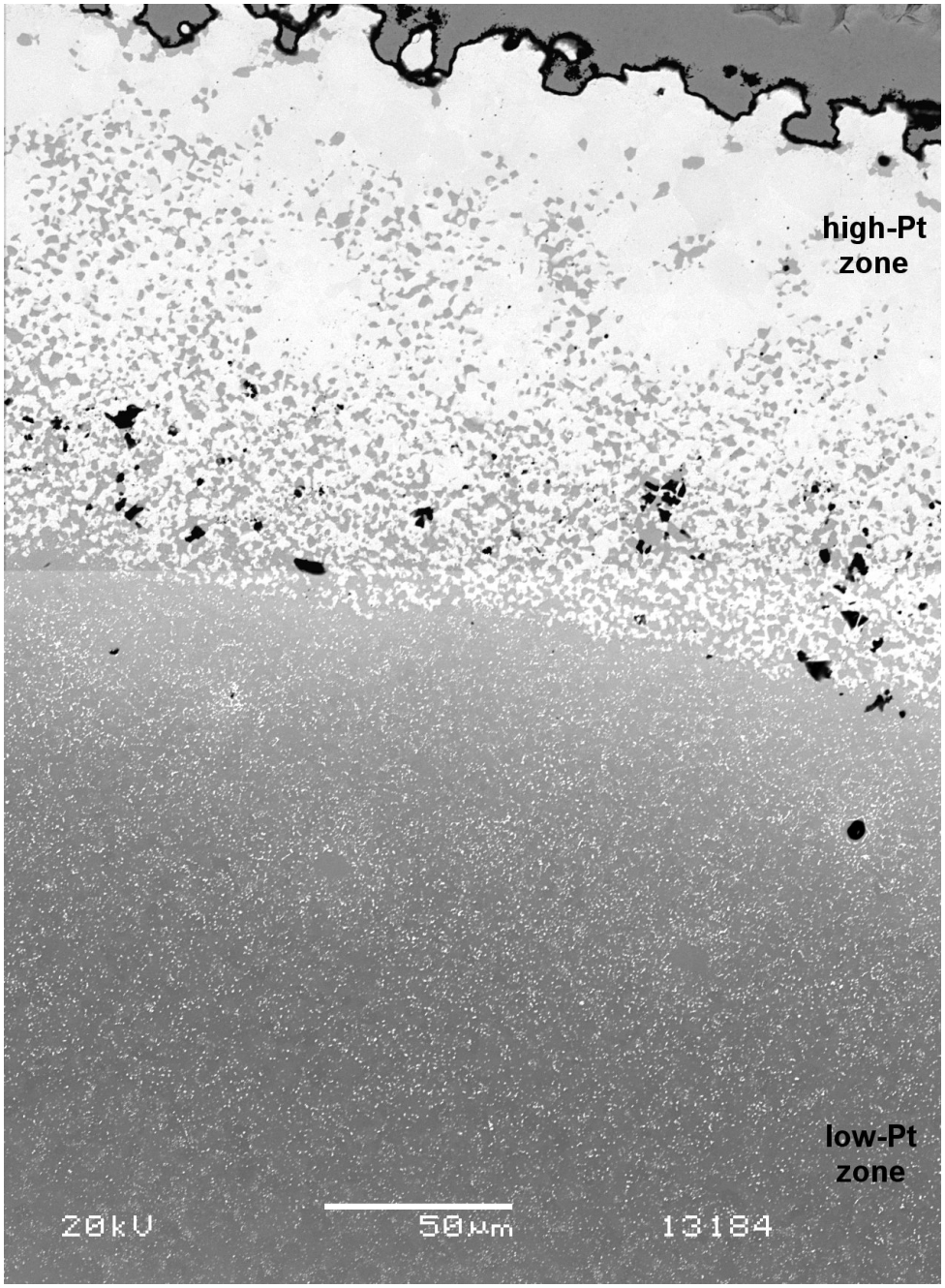

Figure 4.34: BSE micrograph of the high- and low-Pt zone of the bond coat after 5 hours at 1100°C.

The outer high-Pt zone still exhibits a 2 phase structure, with 2 $NiAl$ phases of different platinum contents. At the bond coat/oxide interface a concentration of high-Pt

phase (white) can be seen; the grain size is on average 15μm for the high-Pt phase and 4μm for the low-Pt phase. At the interphase between high- and low-Pt zone, the grains of both phases are much finer, with an average of 2μm diameter.

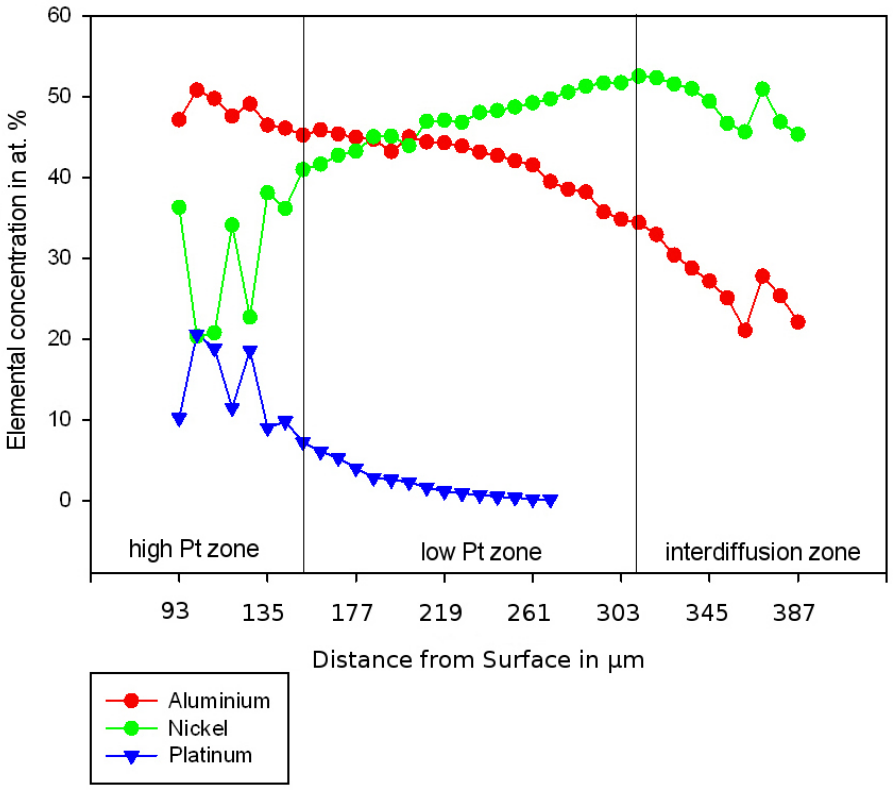

Figure 4.35: Line scan giving the amounts of Al, Ni and Pt from the coating surface to the superalloy, after 5 hours at 1100C.

EDX analysis of the specimens (see figure 4.35) show a similar elementals distribution as after 1 hour at 1100°C. At the bond coat/oxide interface the high-Pt phase (white) has an average Pt content of 19 at.%, the low-Pt phase (grey) has an average Pt content of 10 at.%. The bulk platinum content decreases from the interface between the high- and low-Pt zone towards the interdiffusion zone.

Again, the aluminium content shows a decrease similar to platinum, whereas the nickel content increases from the oxide/bond coat interface towards the super alloy.

10 hours at 1100°C

After oxidation for 10 hours at 1100°C the morphology of the bond coat starts changing significantly (see figure 4.36). Although still clearly divided into two distinct zones with

different platinum levels, the high-Pt zone is now only 75μm thick, whereas the low-Pt zone has gained volume to an average thickness of 270μm. While still consisting of two phases with different platinum content, the amount of low-Pt phase within this outer zone of the coating has decreased significantly. The fine precipitation, formerly only present in the low-Pt zone, can now also be seen in the high-Pt zone. The grains are between 11μm (high-Pt phase) and 5μm (low-Pt phase) in diameter.

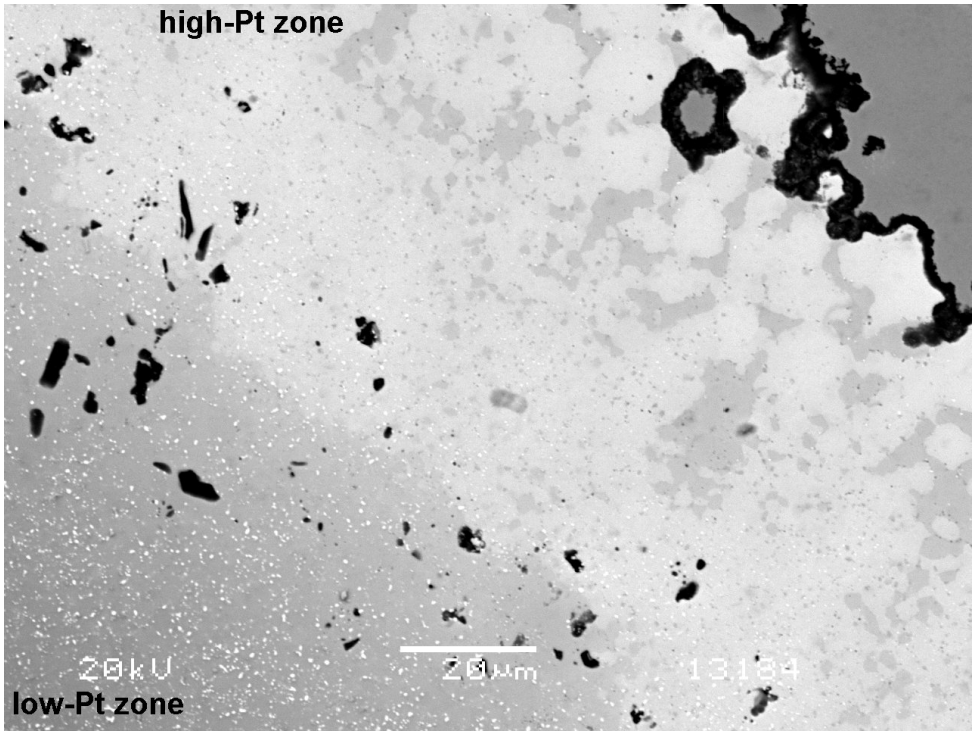

Figure 4.36: BSE micrograph of the high- and low-Pt zone of the bond coat after 10 hours at 1100°C.

Figure 4.37 shows the element distribution of the high-Pt zone, with an average platinum content in the high-Pt phases of 19 at.% and of 14 at.%. The average aluminium content lies at 47 at.%, of nickel at 26 at.%.

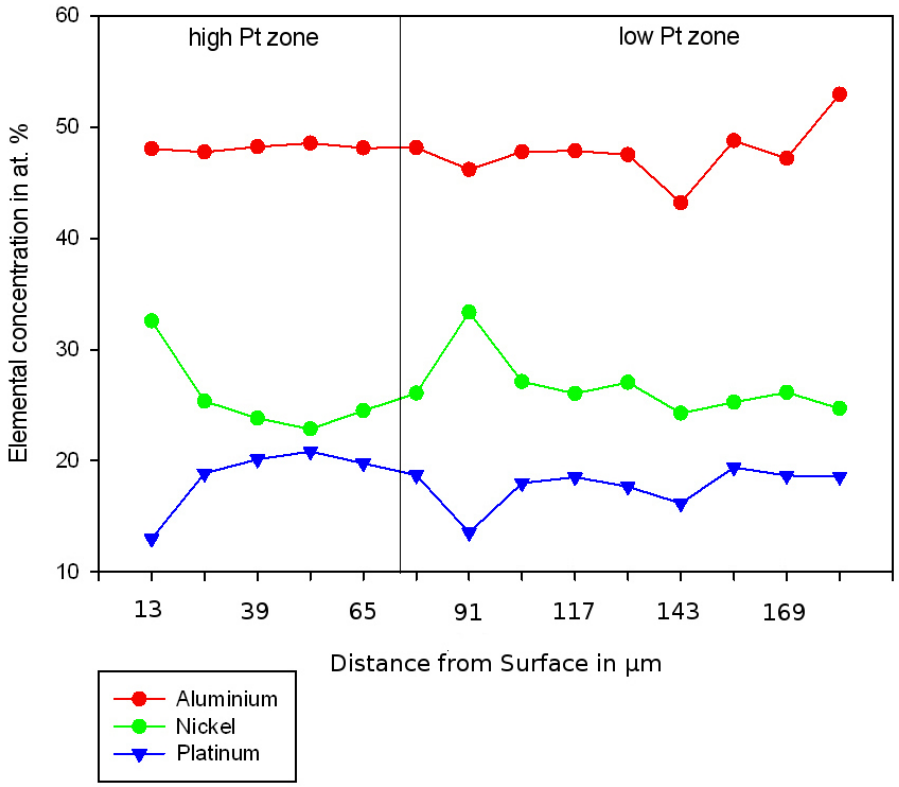

Figure 4.37: Line scan giving the amounts of Al, Ni and Pt of the high-Pt zone, after 10 hours at 1100C.

4.4.2 15 hours at 1100°C

After oxidation for 15 hours at 1100°C the two-phase structure of the outer, high-Pt zone is gone. There is still a difference in contrast, as seen in the BSE micrograph in figure 4.38, between the outer and inner zone, suggesting a difference in chemical composition. Though the difference is not as sharp as it was in the experiments with shorter times at temperature. The outer zone now has an average thickness of 64 μm.

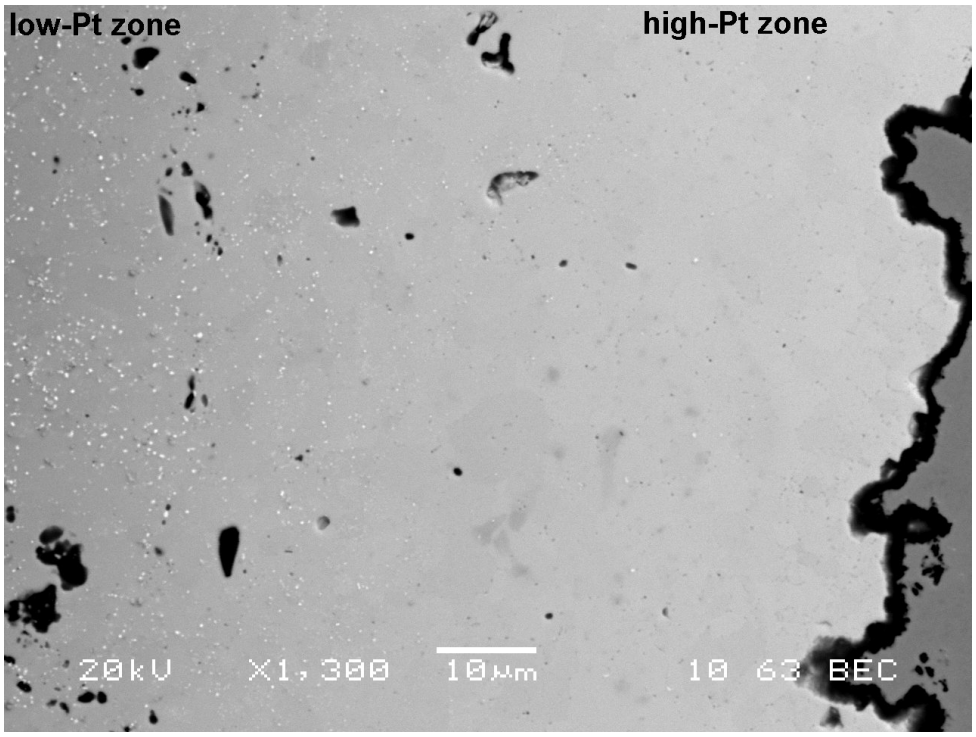

Figure 4.38: BSE micrograph of the high- and low-Pt zone of the bond coat after 15 hours at 1100°C.

The EDX analysis (fig. 4.39) show a gradual decrease in platinum content from the outer surface, where it is around 20 at%, towards the interdiffusion zone, where it is at 6 at%. The Nickel content shows an inverse distribution, increasing from an average of 29 at% at the outer surface to to 43 at% at the interdiffusion zone. The aluminium content only exhibits a very slight decrease, from 45 to 42 at%.

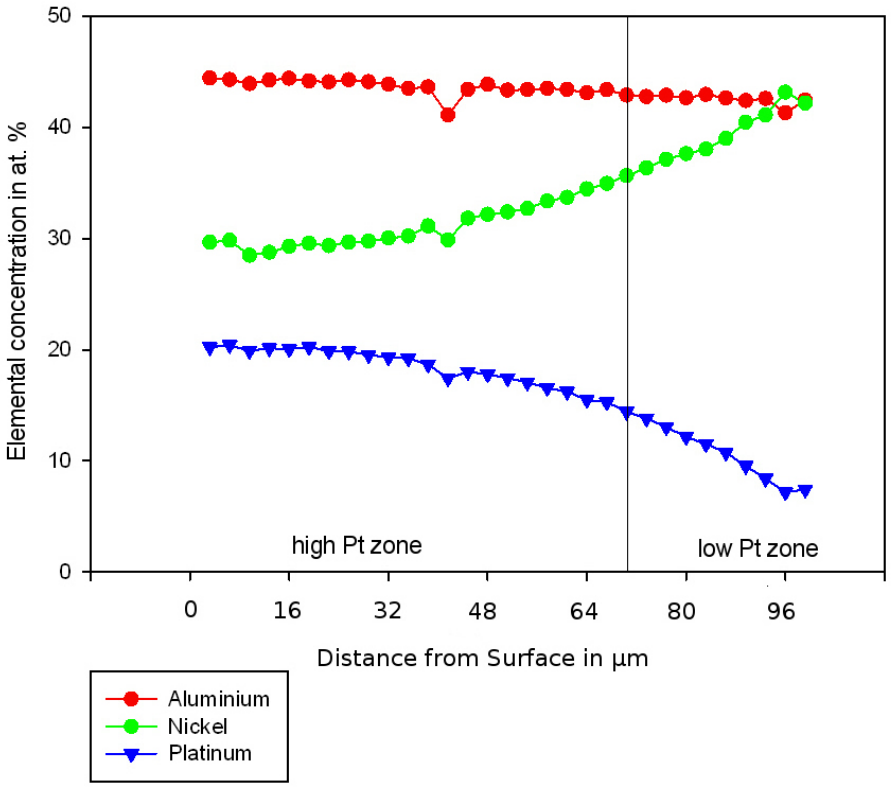

Figure 4.39: Line scan giving the amounts of Al, Ni and Pt from the coating surface to the superalloy, after 15 hours at 1100C.

4.4.3 20 hours at 1100°C

The morphology of the bond coat does not change considerably after oxidation for 20 hours at 1100°C. In BSE images (fig. 4.40) there is still a slight difference in contrast between the outer and inner zone of the coating, this change is gradual however and distinct borders are hard to define.

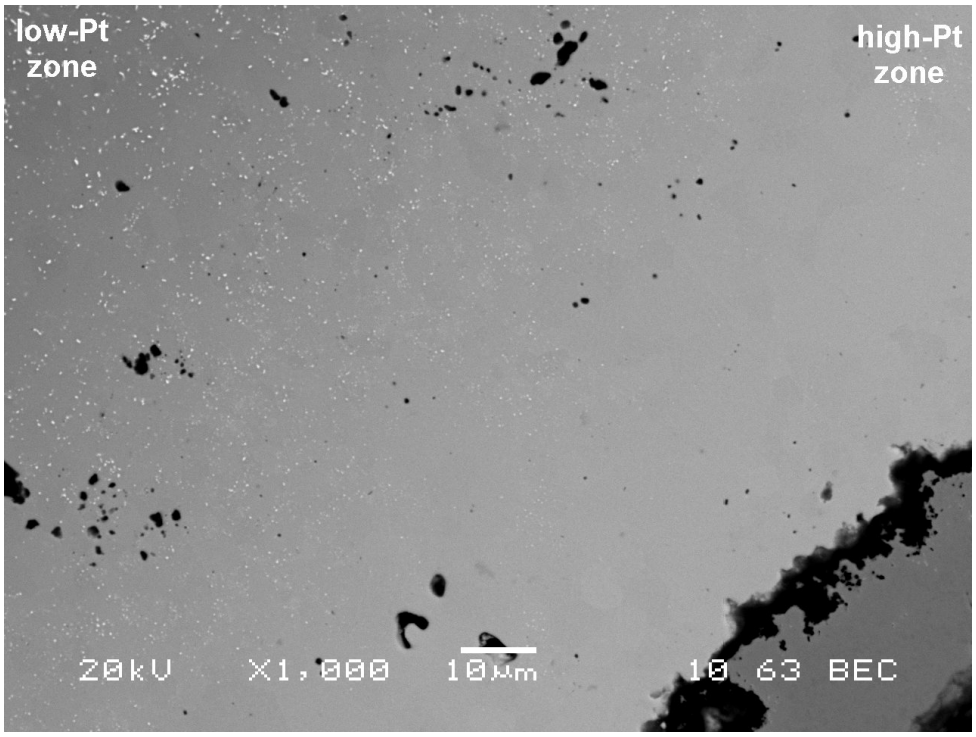

Figure 4.40: BSE micrograph of the high- and low-Pt zone of the bond coat after 20 hours at 1100°C.

Similar to the 15-hours experiment, the main difference between the zones is in platinum and nickel content. EDX analysis shows a decrease in platinum from 16 to 6 at% from the outer surface, to the interdiffusion zone. The nickle content increases from 38 to 48 at% over the same distance. The aluminium content again only decreases very slightly, from 40 to 38 at%.

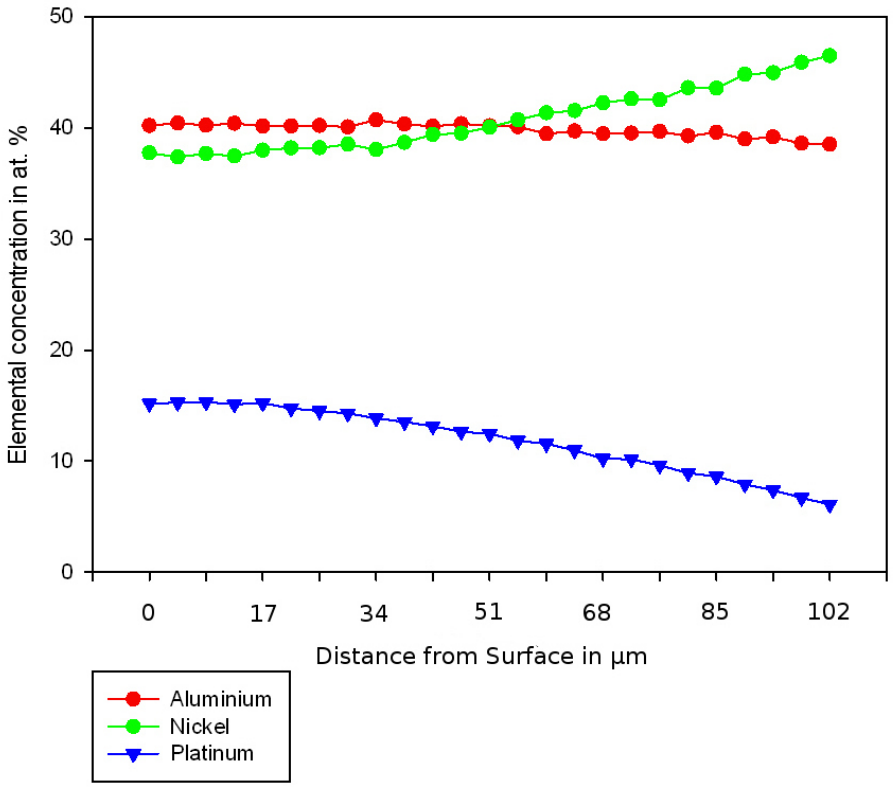

Figure 4.41: Line scan giving the amounts of Al, Ni and Pt from the coating surface to the superalloy, after 20 hours at 1100C.

4.4.4 25 hours at 1100°C

The bond coat morphology does not change significantly from 20 to 25 hours of oxidation. As with the 20 hour experiment there is a gradual change in contrast from the high Pt to the low Pt zone (see fig. 4.40).

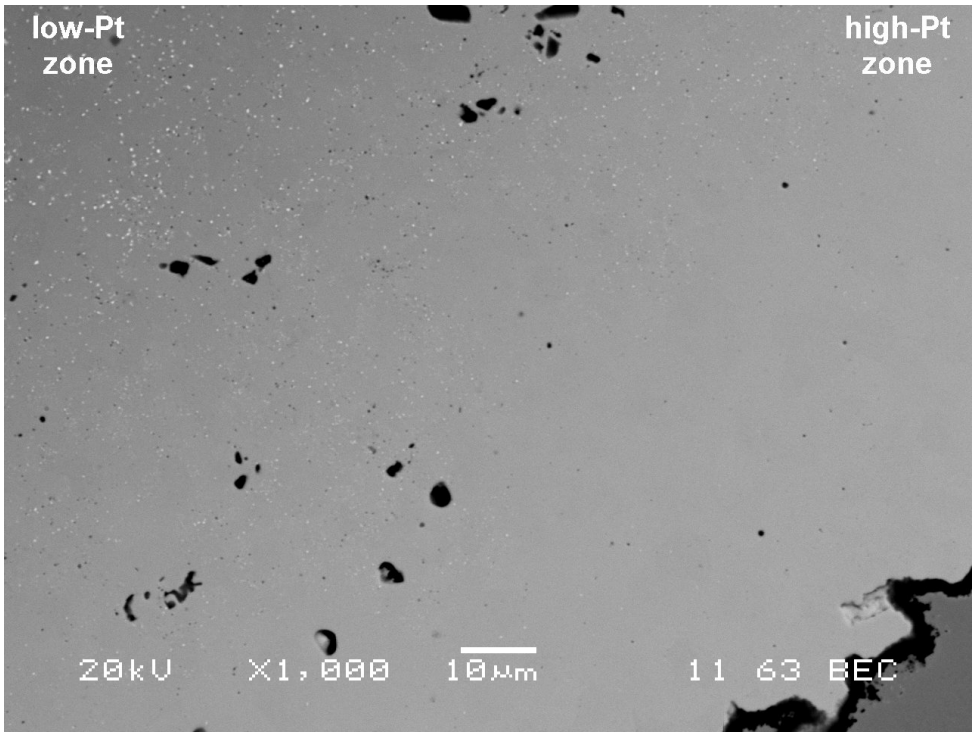

Figure 4.42: BSE micrograph of the high- and low-Pt zone of the bond coat after 25 hours at 1100°C.

The analysis show that platinum gradually decreases from the outer surface of the coating towards the low platinum zone, from about 16 to 6 at %. The aluminium levels also decrease slightly, from 40 to about 38 at %. Correspondingly the amount of nickel increases quite prominently from the outer surface towards the interdiffusion zone, from 38 to 48 at. %.

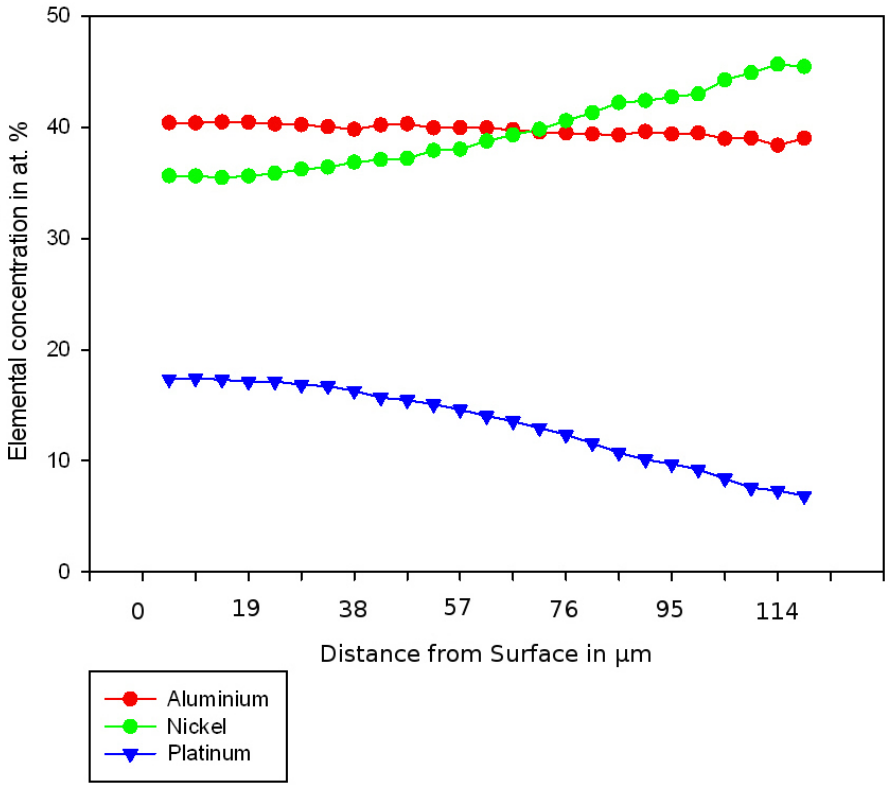

Figure 4.43: Line scan giving the amounts of Al, Ni and Pt from the coating surface to the superalloy, after 25 hours at 1100C.

4.4.5 50 hours at 1100°C

The bond coat thickness after 50 hours at 1100°C is 550μm, from the outer surface to the interdiffusion zone (see figure 4.44). There is no longer a difference in contrast between the outer and inner zone of the coating. The EDX analysis (fig. 4.45) shows that the elements are evenly distributed throughout the whole thickness of the coating. The average contents are 35 at% for aluminium, 55 at% for nickel and 4 at% for platinum.

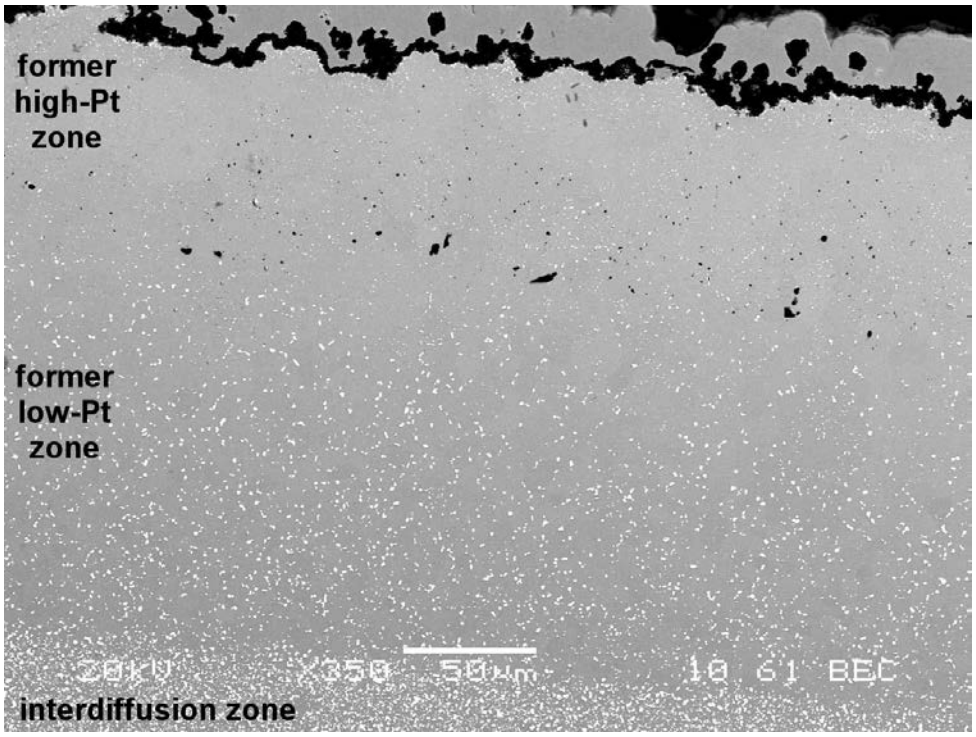

Figure 4.44: BSE micrograph of the high- and low-Pt zone of the bond coat after 50 hours at 1100°C.

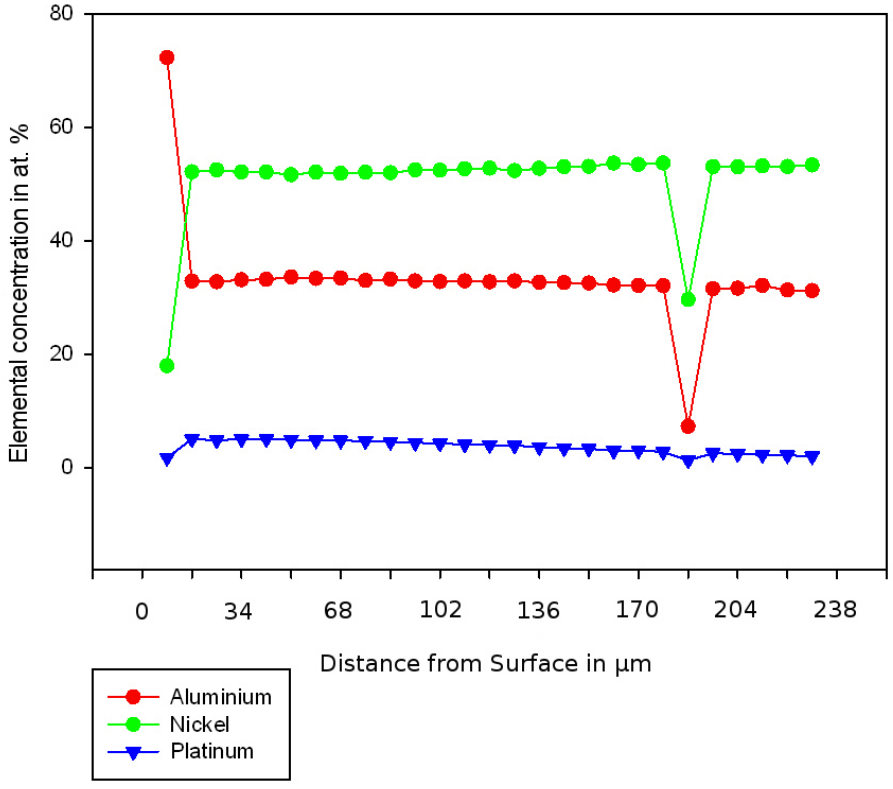

Figure 4.45: Line scan giving the amounts of Al, Ni and Pt from the coating surface to the superalloy, after 50 hours at 1100C.

4.4.6 75 hours at 1100°C

After 75 hours at 1100°C, the bond coat thickness, from the outer surface to the interdiffusion zone is 240μm. The BSE images now show distinct grains within the former low-Pt zone (see fig. 4.46). These grains range in thickness from 12 to 6μm.

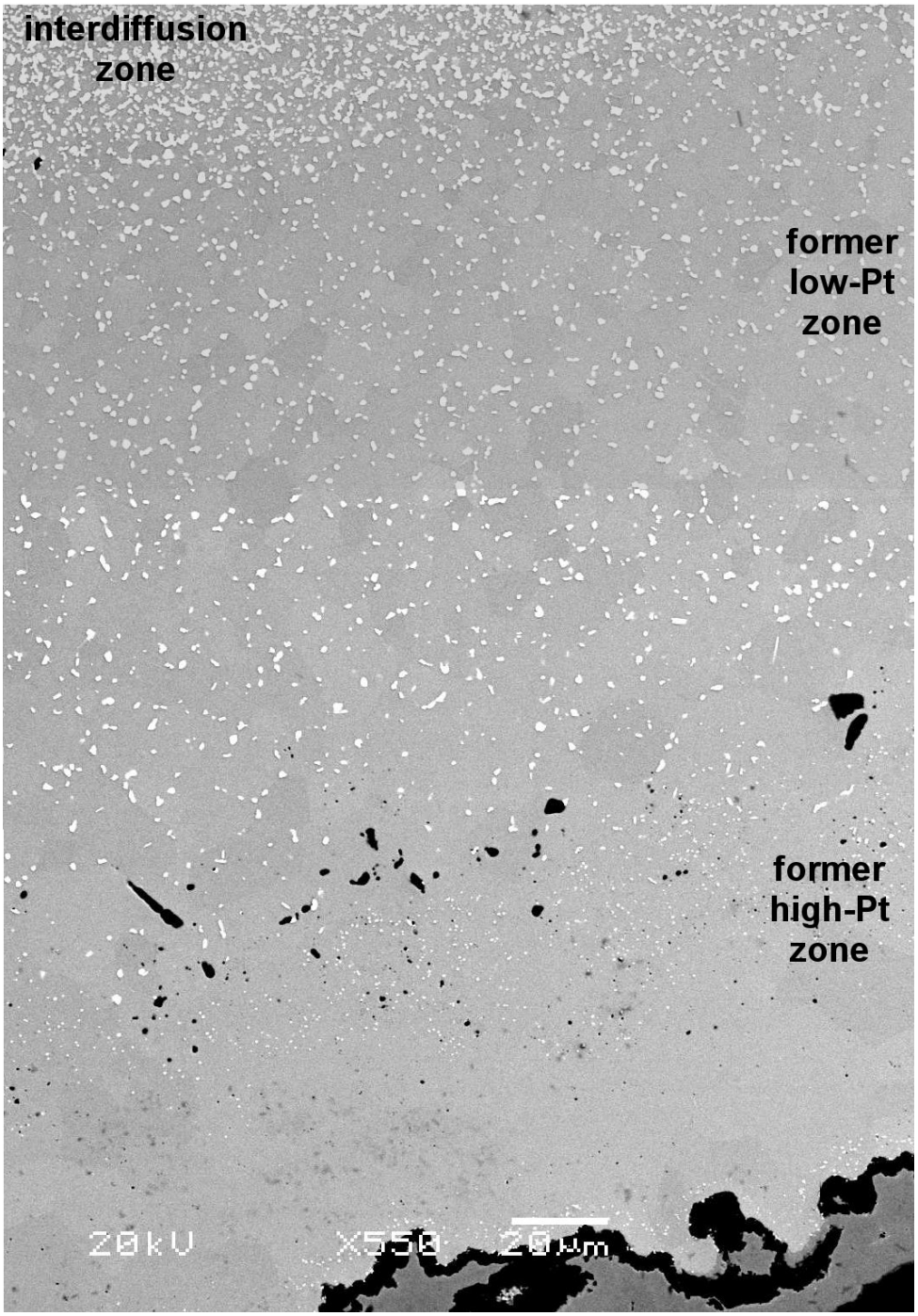

Figure 4.46: BSE micrograph of the high- and low-Pt zone of the bond coat after 75 hours at 1100°C.

EDX analysis shows an average aluminium content of 32 at%, an average nickel content

of 51 at% and an average platinum content of 5 at%. Again, like in the 50 hour experiment, there is no gradient, but an even distribution of elements throughout the whole of the bond coat.

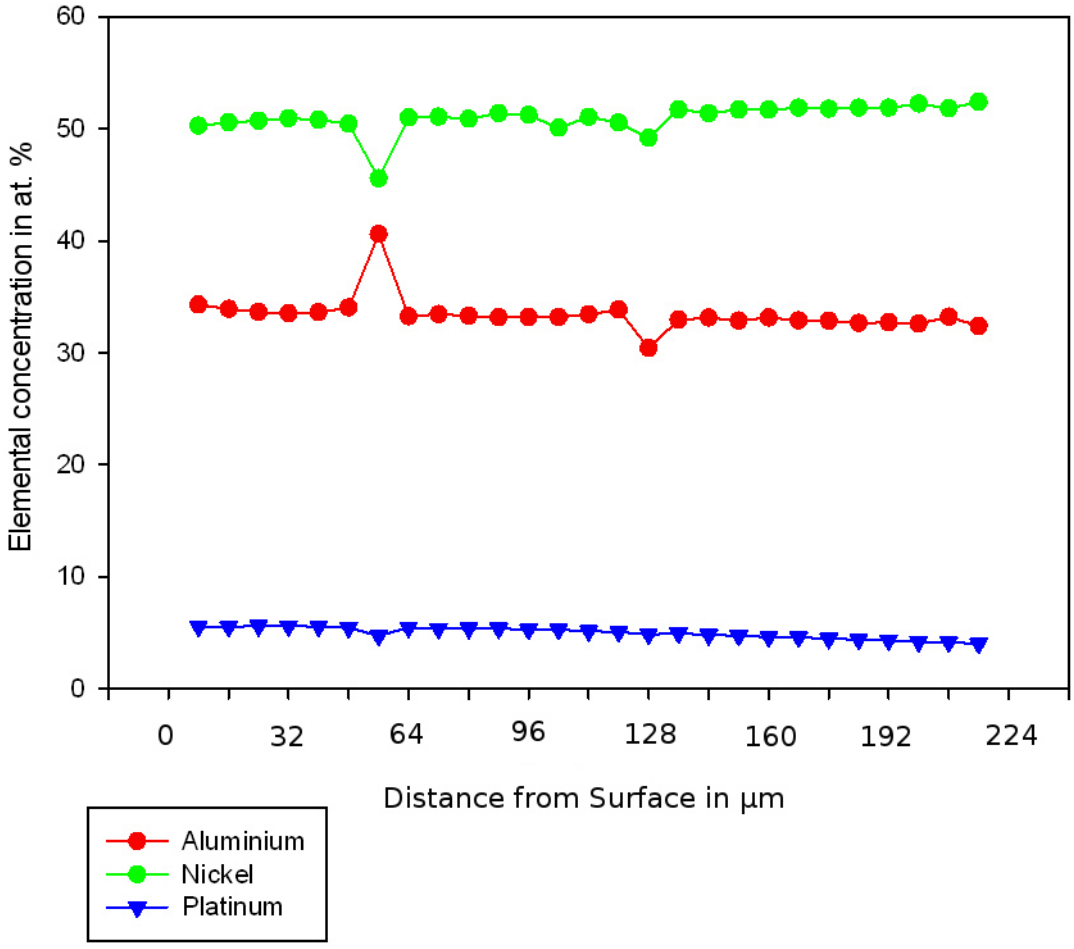

Figure 4.47: Line scan giving the amounts of Al, Ni and Pt from the coating surface to the superalloy, after 75 hours at 1100C.

4.4.7 100 hours at 1100°C

After 100 hours at 1100°C the bond coat is 240μm thick from the outer surface to the interdiffusion zone, 430μm from the surface of the coating to the interface with the superalloy.

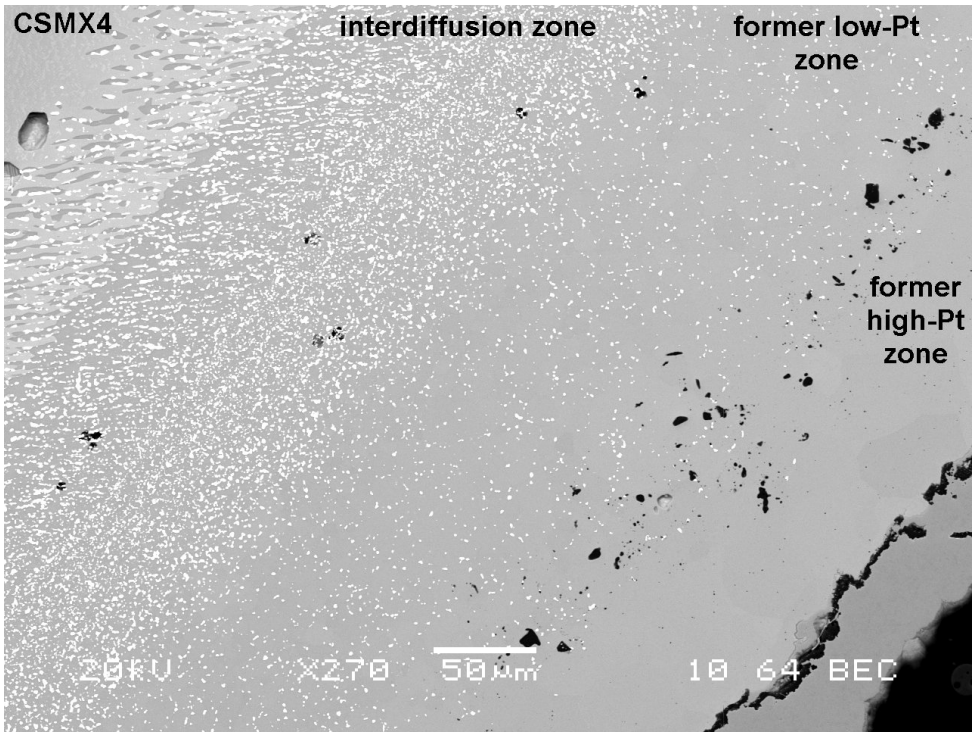

Figure 4.48: BSE micrograph of the high- and low-Pt zone of the bond coat after 100 hours at 1100°C.

The average aluminium content has gone down to 32 at%, the average nickel content is 51 at% and the average platinum content is 4 at%. The elements are evenly distrubuted throughout the coating, there is no noticable gradient between the outer surface of the coating and bond coat/superalloy interface.

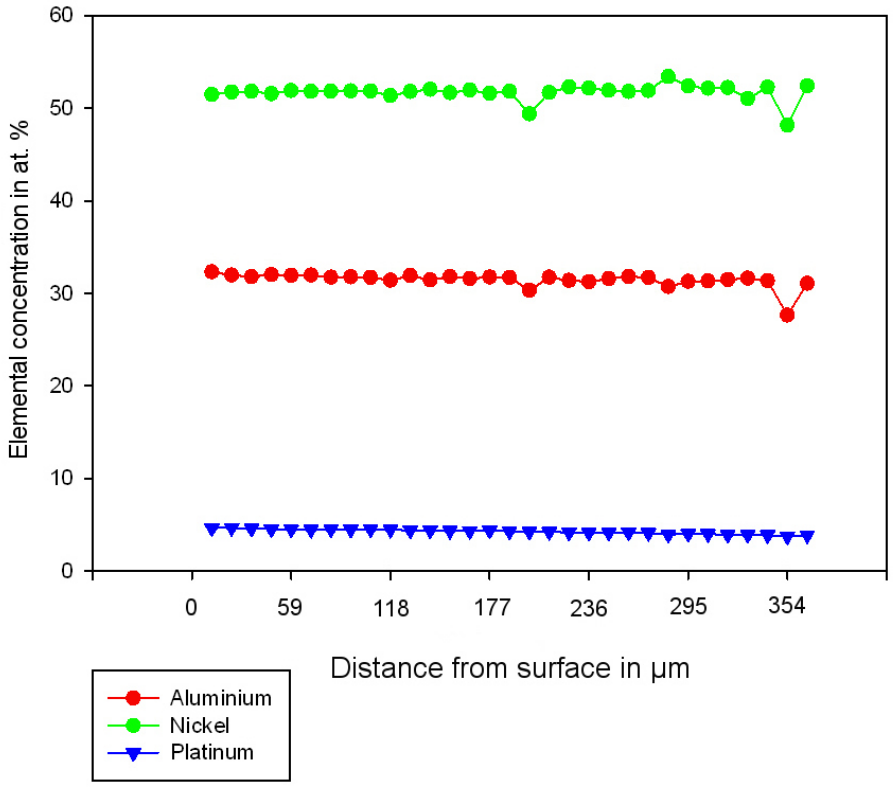

Figure 4.49: Line scan giving the amounts of Al, Ni and Pt from the surface to the superalloy, after 100 hours at 1100C.

4.5 TEM results

4.5.1 Low Pt specimens

Due to the relatively large grain size in the low Pt specimen and the TEM sample preparation being done by FIB sectioning, it was possible to choose phase boundaries between $NiAl$ and Ni_3Al and section through them, to look at the phases and the oxide grown on top of them in their original context. The samples chosen for this method had been oxidised for 7 minutes at 1100°C, as their slightly thicker oxide layer was easier to retain during the ion milling process.

As can be seen in the montages (figures 4.50 and 4.51) the phase boundaries within the bond coat, indicated by a red line, also mark a difference in oxide morphology within the oxide layer. The hole that can be seen in figure 4.50 where the phase boundary should

be is an artifact created by ion milling. The voids at the oxide/metal interface were there from the start, but have been enlarged during the final thinning process. The same applies to the voids at the oxide/metal interface in figure 4.51.

Just below the oxide layer is a thin aluminium depleted zone, clearly visible throughout the whole sample in figure 4.50, not quite as clear in figure 4.51.

Both figure 4.50 and 4.51 show the microstructure of martensite transformation within the $NiAl$ grain.

The oxide layer grown on top of the martensitic $NiAl$ consists of columnar grains (fig. 4.50 and 4.51), the oxide layer grown on top of Ni_3Al is more complex, showing a 2 layered structure, with a series of voids as the dividing line in one case (figure 4.50) and a zone rich in Cr, Ti and Ta in the other (figure 4.51).

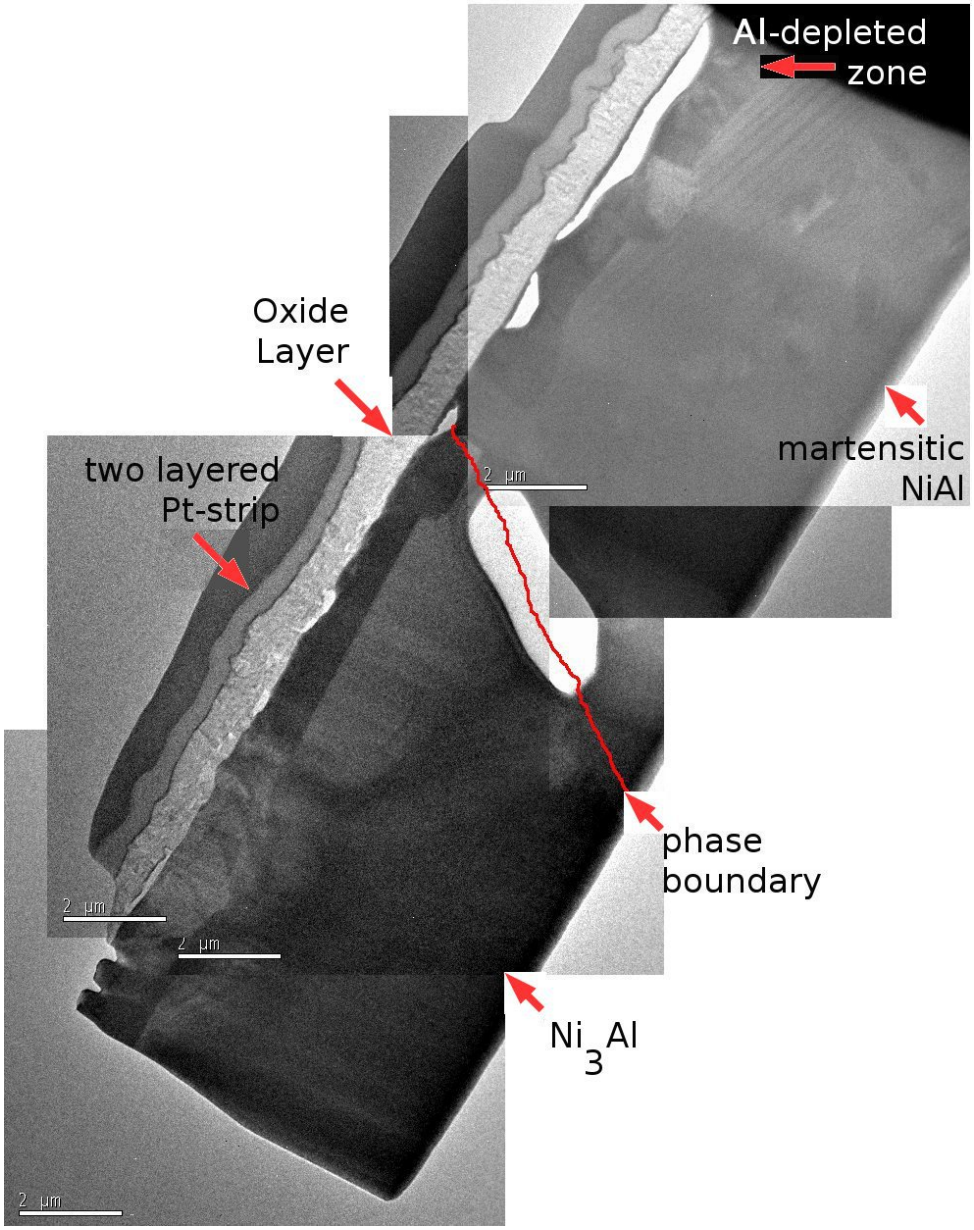

Figure 4.50: Montage of bright field images showing the whole TEM specimen of a low Pt sample after 7 minutes at 1100°C. The top two layers are the protective platinum strip (the darker outer layer deposited by ion beam, the lighter inner layer deposited by electron beam), followed by the oxide layer, then the aluminium depleted zone, the bulk of the sample consists of the two bond coat phases, martensitic $NiAl$ on the top right and Ni_3Al on the bottom left. The phase boundary is indicated by a red line.

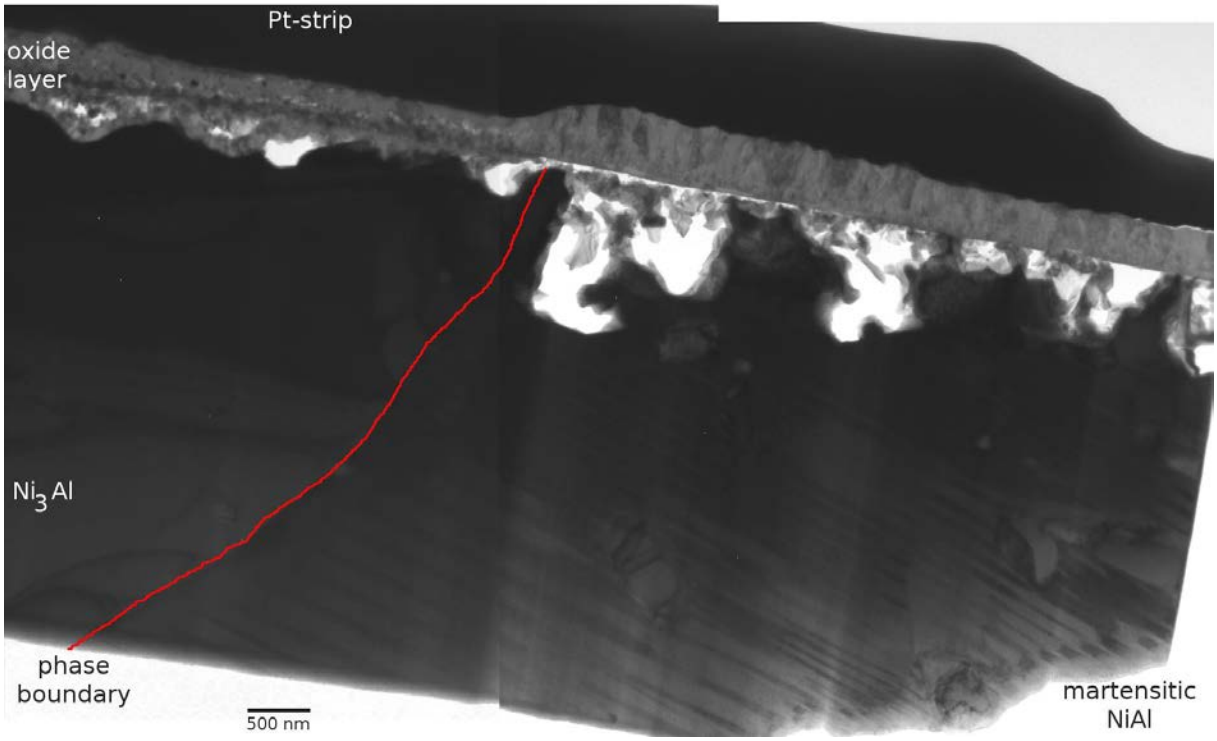

Figure 4.51: Montage of bright field images showing the whole TEM specimen of a low Pt sample after 7 minutes at 1100°C. The black top-most layer is the protective platinum strip, below lies the oxide layer. The aluminium depleted zone below the metal can't be seen in this particular case. The grain boundary is again indicated by a red line , to the right is the martensitic $NiAl$ grain, to the left the Ni_3Al grain.

STEM Line scans

Several line scans were made in order to see the element distribution from the part of the metal that is not effected by the diffusion processes, over the aluminium depleted zone and the oxide. Six elements were picked for this analysis: oxygen, aluminium, platinum, chromium, cobalt and nickel.

The line scans of martensitic NiAl and the oxide grown on top of it shows a quite expected element distribution (see figures 4.52 and 4.53). Between the NiAl and the oxide layer is an aluminium depleted zone, with relatively higher levels in Ni and Co. The Pt levels goes down with the Al, Cr stays at the same level until it reaches a peak just before a very thin zone (marked with an 'x' in figures 4.52 and 4.53) of the specimen, that might relate to a void or may be an artifact from the ion milling process. According to the line scan the oxide consists almost entirely of oxygen and aluminium, apart from a small Ni peak at the former oxide/air interface.

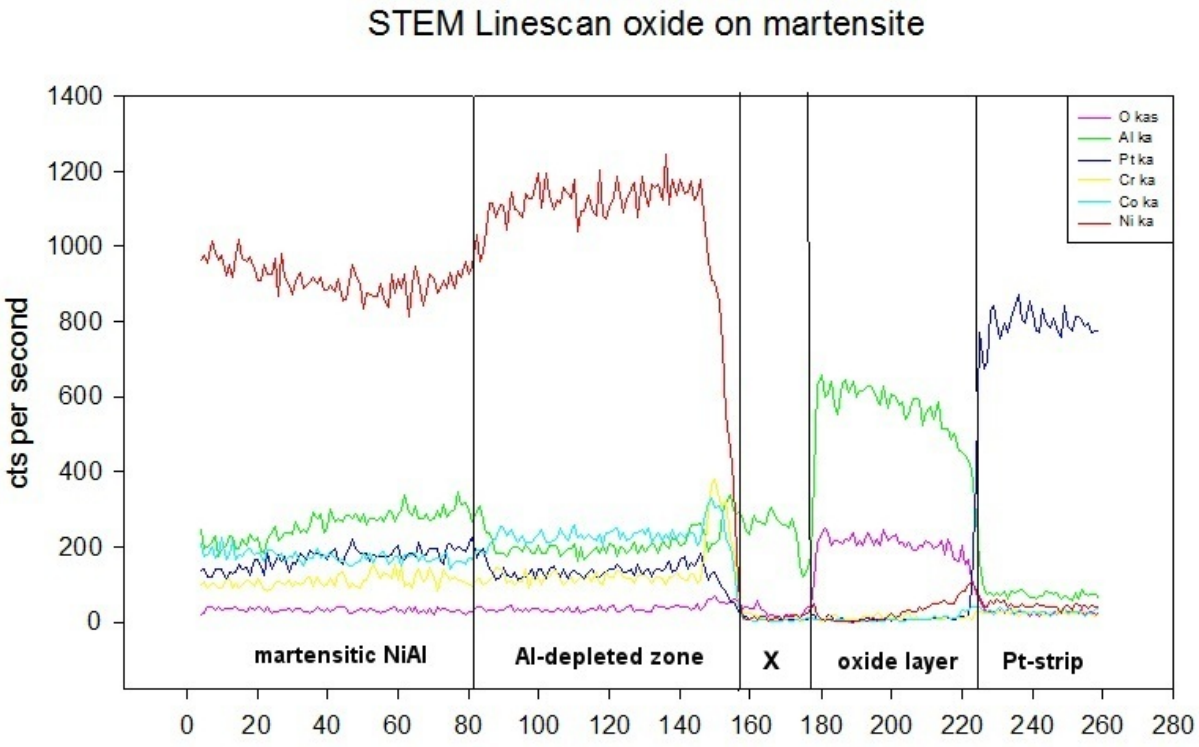

Figure 4.52: STEM Line scan showing the element distribution from metal to oxide. The exact location of the line is indicated in figure 4.53.

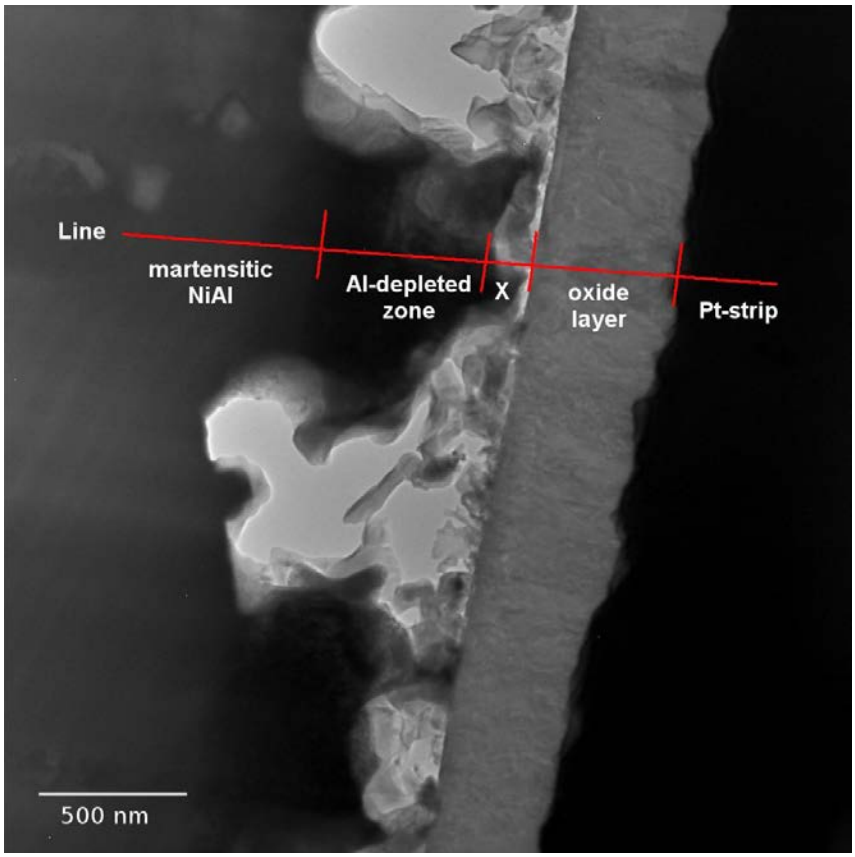

Figure 4.53: TEM image showing the location of the line scan from figure 4.52.

The line scans taken on the Ni_3Al and the oxide grown there-on, show a much more complex oxide layer. The oxide layer is divided into two parts. The dividing line can be seen in the TEM-micrographs as a thin dark layer running parallel to the oxide/metal interface (figures 4.51, 4.54, 4.55). The inner layer, at the oxide metal interface, shows many voids but only a small amount of impurities. One of these can be seen in figure 4.55. The dark particle is nickel- and platinum-rich, as can be seen from the line scan (fig. 4.54), surrounded by aluminium-rich phases. The outer layer, marked as oxide II in the figures, consists mainly of an aluminium oxide, with a nickel and cobalt peak at the outside.

Away from any voids and impurities (figures 4.56 and 4.57) the oxide layer on top of Ni_3Al shows a pure aluminium oxide on the inner layer, a chromium peak corresponding to the thin dark layer in the micrographs (see figure 4.56), and an increase in nickel and cobalt in the outer layer of the oxide.

Due to the limitation of line scans more investigations were made using element-mapping, which will be discussed in more detail in the next section.

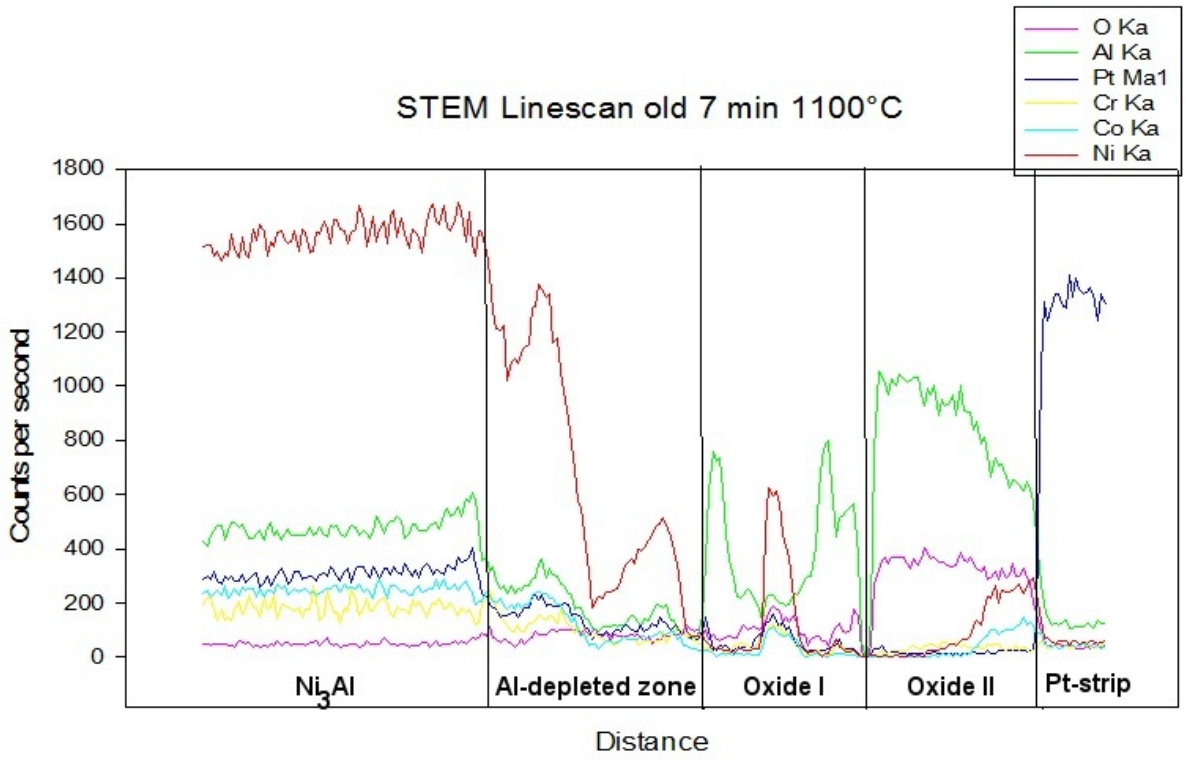

Figure 4.54: STEM Line scan showing the element distribution from metal to oxide. The exact location of the line is indicated in figure 4.55.

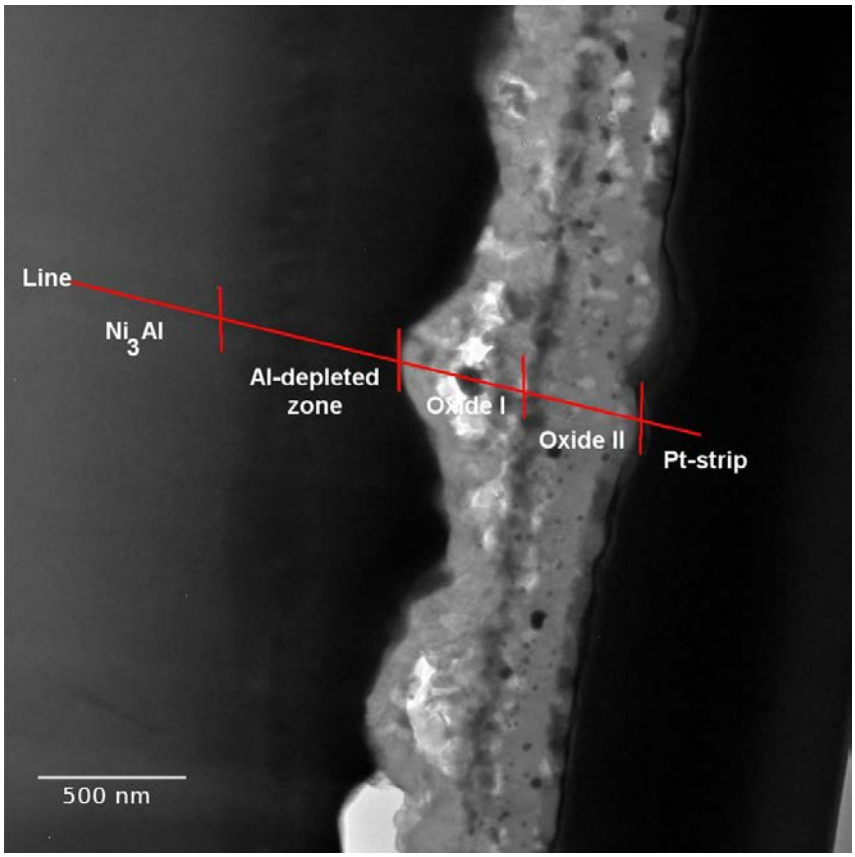

Figure 4.55: TEM image showing the location of the line scan from figure 4.54.

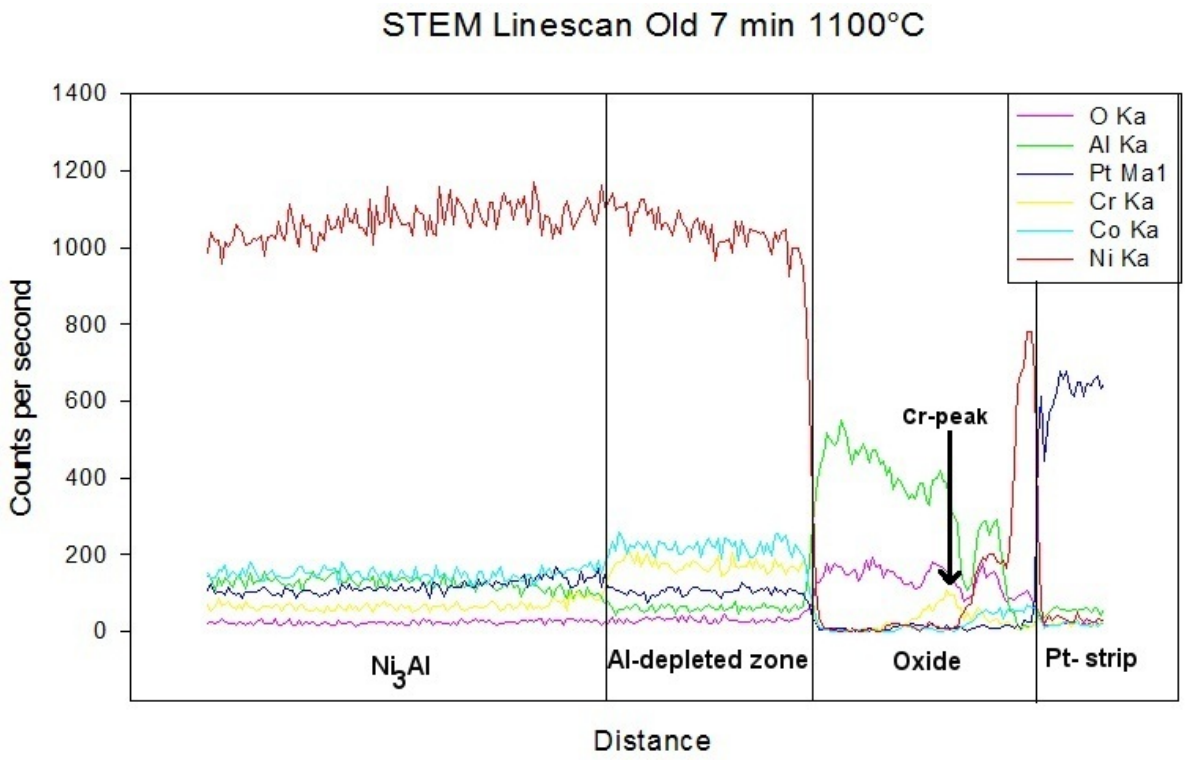

Figure 4.56: STEM Line scan showing the element distribution from metal to oxide. The exact location of the line is indicated in figure 4.57.

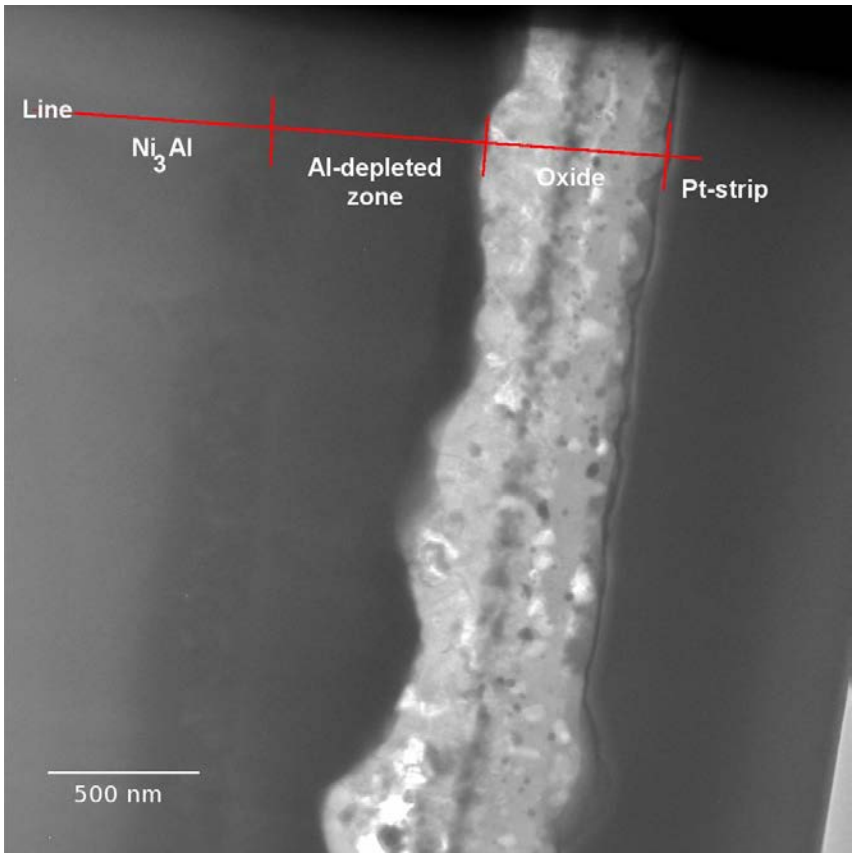

Figure 4.57: TEM image showing the location of the line scan from figure 4.56.

STEM Mapping

To get a clearer picture of the element distribution throughout the oxide layer, larger parts of the oxide were mapped using a drift detector in the TEM. These maps show the scale as a whole, as compared to the more selective line scans.

The quantified maps that can be seen in figures 4.58 to 4.59 are of oxide grown on top of a Ni_3Al grain, where it is relatively complex compared to oxide grown on $NiAl$. These maps confirm that the whole scale is indeed an aluminium oxide (figures 4.58b and 4.58c). There are some platinum rich phases dispersed throughout the outer part on the scale, none of them can be found near the oxide/metal interface (fig. 4.58d).

Some localised nickel-rich phases can be found on this interface (fig. 4.59b), most of the nickel within the oxide scale however, is concentrated on the very outside of the scale, at the oxide/air interface. Cobalt follows the same distribution as nickel (fig. 4.59c). The chromium content is the highest in the center of the scale, decreasing towards the outer part of the oxide, therefore behaving inversely proportional to nickel. There are also some localised Cr-rich phases near the oxide/metal interface.

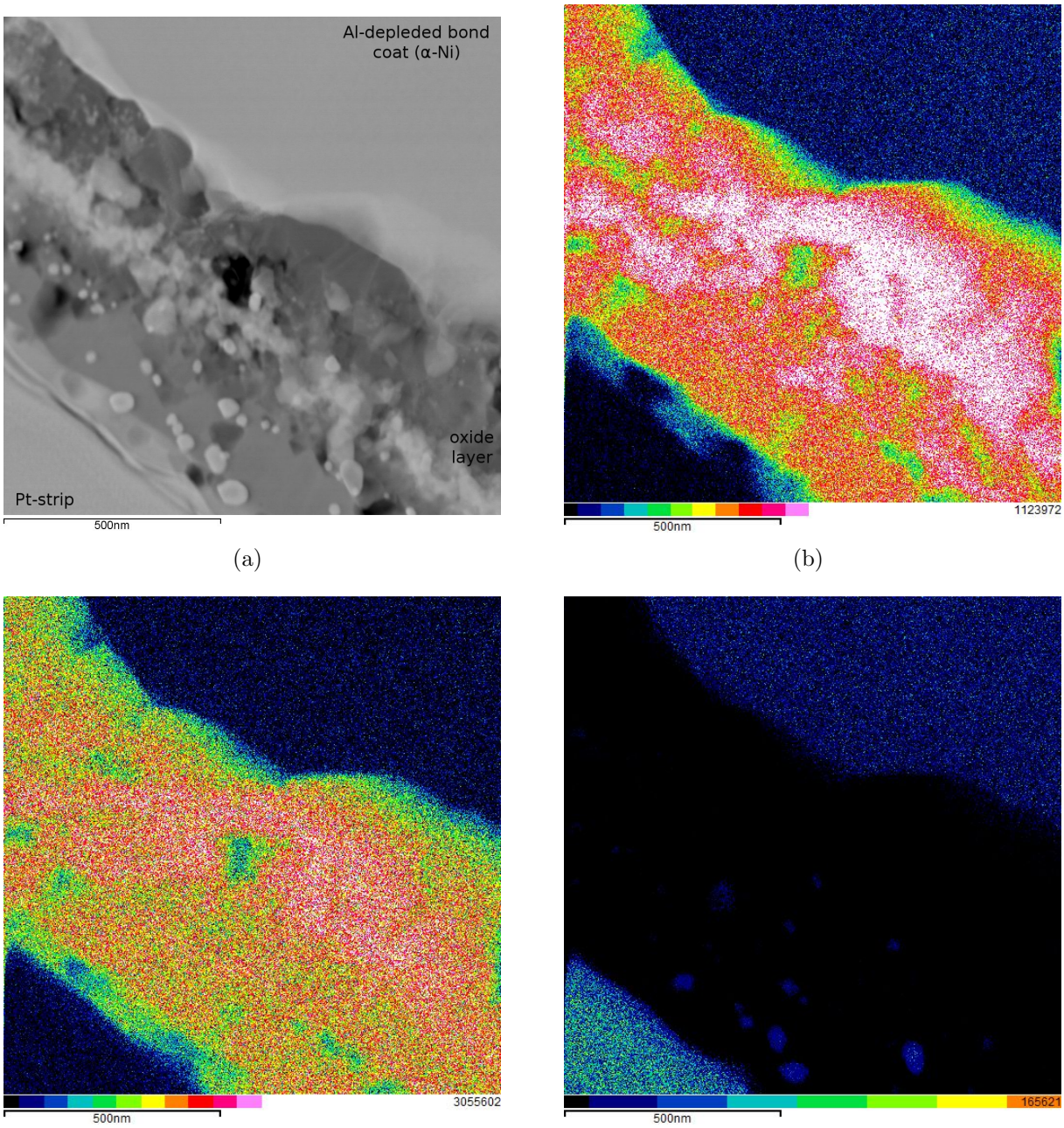

(a) (b)

(c) (d)

Figure 4.58: STEM elemental map of the oxide layer over a Ni_3Al grain part 1. (a) STEM image (b) Aluminium distribution map (c) Oxygen distribution map (d) Platinum distribution map

The central part of the scale is also shows traces of tantalum (fig. 4.60b). Titanium can be found in various places throughout the oxide scale, right at the oxide/air interface, at the central part and in isolated phases in the inner oxide layer (see figure 4.60c).

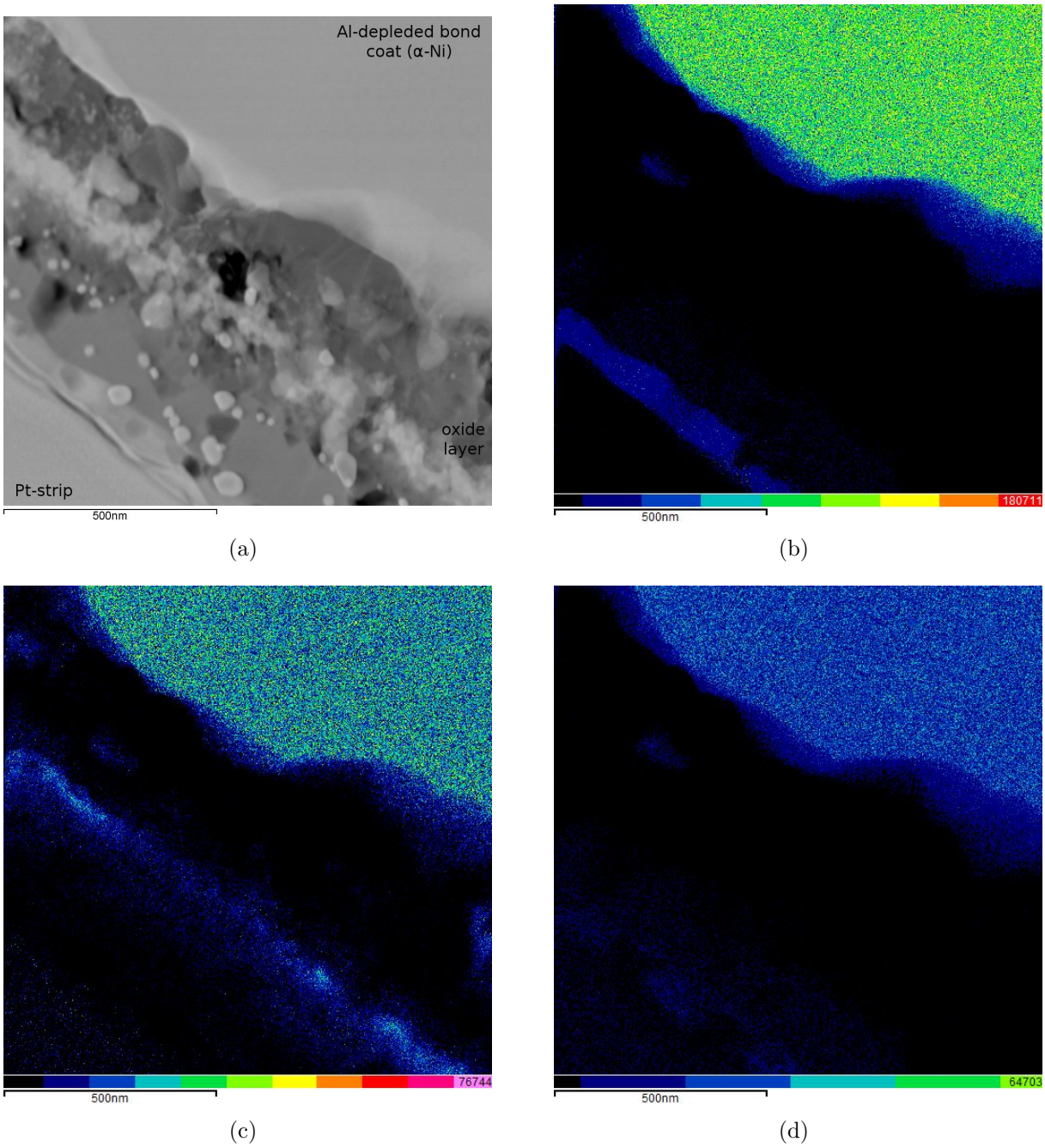

Figure 4.59: STEM elemental map of the oxide layer over a Ni_3Al grain part 2. (a) STEM image (b) Nickel distribution map (c) Chromium distribution map (d) Cobalt distribution map

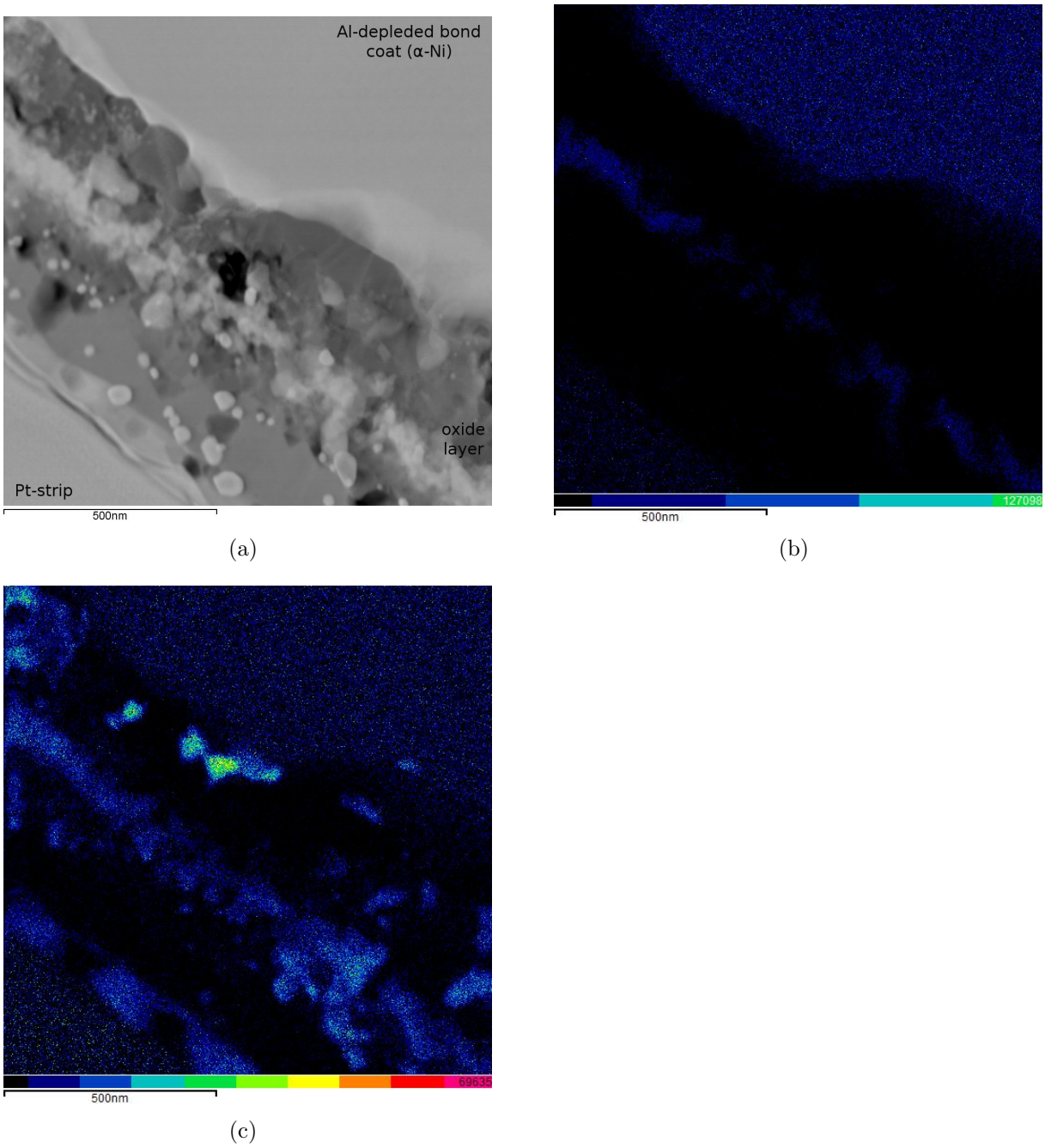

(a) (b)

(c)

Figure 4.60: STEM elemental map of the oxide layer over a Ni_3Al grain part 3. (a) STEM image (b) Tantalum distribution map (c) Titanium distribution map

The oxide scale growing on top of $\beta - NiAl$ however shows a uniform element distribution (fig. 4.61). The scale consists almost entirely of aluminium and oxygen (see figure 4.61), with the exception of nickel as can be seen in figure 4.62a. A small area at the surface of the oxide contains nickel.

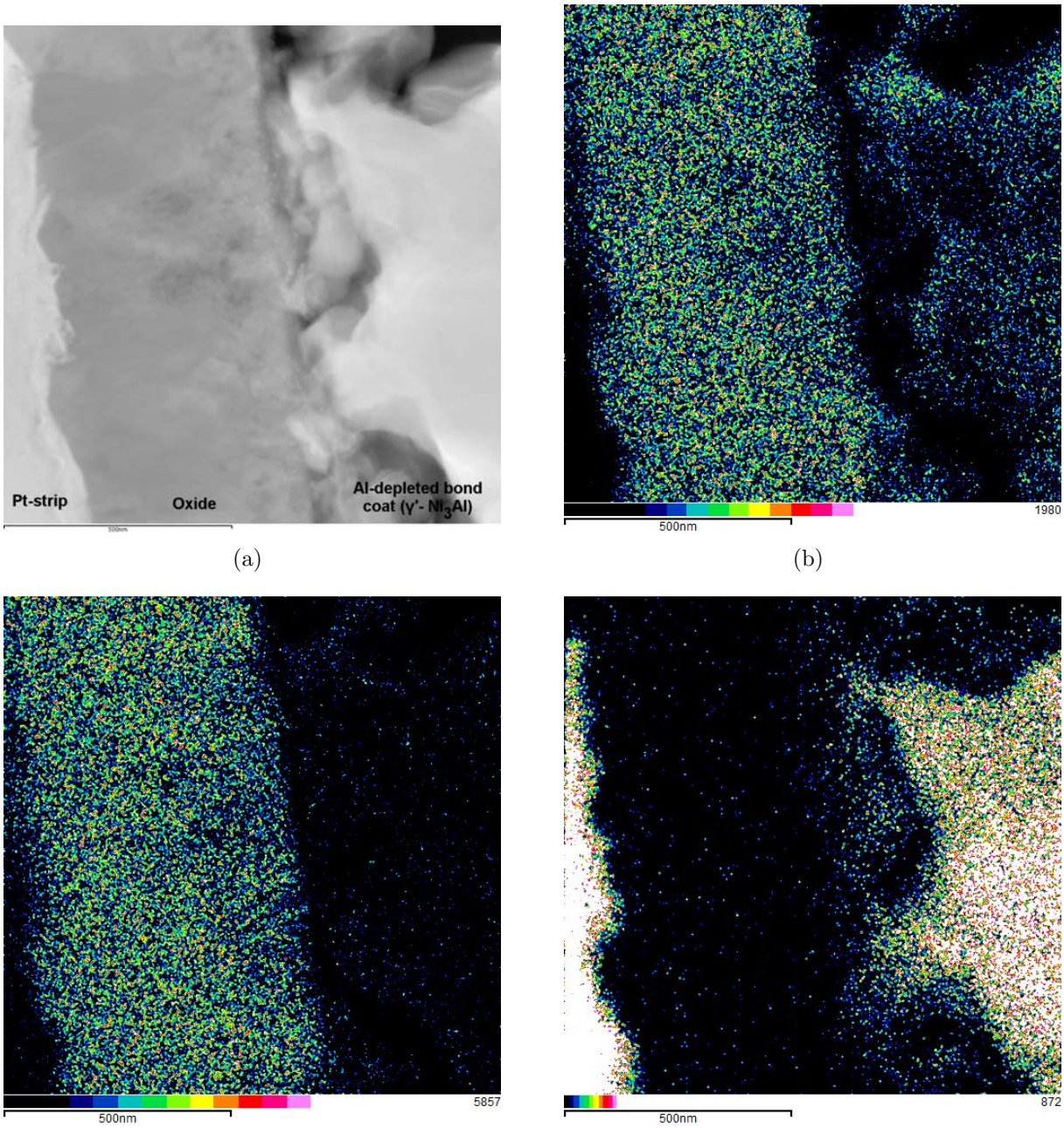

(a) (b)

(c) (d)

Figure 4.61: STEM elemental map of the oxide layer over a $NiAl$ grain part 1. (a) STEM image (b) Aluminium distribution map (c) Oxygen distribution map (d) Platinum distribution map

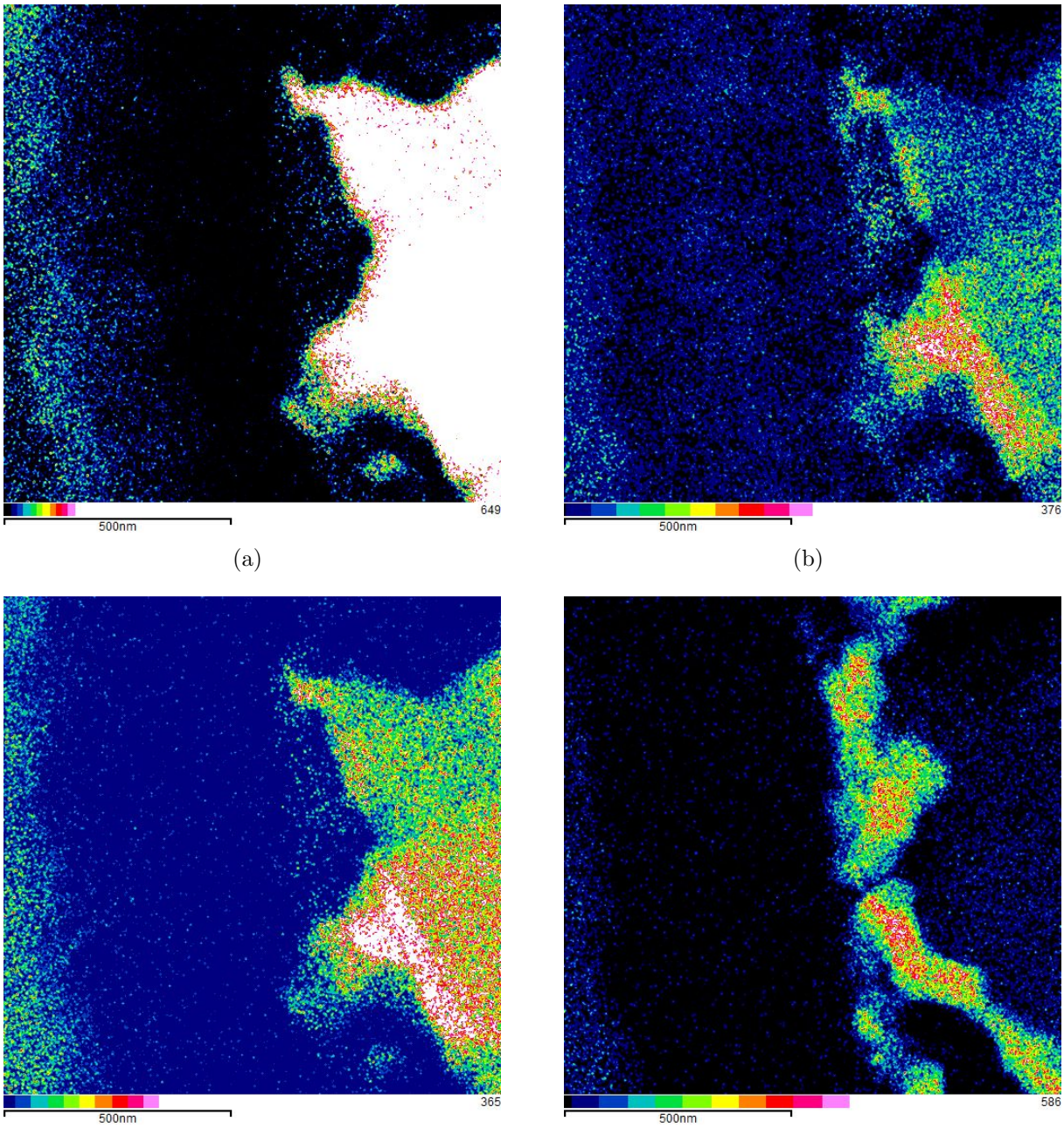

(a) (b)

(c) (d)

Figure 4.62: STEM elemental map of the oxide layer over a $NiAl$ grain part 2. (a) Nickel distribution map (b) Chromium distribution map (c) Cobalt distribution map (d) Titanium distribution map.

Electron diffraction

Electron diffraction was done on oxide grains and on the underlying metal phases. For indexing, powder diffraction data was used as an aid, since none of the phases were truly unknown. The powder diffraction data was taken from the online database ISCD of the FIZ Karlsruhe [10].

Figure 4.63 shows the specimen the diffraction patterns where taken from. It displays the typical morphology, with the two phases Ni_3Al and martensitic $NiAl$, an aluminium depleted zone right at the interface with the oxide and a protective platinum strip, deposited for sample preparation in the FIB.

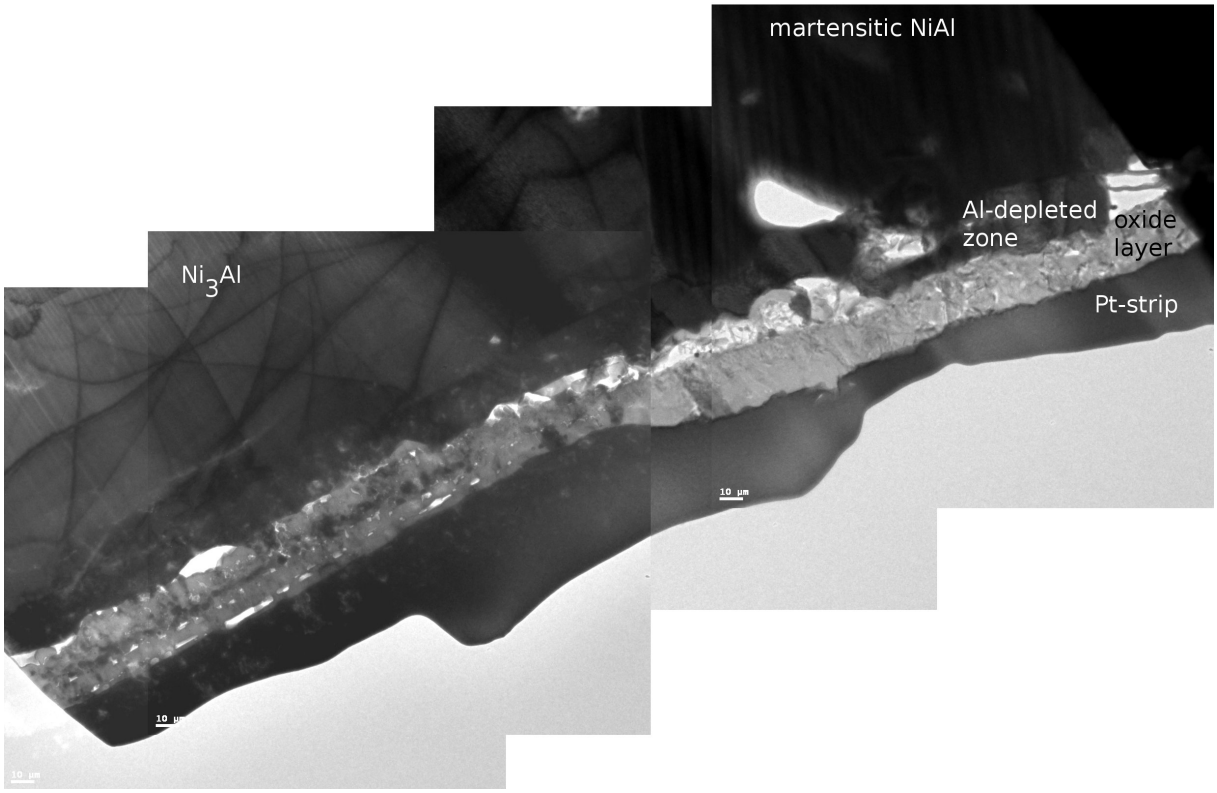

Figure 4.63: Overview of a low-Pt specimen. All diffraction patterns presented below are taken from this specimen.

To confirm the nature of the bond coat phases, diffraction patterns were taken and the d-values compared to published data shown in table 4.4 for Ni_3Al and 4.5 for NiAl.

Figures 4.64 and 4.65 show diffraction patterns taken along 2 different zone axes of Ni_3Al.

H	K	L	2Theta	d-value	Intensity
1	0	0	24.93	3.5720	110.3
1	1	0	35.54	2.5258	85.0
1	1	1	43.90	2.0623	1000.0
2	0	0	51.14	1.7860	449.8
2	1	0	57.71	1.5974	33.4
2	1	1	63.83	1.4583	22.7
2	2	0	75.24	1.2629	221.3
3	0	0	80.70	1.1908	2.3

Table 4.4: Powder pattern table for Ni_3Al, taken from the ICSD Karlsruhe [10].

H	K	L	2Theta	d-value	Intensity
1	0	0	31.03	2.8820	252.4
1	1	0	44.45	2.0379	1000.0
1	1	1	55.20	1.6639	53.2
2	0	0	64.68	1.4410	135.2
2	1	0	73.47	1.2889	53.2
2	1	1	81.87	1.1766	233.8

Table 4.5: Powder pattern table for NiAl, taken from the ICSD Karlsruhe [10].

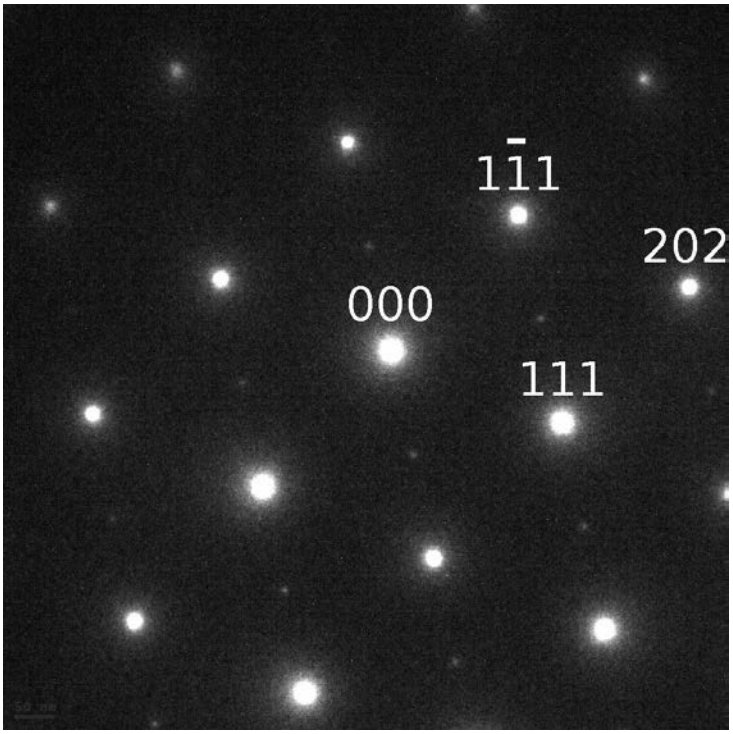

Figure 4.64: $\left[10\bar{1}\right]$ diffraction pattern of Ni_3Al.

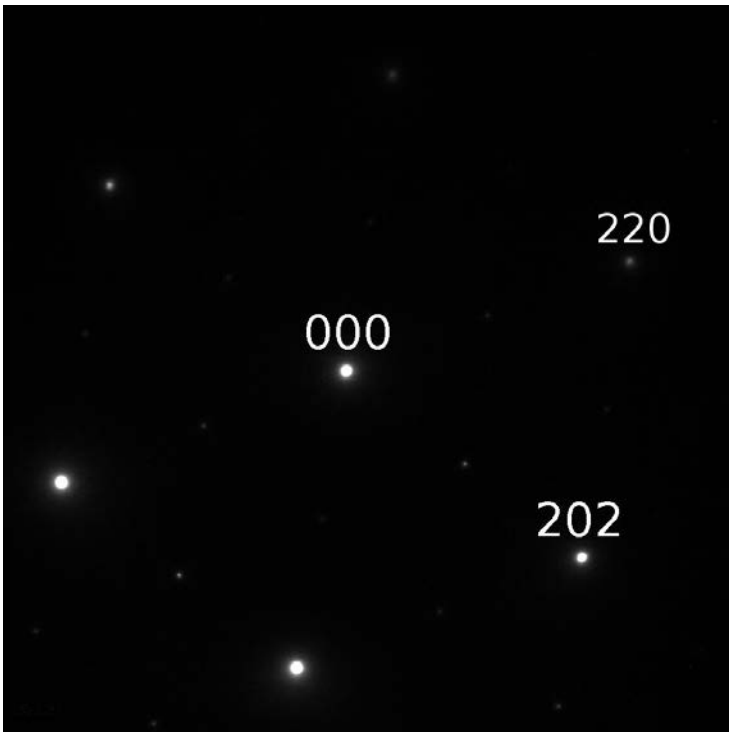

Figure 4.65: $\left[1\overline{1}\overline{1}\right]$ diffraction pattern of Ni_3Al.

The diffraction pattern of the martensitic NiAl shows a doubling of peaks (see figure 4.66), due to the lamellas being very thin, it was impossible to get a diffraction pattern from just one lamella.

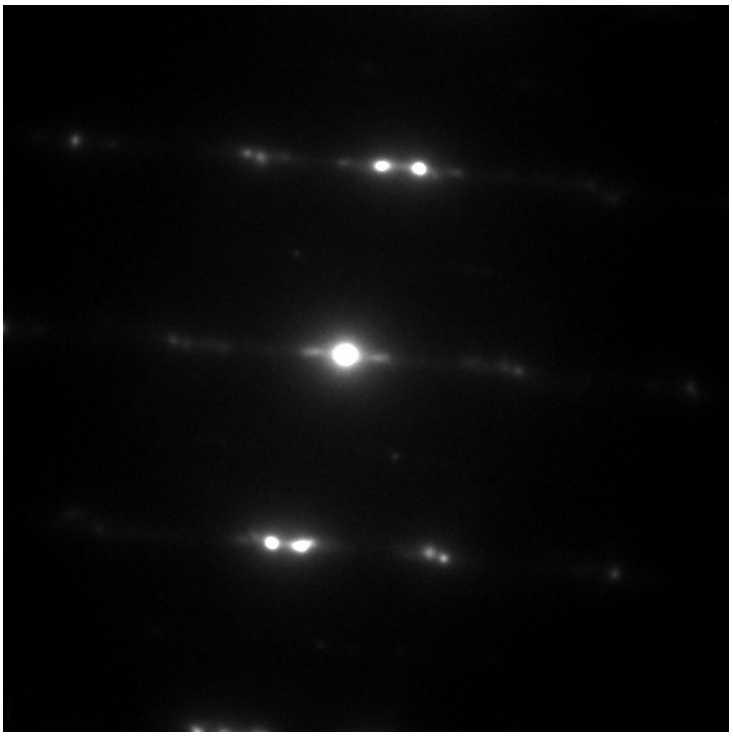

Figure 4.66: Diffraction pattern obtained from the martensitic NiAl, showing double peaks due to the size of the lamellas.

Figure 4.67 shows the oxide formed over NiAl. Highlighted in red is the grain the diffraction pattern (figure 4.68) is taken from. Table 4.6 contains the 30 largest d-values for theta alumina. The diffraction pattern in figure 4.68 has been indexed as theta alumina. The ratios of the reflexions are consistant with the table of d-values, the angles however don't fit completely. This should be investigated further in future work.

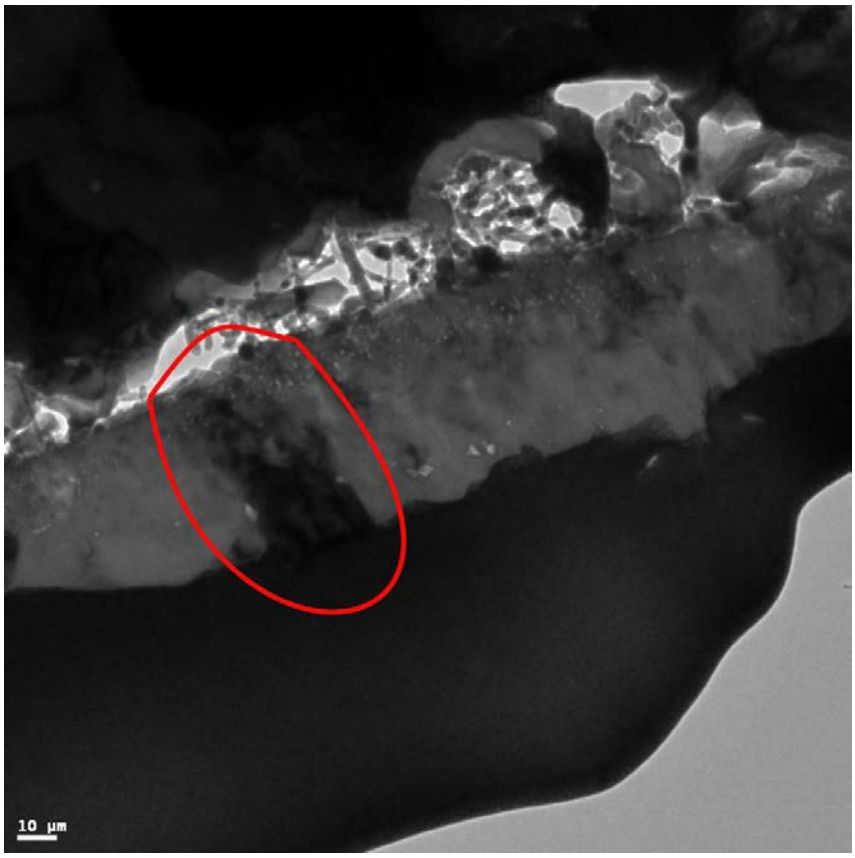

Figure 4.67: Brightfield image. The diffraction pattern taken from the highlighted grain is shown in figure 4.68.

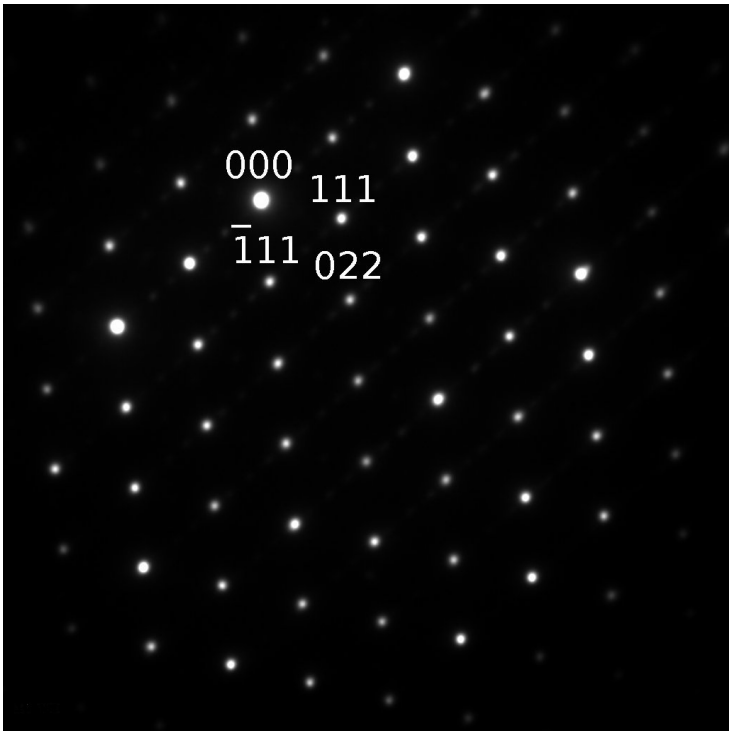

Figure 4.68: $[10\bar{1}]$ diffraction pattern of theta alumina.

The oxide formed on Ni_3Al could be one of two phases. Figure 4.69 shows this part of the sample, the oxide grain the diffraction patterns are taken from is highlighted in red. The diffraction patterns for this grain (figures 4.70 to 4.72) to have been indexed as gamma alumina. Table 4.7 gives the values as published in the ICSD [10], which were used for calculation.

However, the chemical composition gives hints that this oxide might well be a nickel-aluminate spinel. More on this subject will be presented in the discussion in chapter 4.

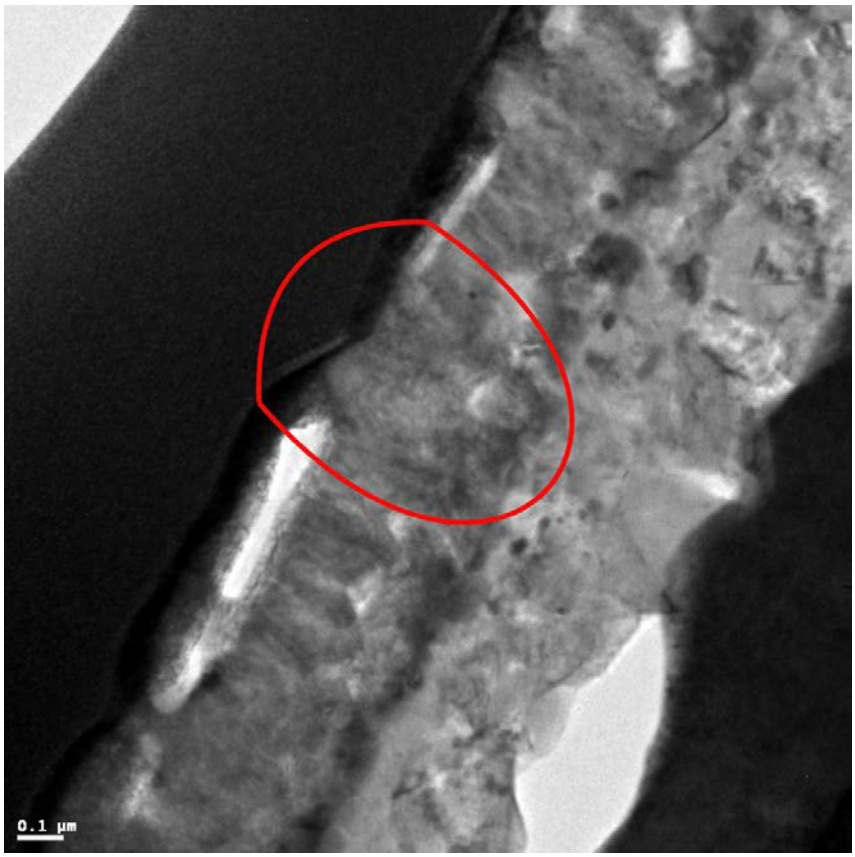

Figure 4.69: Brightfield image. The oxide grain the diffraction pattern is taken from is highlighted in red.

H	K	L	2Theta	d-value	Intensity
1	1	1	19.48	4.5536	59.0
2	2	0	32.07	2.7885	368.5
3	1	1	37.80	2.3780	1000.0
2	2	2	39.55	2.2768	64.1
4	0	0	45.99	1.9718	506.8
3	3	1	50.39	1.8094	0.3
4	2	2	57.17	1.6099	114.4
5	1	1	60.99	1.5179	286.2
3	3	3	60.99	1.5179	49.4
4	4	0	67.07	1.3942	678.7
5	3	1	70.59	1.3331	5.0
4	4	2	71.75	1.3145	0.0
6	2	0	76.29	1.2470	40.7
5	3	3	79.65	1.2028	84.4
6	2	2	80.76	1.1890	0.0

Table 4.7: Powder pattern table for gamma alumina, taken from the ICSD Karlsruhe [10].

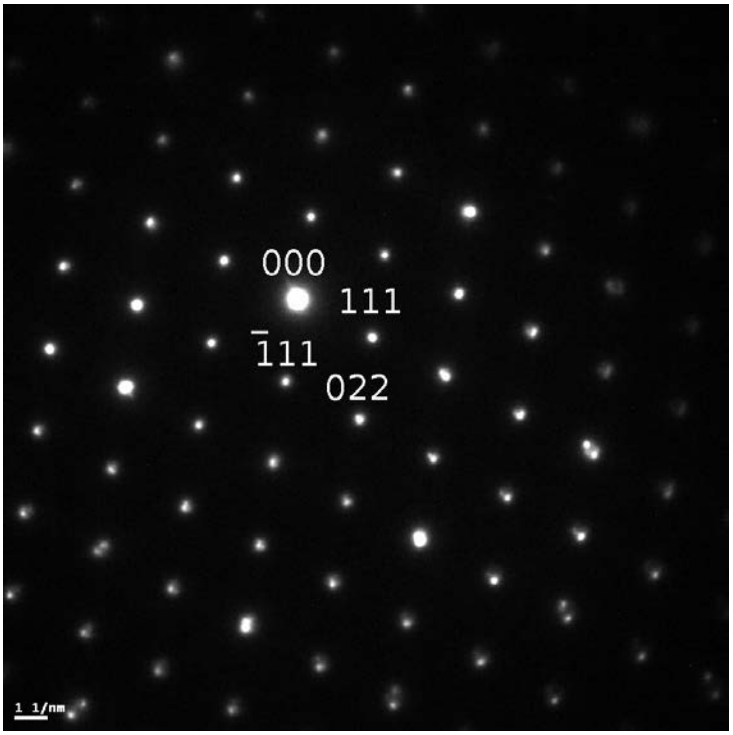

Figure 4.70: $\left[10\bar{1}\right]$ diffraction pattern of gamma alumina.

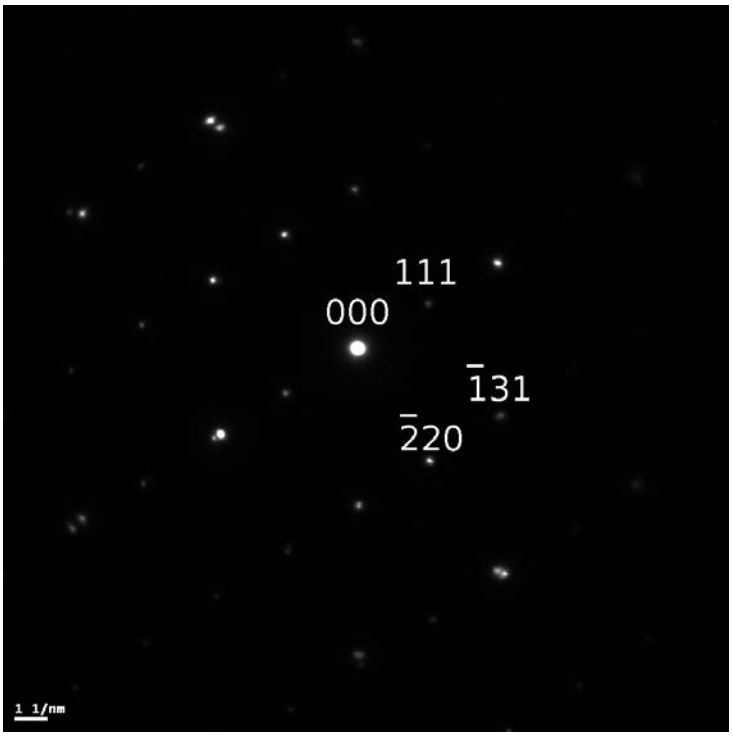

Figure 4.71: $\left[\overline{1}\overline{1}2\right]$ diffraction pattern of gamma alumina.

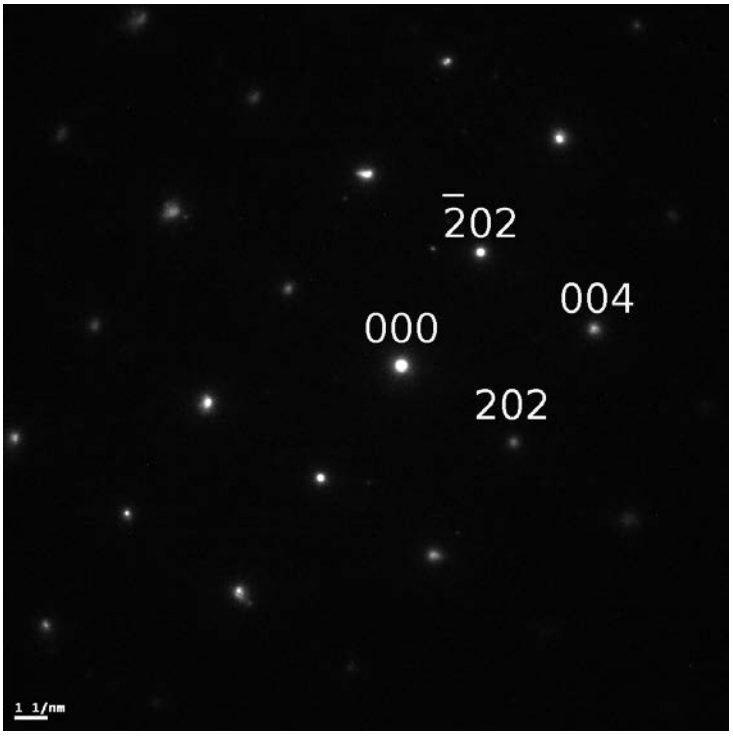

Figure 4.72: $\left[0\overline{1}0\right]$ diffraction pattern of gamma alumina.

4.5.2 High Pt Specimens

The TEM cross section of a high Pt specimen after 1100°C confirms the SEM evidence that there is no difference in oxides growing on NiAl (light grey in figure 3.63) as compared to $PtAl_2$ (dark grey in figure 4.63). There are a few voids at the oxide/metal interface. No distinct zone of aluminium depletion can be seen in the metal at the interface, as is the case with the low Pt specimens discussed above.

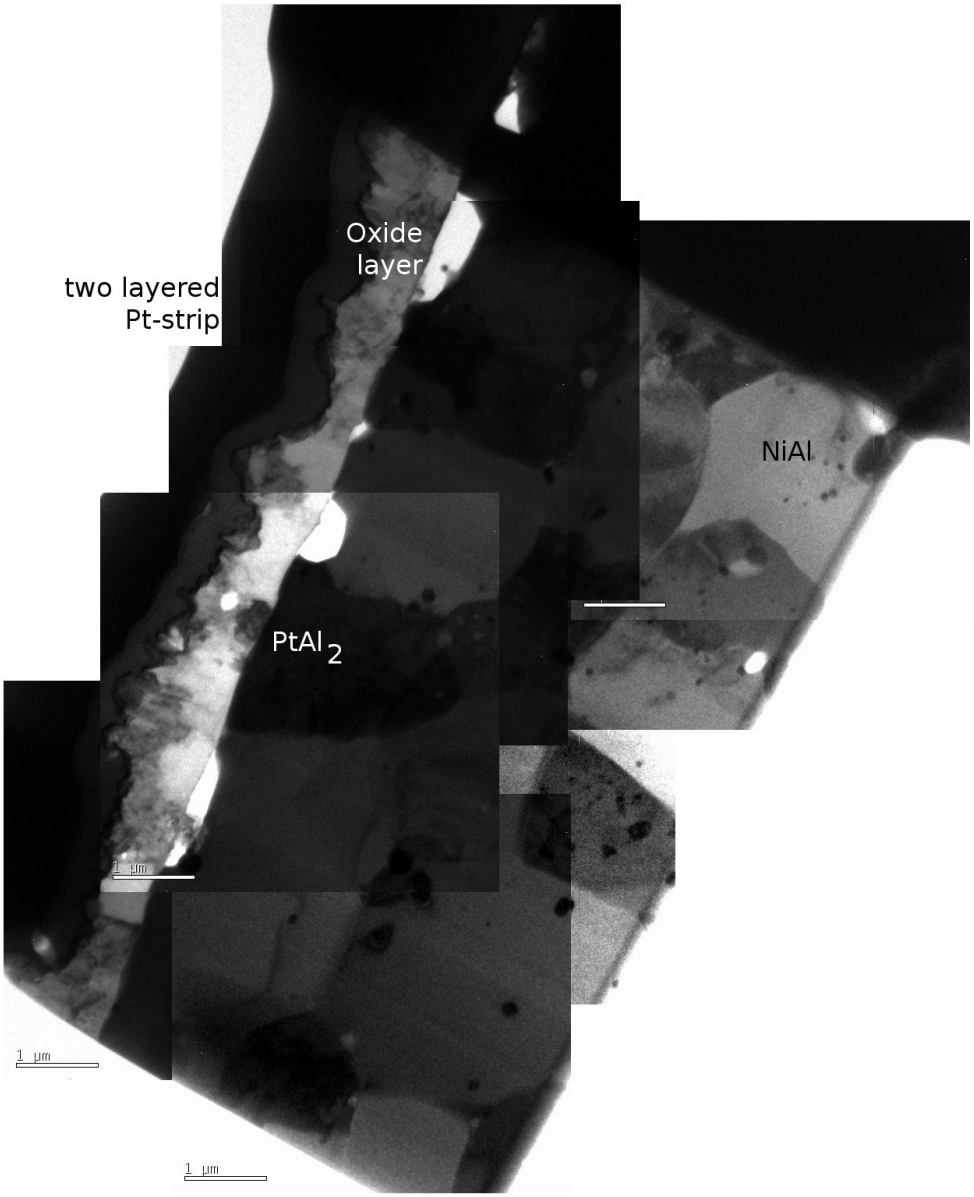

Figure 4.73: Montage of TEM images, showing a cross section through a high Pt specimen after 7 minutes at 1100°C.

Electron diffraction

For the high-Pt specimens only diffraction patterns of the metal phases were taken. These were done to make sure of the phases being NiAl and $PtAl_2$ as the EDX analysis suggested.

In figure 4.74 the exact phases the diffraction patterns are taken from are labled in red. Tables 4.5 and 4.8 give the d-values of NiAl and $PtAl_2$ as published on the ICSD [10], that were used for indexing.

Figures 4.75 to 4.77 show 3 different zone axis of NiAl and figures 4.78 to 4.80 show 3 different zone axis for $PtAl_2$.

In Figure 4.75 only the bright reflexions were indexed and correspond to the table of d-values. The origin of the weaker reflexions remains unknown.

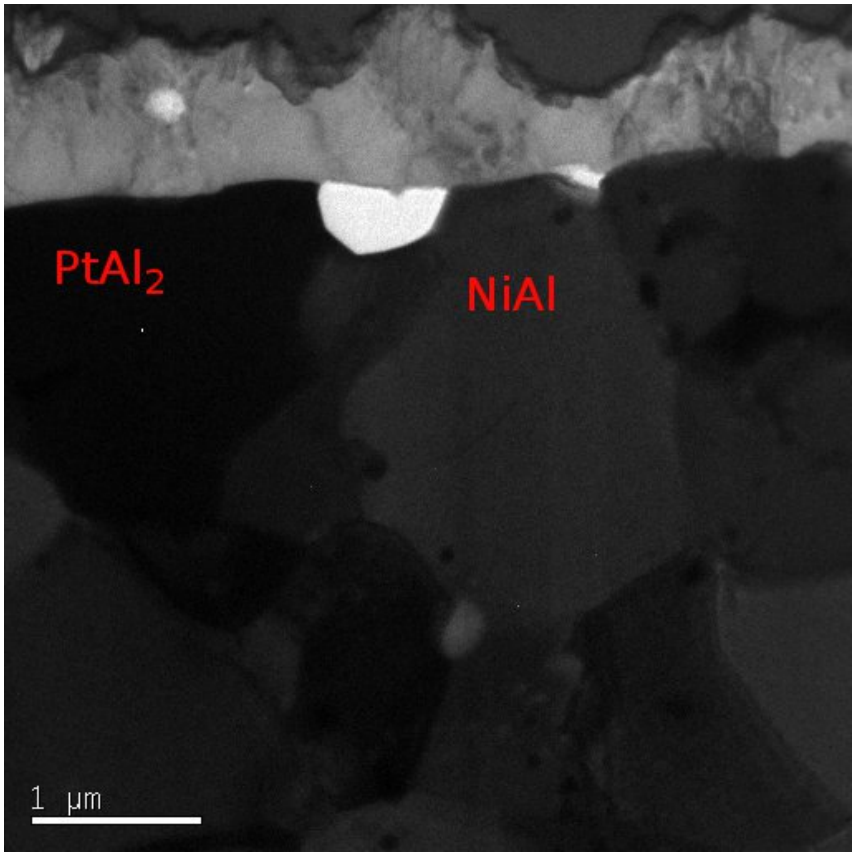

Figure 4.74: Brightfield image, showing the bond coat phases the diffraction patterns were taken from.

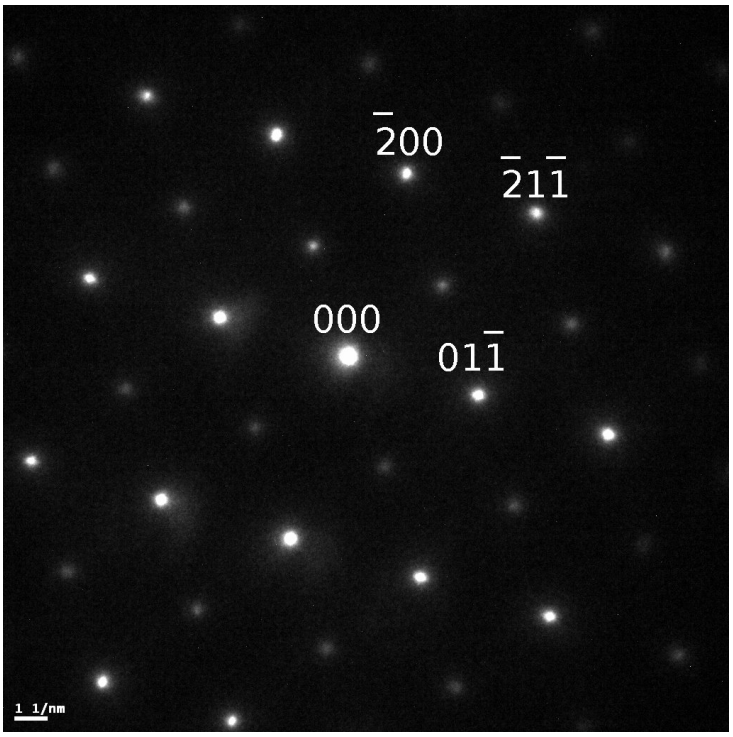

Figure 4.75: [011] diffraction pattern of NiAl.

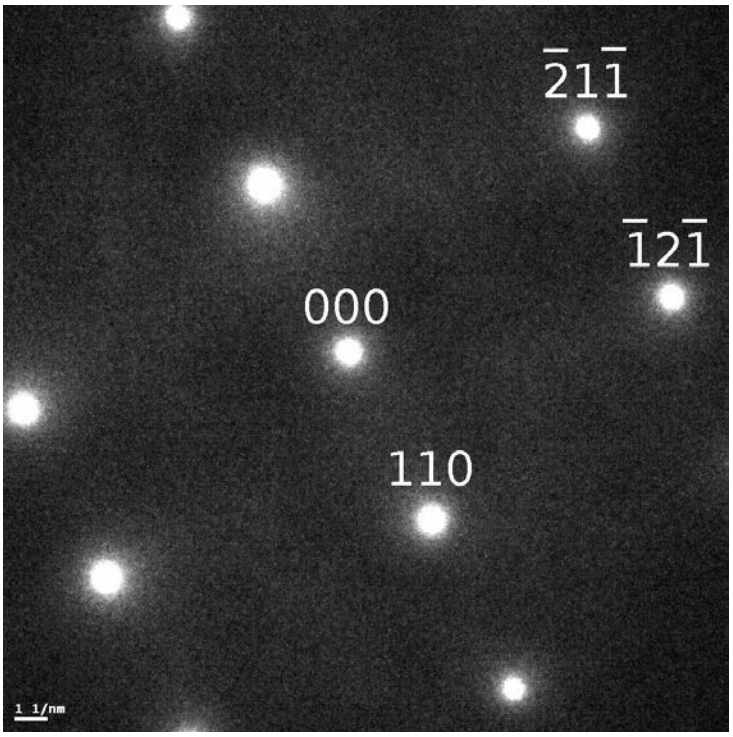

Figure 4.76: $\left[\bar{1}13\right]$ diffraction pattern of NiAl.

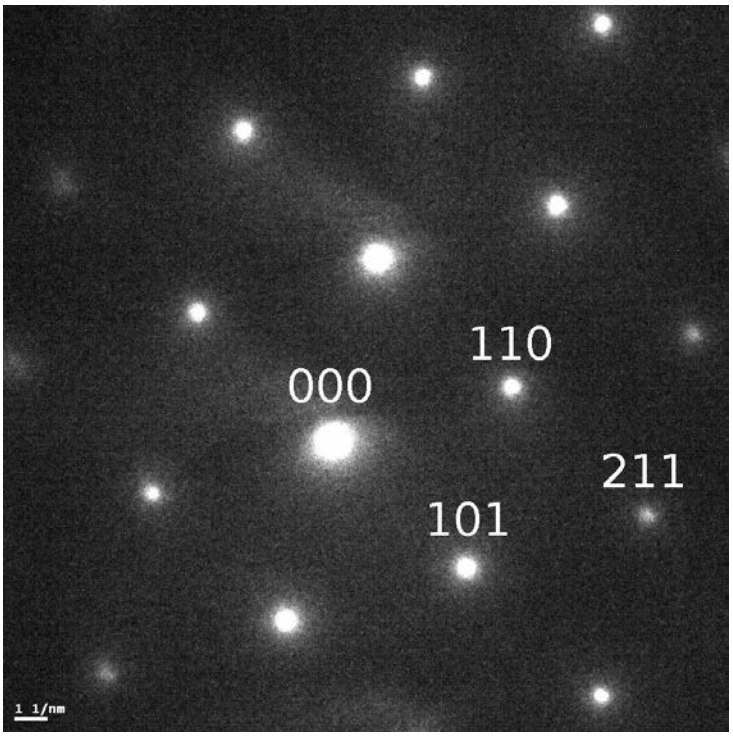

Figure 4.77: $\left[\bar{1}11\right]$ diffraction pattern of NiAl.

H	K	L	2Theta	d-value	Intensity
1	1	1	26.09	3.4121	1000.0
2	0	0	30.22	2.9550	265.0
2	2	0	43.26	2.0895	601.9
3	1	1	51.22	1.7819	438.6
2	2	2	53.68	1.7061	67.1
4	0	0	62.84	1.4775	89.5
3	3	1	69.24	1.3558	161.8
4	2	0	71.31	1.3215	79.9
4	2	2	79.36	1.2064	166.5

Table 4.8: Powder pattern table for $PtAl_2$, taken from the ICSD Karlsruhe [10].

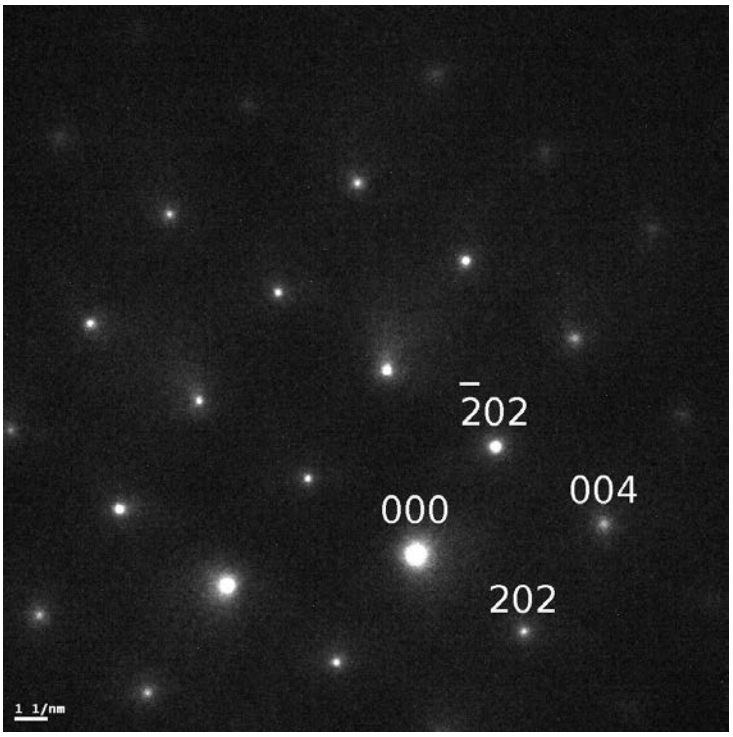

Figure 4.78: $\left[0\bar{1}0\right]$ diffraction pattern of $PtAl_2$.

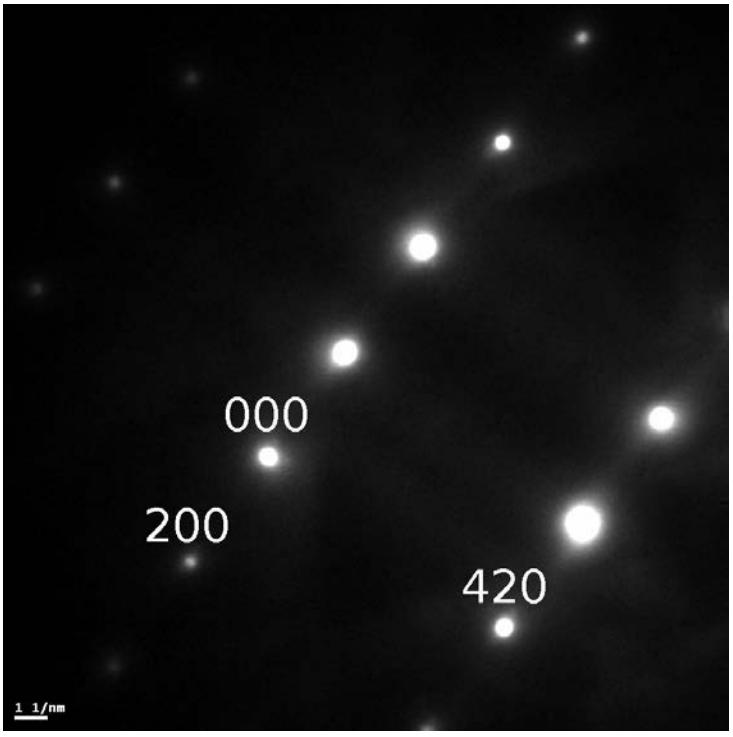

Figure 4.79: [001] diffraction pattern of $PtAl_2$.

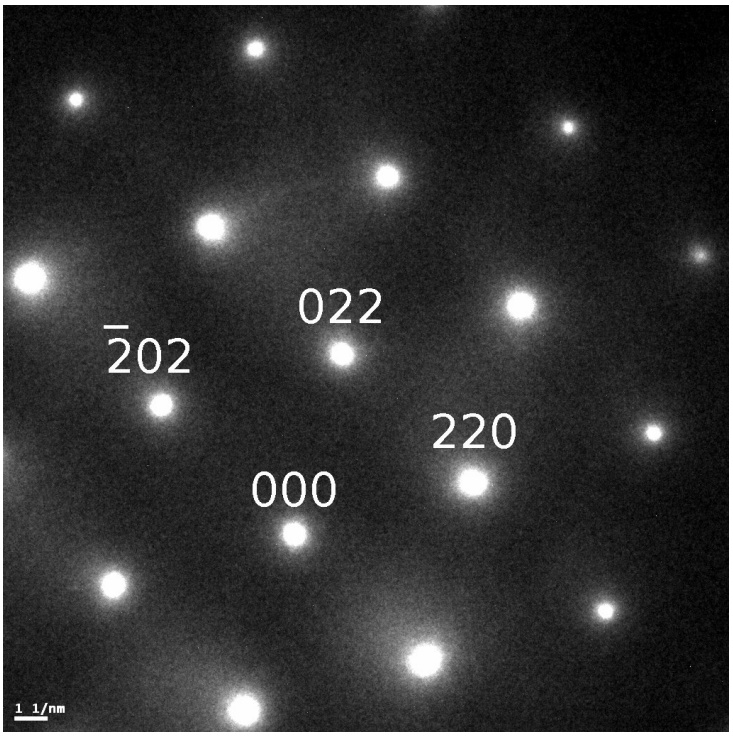

Figure 4.80: $\left[1\bar{1}1\right]$ diffraction pattern of $PtAl_2$.

EDX on the TEM was also used to confirm single-phase compositions of the NiAl and $PtAl_2$ phases in the high-Pt zone. Two representative analysis are given in table 4.9.

Phase	Al	Cr	Co	Ni	Pt
$PtAl_2$	47.62	8.93	2.49	11.44	28.01
NiAl	46.65	3.51	4.87	32.35	11.58

Table 4.9: Table showing the composition of $PtAl_2$ and NiAl in the high Pt specimens. All values are in atomic %.

Chapter 5

Discussion

5.1 The influences of aluminium content of bond coat phases on the formation of alumina phases.

Plan view SEM micrographs of alumina phases growing on mixed $NiAl/Ni_3Al$ bond coats (figures 4.8 to 4.21) show clear differences in the oxide morphology depending on the underlying bond coat phase and therefore connected to aluminium content. A look at the oxide morphology as it is displayed in greater detail by TEM micrographs (see figures 4.50 and 4.51) confirm this. Figure 4.51 also shows that the oxide growing on the Ni_3Al itself consists of 2 layers, an inner alumina layer and an outer layer with a more complex composition.

Elemental maps as well as STEM line scans show a clear difference in oxide composition of oxides grown over NiAl and Ni_3Al. This is confirmed by EDX analysis. Typical results of which can be seen in table 5.1.

Underlying BC phase	O at%	Al at%	Ni at%	Ti at%	Cr at%	Co at%
Ni_3Al	63.9	21.1	6.7	1.9	3.9	1.6
Ni_3Al	65.0	23.9	7.1	1.4	0.7	1.9
$NiAl$	66.9	30.5	n.d.	0.5	1.5	n.d.
$NiAl$	66.3	31.9	0.3	n.d.	0.8	n.d.

Table 5.1: Typical results of EDX analysis of different oxides grown on NiAl and Ni_3Al

These analysis suggest that the oxide growing on NiAl is indeed alumina, whereas the outer oxide layer growing on Ni_3Al seem to be a type of nickel-aluminate spinel.

As presented in chapter 4.5.1 the diffraction patterns of oxide grown on NiAl can be be indexed as θ-alumina (see figure 4.68). Due to the fact that it was only possible to obtain one pattern from different oxide grains in this area, the result however remains uncertain. According to Yang and co-workers [58] these platelets could also be heavily twinned γ-alumina.

For the oxide growing on Ni_3Al, there are two possibilities. As presented in chapter 4.5.1, they can be indexed as γ-alumina. The high nickel and cobalt levels on the outside of the oxide layer in this area, gave rise to the idea, that it might be a nickel-aluminate spinell. γ-alumina can be described as defect spinell [56, 57] as mentioned above, and so distinguishing between the two may be difficult. This can also be seen by comparing the peak lists for the phases in question (see tables 4.7, 5.2 and 5.3).

h	k	l	d-value	2Theta	Intensity
1	1	1	4.65000	19.071	20.0
2	2	0	2.84600	31.407	20.0
3	1	1	2.42700	37.010	100.0
4	0	0	2.01300	44.997	65.0
4	2	2	1.64150	55.973	8.0
5	1	1	1.54850	65.537	30.0
4	4	0	1.42320	65.537	60.0
5	3	1	1.36010	68.993	1.0
6	2	0	1.36010	74.411	1.0
5	3	3	1.22740	77.745	10.0
6	2	2	1.21340	78.814	1.0
4	4	4	1.16130	83.105	8.0

Table 5.2: Peak list for $NiAl_2O_4$. The Reference code for the database is 00-010-0339.

Due to the similarity of the structures between the spinels and γ-alumina, indexing the patterns as $NiAl_2O_3$ (see figures) gives the same results as for γ-alumina (see figures 4.70 and 4.72).

h	k	l	d-value	2Theta	Intensity
1	1	1	4.67900	18.951	8.0
2	2	0	2.86500	31.194	65.0
3	1	1	2.44400	36.743	100.0
2	2	2	2.33900	38.456	2.0
4	0	0	2.02600	44.693	14.0
3	3	1	1.85960	48.942	4.0
4	2	2	1.65440	55.499	13.0
5	1	1	1.55970	59.191	27.0
4	4	0	1.43280	65.043	33.0
5	3	1	1.36980	68.436	1.0
6	2	0	1.28150	73.896	4.0
5	3	3	1.23590	77.111	5.0

Table 5.3: Peak list for $CoAl_2O_4$. The reference code for the database is 00-044-0160.

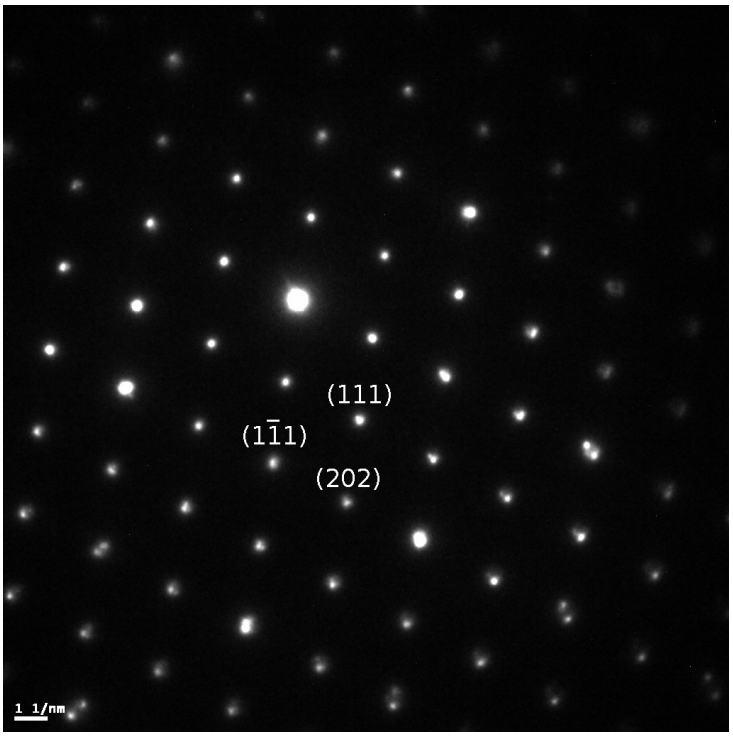

Figure 5.1: Diffraction pattern, showing the $\{0\bar{2}2\}$ zone axis for $NiAl_2O_4$.

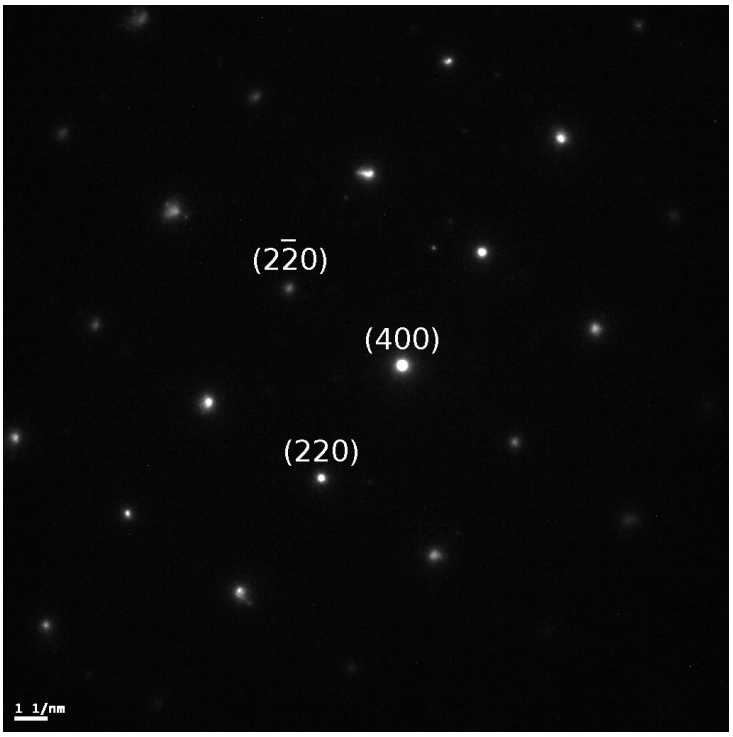

Figure 5.2: Diffraction pattern, showing the {008} zone axis for $NiAl_2O_4$.

Since the TEM diffraction is inconclusive, a comparison of oxide morphology (figures 4.8 to 4.21) with results presented in the literature is used as an estimate to what oxide phases are growing on $\beta - NiAl$ and $\gamma' - Ni_3Al$ respectively. The whisker like morphology of the oxide growing on top of NiAl grains compares to θ-alumina as reported by many authors [67, 68, 69, 70, 71].

Tolpygo and Clarke report even after a complete transformation from θ- to α-alumina, the oxide layer retains the whisker-like morphology of the θ-alumina [67]. They attribute this to the fact that cation diffusion is believed to be much faster in θ than it is in α-alumina.

This assumption is backed by estimates of parabolic rate constants for the oxide growing on $\beta - NiAl$ (see figure 4.51). The oxide thickness, h, is 500nm after 7 minutes of oxidation, if we use these in the equation

$$k_p = \frac{h^2}{t} \tag{5.1}$$

it gives a k_p of $5.95 * 10^{-16} m^2 s^{-1}$ which is much higher than that of α-alumina, which

can be calculated thus [30]:

$$k_p = 7.65 * 10^{-7} exp\left[-\frac{275000}{8.314 * T}\right] m^2 s^{-1} = 2.61x10^{-17} m^2 s^{-1} at 1100°C \qquad (5.2)$$

This confirms that the oxide layer consists of a faster growing transient alumina.

5.2 Void formation along the bond coat/oxide interface

The first question with regards to the voids seen in TEM samples (figures 4.50 and 4.51) was whether they are genuine, or produced in the final thinning stages of ion milling. Some of them, like the one on the phase boundary shown in figure 4.50, could be an artefact, since the author saw it growing during the final thinning process. It could however also have been a small, pre-existing void that was cut into at this stage.

From comparison with SEM cross section imaging, it can be assumed that there are genuine voids forming at the bond coat/oxide interface during oxidation in the low Pt specimens (see figure 5.3) as well as the high Pt specimens (see figures 5.4 and 5.5).

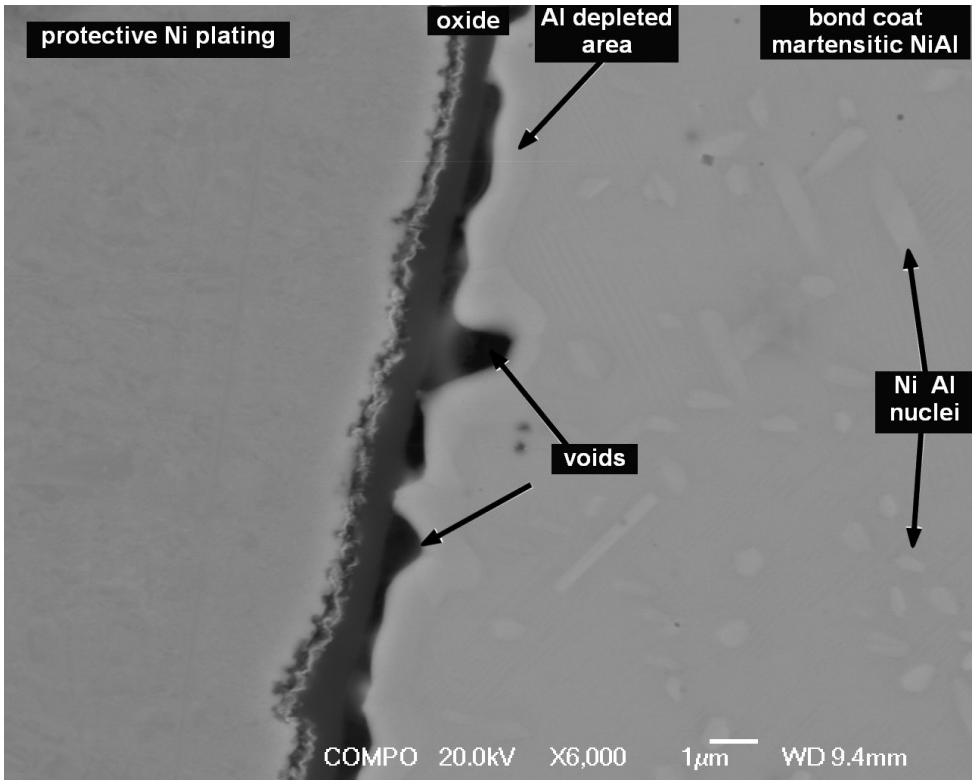

Figure 5.3: Voids on low Pt specimens

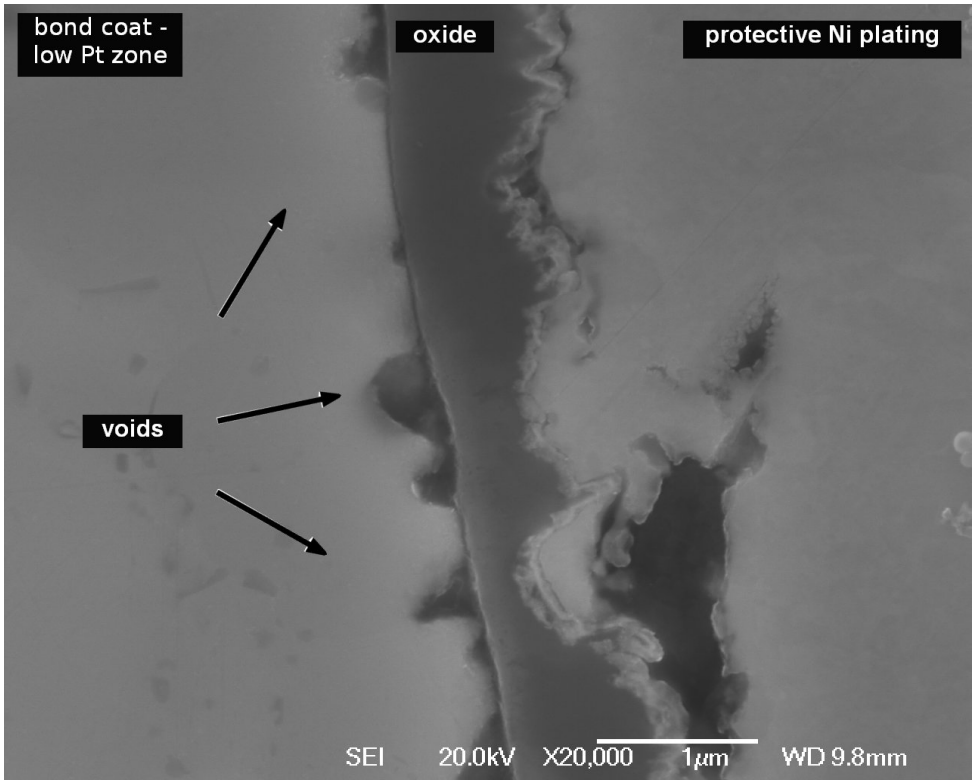

Figure 5.4: Voids on high Pt specimens

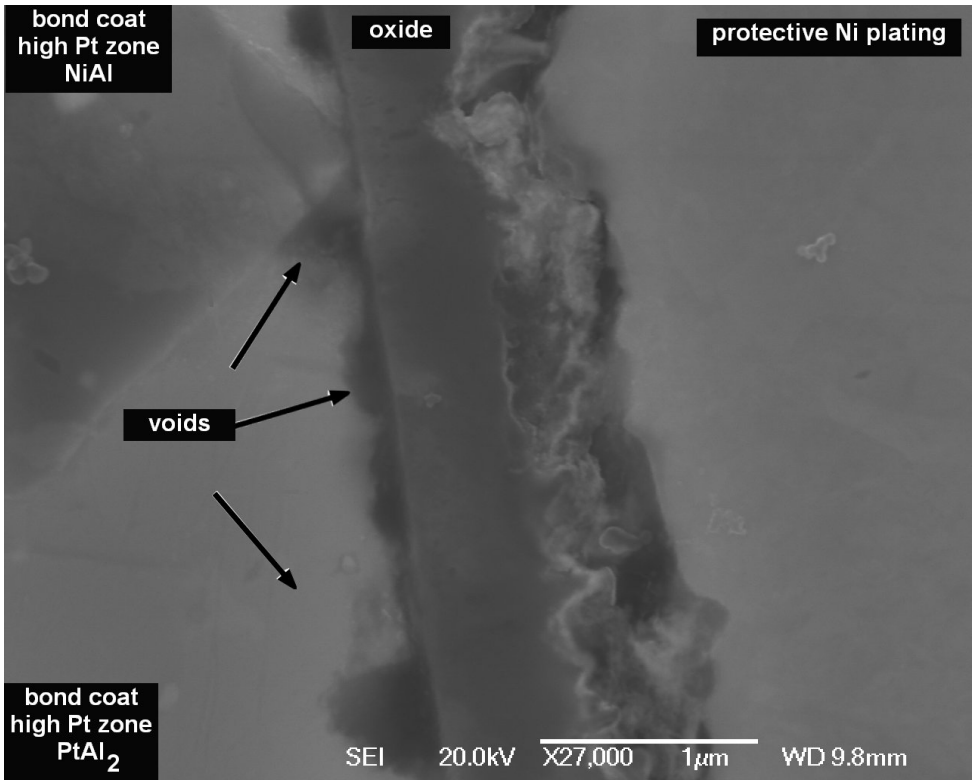

Figure 5.5: voids on high Pt specimens

One thing that became apparent from the TEM cross sections was that there seem to be significantly more voids at the oxide/metal interface at the martensitic NiAl grains as compared to Ni_3Al grains (see figures 4.50 and 4.51 above). The question arising therefore was, whether this could be due to the volume change associated with martensite transformation.

As mentioned earlier, the shrinkage due to martensite transformation is about 2% of the volume of the original NiAl grain. An estimation of the volume of voids, like the ones seen in figure 4.51 gives 13%. Though the volume change on martensite transformation may contribute, it is by no means large enough to explain this amount of void formation at the NiAl/oxide interface.

Brumm and Grabke were studying the void formation of NiAl with different aluminium levels and found more voids in samples with higher aluminium contents [72]. They state that this is due to nickel diffusing to the bulk, to compensate for the aluminium depletion in Ni-rich NiAl. Following this model, the samples in this study would be expected to show more voids forming on the Ni-rich Ni_3Al, rather than the Al-rich martensitic NiAl.

The explanation by Brumm and Grabke is contradicted by Haynes at all [37], who find different amounts of voids in samples with identical nickel and aluminium contents. They find that sulphur impurities may stabilise the voids, enabling them to become critical and grow by transport of excess vacancies from the surrounding NiAl to the voids. This effect of sulphur may play a role in the sampled investigated for this study, but since only EDX was used for chemical analysis, it was not possible to detect any sulphur.

A case, similar to this study, is presented by Svensson et al [68]. They find voids forming at the metal/oxide interface after 10 minutes of oxidation at 1050°C, that are later healed by newly forming oxide. Effects similar to this can also be observed at the oxide/metal interface on $\gamma' - Ni_3Al$ as seen in figure 4.51.

Tatlock et al [73] find these types of voids after oxidation for 200 hours at 900°C on FeCrAlRE alloys, during the formation of transient aluminas by outward cation movement. Some of these voids were filled by chromia. Martinez et al [74] find them on FeAl-alloys.

During oxidation aluminium is taken out of the alloy to form an oxide layer, which leaves vacancies. These vacancies congregate at the metal surface as more and more aluminium diffuses out. This process explains how voids can form at the oxide/metal interface, if enough vacancies congregate and are not previously destroyed by an inward moving interface. It is highly relevant for the short times the specimens in this study were exposed to high temperatures.

If these vacancies are destroyed by the interface moving inwards, consuming the metal, no voids can form. However, if the interface stays at the same level, with the oxide growing by aluminum diffusing out of the metal, voids would form and grow as more and more aluminium is taken out.

On the $\beta - NiAl$-grain the interface stays at the same level and therefore voids are produced in the metal just below the interface (see figure 5.6). This may be connected to transient oxides growing by outward diffusion of cation, but this would be the case for oxides growing on γ' as well as on β grains. On the $\gamma' - Ni_3Al$ interface is moving

inwards, with only a very small amount of voids forming. This process also explains the height difference between the oxide layer grown on $NiAl$ and on Ni_3Al when measured from the original interface (indicated by a green line in figure 5.6), compared to the over all oxide thickness on both phases, which is roughly the same.

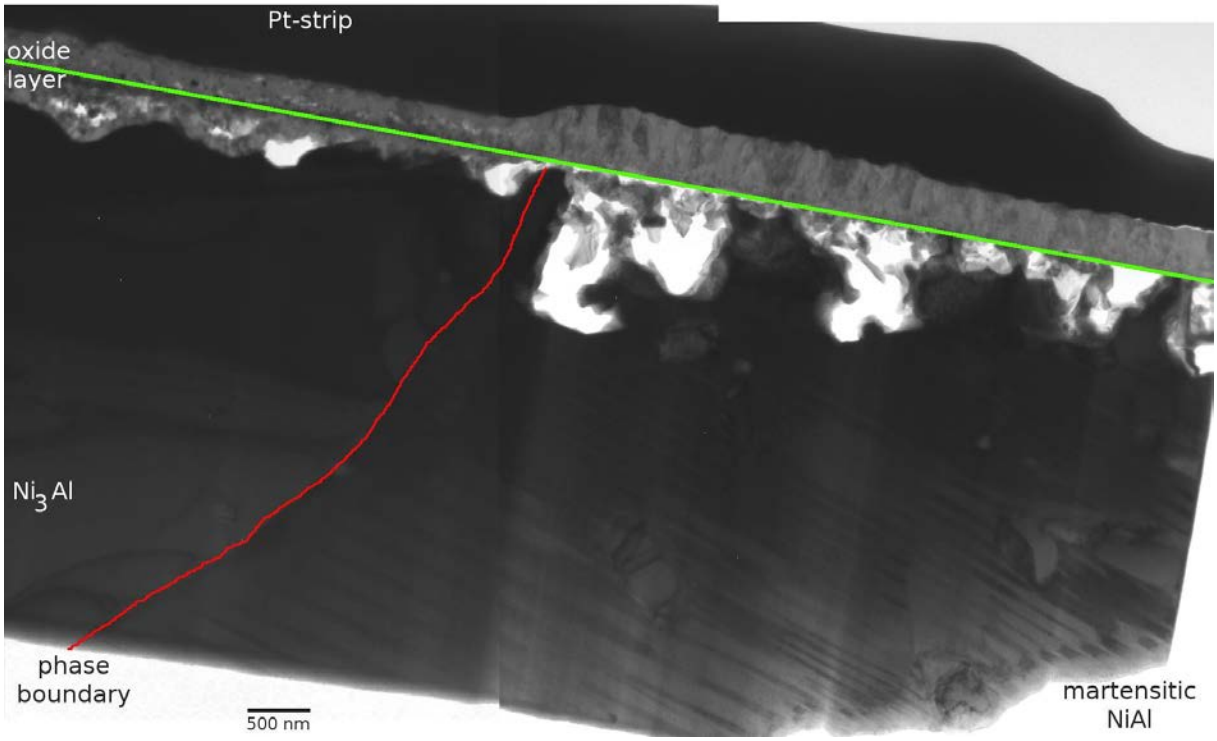

Figure 5.6: Oxide growing on $\beta - NiAl$ and $\gamma' - Ni_3Al$. The phase boundary is indicated in red. The green line shows the original polished surface of the sample, which happens to be the metal/oxide interface on $\beta - NiAl$, where as on the $\gamma' - Ni_3Al$ the interface moved inwards, replacing the metal with oxide.

5.3 Oxide thicknesses on high Pt specimens.

Oxide thicknesses were measured on the high platinum specimens after 1, 5, 10, 15, 20 and 25 hours of oxidation at 1100°C. Large scale spallation happened at 50, 75 and 100 hours at 1100°C and even though the oxide scale re-healed, no continuous oxide thickness could be measured from those. The detailed measurements of oxide thickness are given in Table 5.4 together with the mean value and standard deviation.

The variation of mean oxide thickness with exposure time at 1100°C is shown in Figure

Time at Temperature, Hours	1	5	10	15	20	25
Oxide thickness, μm	1.02	0.84	1.38	1.82	1.78	1.81
	0.74	1.13	1.02	1.44	1.16	1.79
	0.64	1.01	1.35	1.54	1.27	1.36
	0.85	1.26	1.09	1.54	1.69	1.30
	0.93	1.36	1.02	1.53	1.67	1.65
	0.80	1.75	1.79	1.32	1.89	1.70
	1.19	1.29	1.67	1.22	1.24	1.58
	0.93	1.18	1.02	1.49	1.13	1.72
	1.86	1.31	0.96	1.48	1.21	1.72
	1.06	0.73	0.41	1.56	1.80	1.39
	0.87	1.06	2.21	1.71	1.16	0.83
	0.96	1.17	2.12	1.25	1.53	1.60
	0.86	1.00	1.82	1.24	1.73	1.46
	1.26	1.28	1.88	1.58	1.40	1.49
	0.93	1.28	1.38	1.60	1.24	1.66
	0.89	1.00	1.92	1.41	1.56	1.13
	0.99	1.19	1.81	1.42	1.91	1.65
	1.17	1.33	1.09	1.44	1.59	1.47
	1.19	0.89	1.32	1.99	1.62	1.46
	0.99	1.21	1.27	1.56	1.46	1.57
	0.93	0.62	1.13	1.32	1.46	1.49
	1.07	1.01	1.55	1.75	1.00	1.54
	0.80	0.73	1.19	1.51	1.56	1.62
Mean Thickness, μm	1.00	1.11	1.41	1.51	1.48	1.52
Standard Deviation, μm	0.24	0.25	0.44	0.19	0.26	0.22

Table 5.4: Oxide Thickness Measurements on the High-Pt Coating for Increasing Exposures at 1100°C.

5.7. Clearly, there is a very rapid initial rate of oxidation which decays after a few hours exposure to low oxidation rates. These kinetics are reminiscent of those found by Pragnell et al. [75] on alumina-forming FeCrAlY alloys which were attributed, in that work, to the transition from faster-growing θ-alumina to the more protective α-alumina. A similar transition is likely to be occurring here although the timescales are appreciably shorter: approximately <2 hours at 1100°C in the present case compared with ∼30 hours at 900°C and ∼10 hours at 925°C in Pragnells work. The differences are likely to be due to the higher temperature used in the present work.

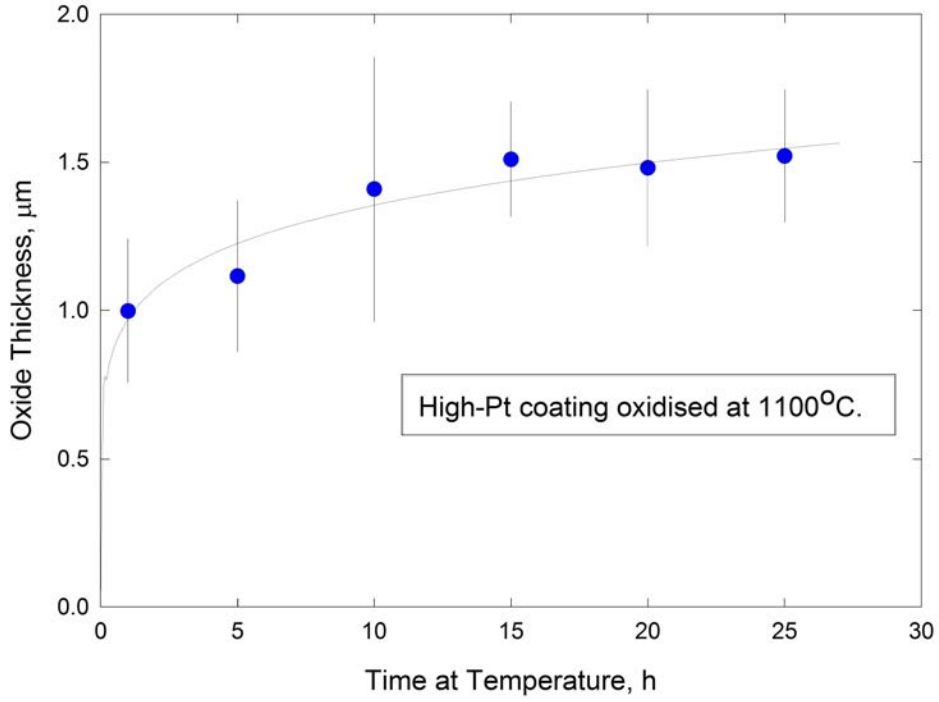

Figure 5.7: The Variation of Mean Oxide Thickness with Exposure Time at 1100°C.

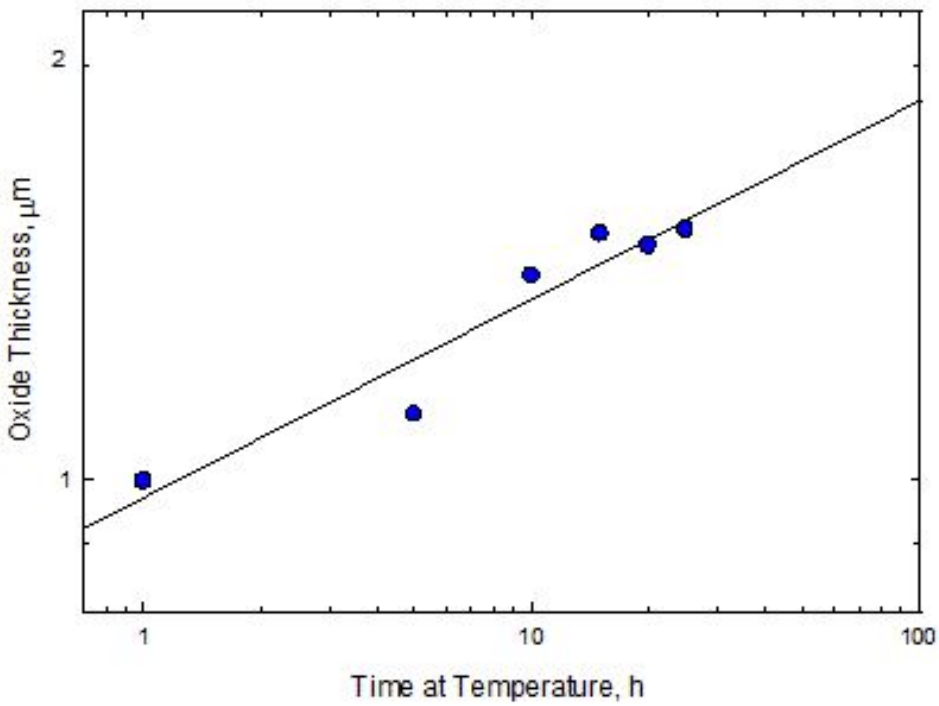

Figure 5.8: Log-log Plot of Oxide Thickness against Exposure Time at 1100°C

Pragnell et al. [75] described their observed dependence of oxide thickness against

exposure time by a hyperbolic function but the present results can adequately be described by a simple power-law dependence. This can be appreciated from the log-log plot of Figure 5.8. The best-fit line shown corresponds to the expression:

$$h = kt^{0.145} \tag{5.3}$$

where h is the oxide thickness in metres, t is exposure time in seconds and k is a constant having a value of $2.96 * 10^{-7} m.s^{-0.145}$ at 1100°C. This expression is plotted as the solid line in Figure 5.7.

5.4 Development of high-Pt coating at different times at 1100°C and it's implications on the Ni-Al-Pt ternary phase diagram

The results of this study suggest a two phase field, where Gleeson at al [6] only show a NiAl stability field within the ternary diagram (see fig. 5.9).

Since neither method is an equilibrium method, the results of both studies are comparable. Gleeson at al [6] used diffusion couples for their experiments, which results in a flux. The same is true for the experimental setup used in this study, where diffusion of aluminium through the bond coat is the main driving force.

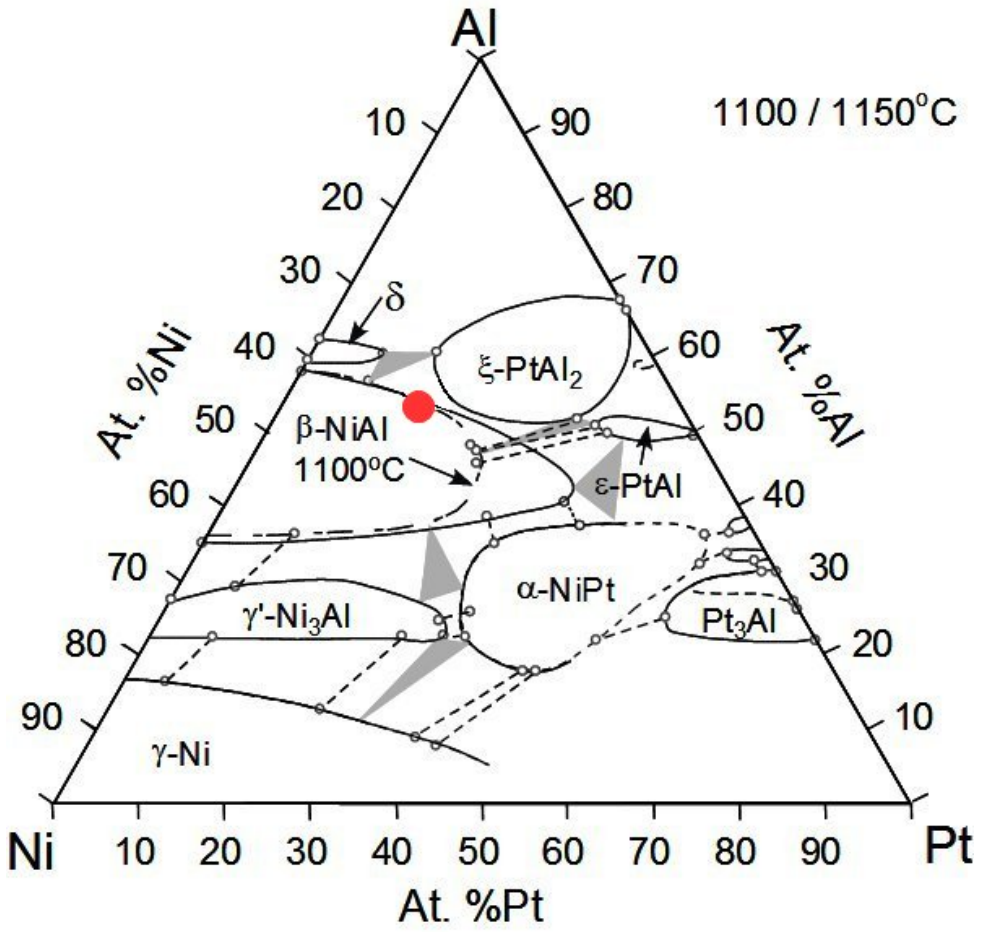

Figure 5.9: Original Ni-Al-Pl ternary diagram by Gleeson et al [6]. The red dot marks the as-received, bulk composition of the outer layer of the coating.

As has been shown in the results section, up to 15 hours at 1100C, there clearly are two phases present in the outer part of the bond coat. They differ in platinum content by about 10 at%. When superimposed on the Ni-Al-Pt diagram, they both fall within the NiAl phase field as it is shown in figure 5.9. It must therefore be assumed that this either is not a single phase field or the presance of additional elements within the coating is having a bigger influence than first assumed.

The only elements in the bond coat that have to be taken into account there, are chromium and cobalt. Jackson and Rairden [76] found that most alloys can be simplified by equating cobalt to nickel, therefore leaving 4 elements that have to be considered: chromium, nickel, aluminium and platinum.

As a first step, looking at the Ni-Al-Cr ternary diagram [9] shows that chromium additions very much affect the dimensions of the NiAl phase field. An addition of 3-5

at.% Cr starts to shrink the single phase field (see figure 5.9). The specimen used in this study typicly contained 3-6 at.% of chromium and therefore fall into the NiAl stability field on or around the green line as depicted in figure 5.10.

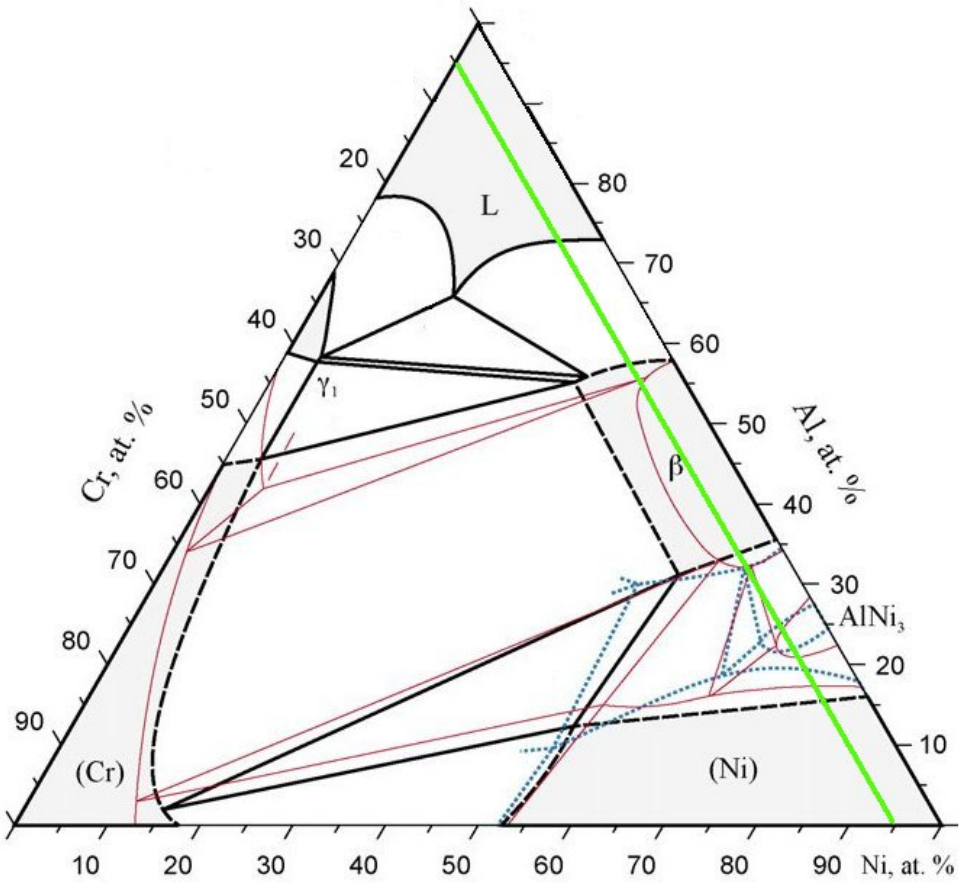

Figure 5.10: Ni-Al-Cr Diagram by Grushko et al [9] for 1150°C. The green line showing the 5 at.% Cr line.

To gain a good understanding of the effects of Cr it is helpful to look at the quaternary system Ni-Al-Cr-Pt by forming a 3-sided pyramid, with one element at each corner (see figure 5.11). Due to the chemical composition of the specimens, the area around the Ni-Al (marked red in figure 5.11) is of the most interest. Folding the pyramid open along this binary line gives the diagram shown in figure 5.12, where the ternary diagrams of the Ni-Al-Pt and the Ni-Al-Cr system are joined together. This shows that the stability fields of $\beta - NiAl$ and $\gamma' - Ni_3Al$ fit well.

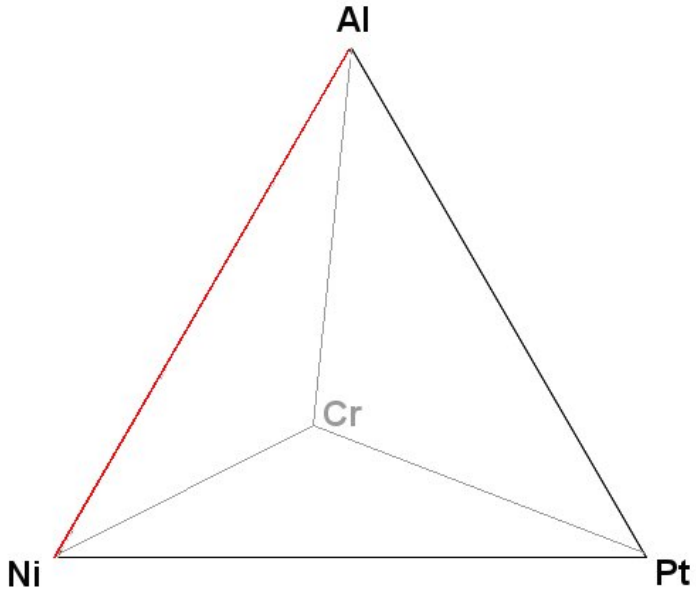

Figure 5.11: Schematic of the quaternary Ni-Al-Cr-Pt system

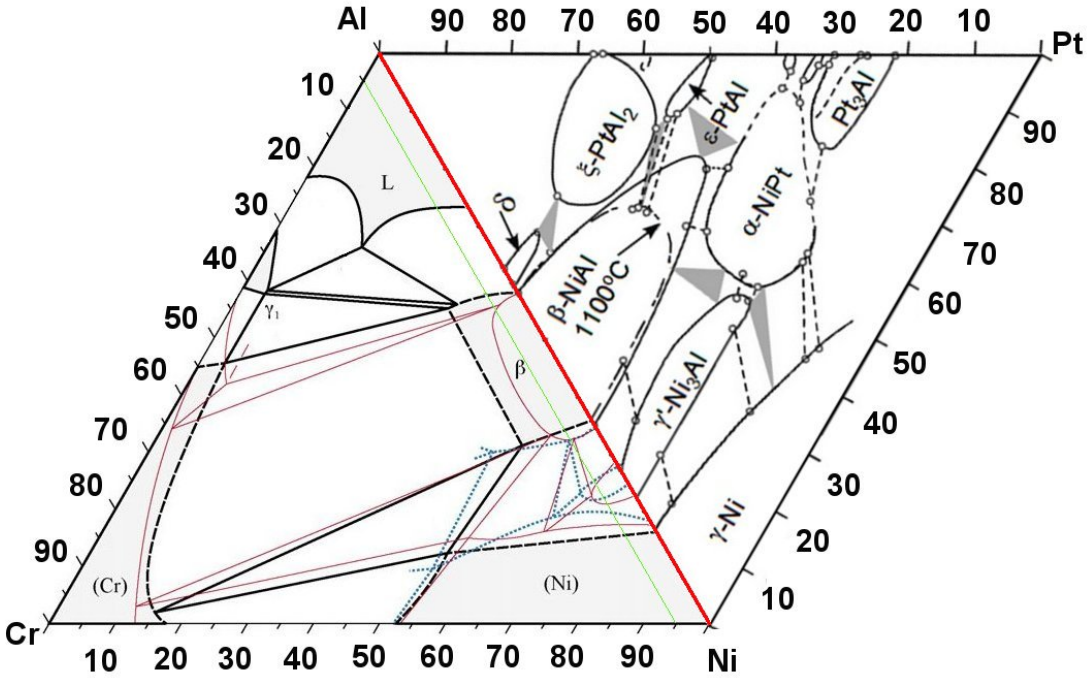

Figure 5.12: Quaternary system derived by joining 2 ternary diagrams at the binary Ni-Al line

A possible stability field for NiAl is shown in figure 5.13. The dimensions stem from the results presented in chapter 4.4. The bulk chemistry of the outer, high-Pt layer of the bond coat would lie within the single NiAl phase field (dashed line in figure 5.13), but as can be seen in figures 4.29, 4.31 and 4.33 after oxidation for 1, 5 and 10 hours at 1100°

there are clearly 2 phases present. The grey phase is β-NiAl with an average platinum content of 10 at. %, the white phase is either a β-NiAl with a higher platinum content or $\xi - PtAl_2$, the average platinum content of this phase is 20 at. %.

This presence of two phases shows that the single NiAl phase field must shrink with the addition of chromium.

Since the specimens used in this study don't have a higher platinum content than 20 at %, nothing can be said about the influence of chromium on the $PtAl_2$ phase field. A look at the Al-Pt-Cr diagram plublished by Suess et Al [52] however suggests that there is a single phase field for $PtAl_2$ up to about 18 at. % of chromium within the alloy.

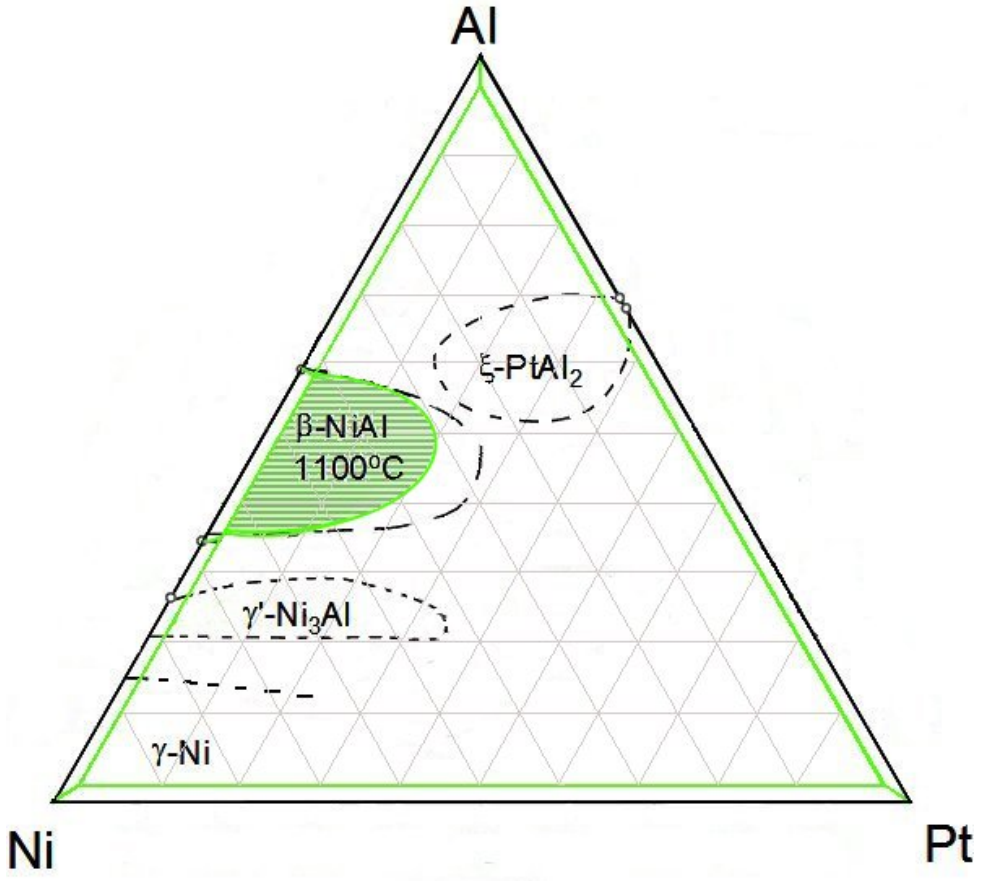

Figure 5.13: In green the proposed NiAl stability field in the presence of 3-5 at. % chromium. The green triangle indicates a level above the Ni-Al-Pt diagram by Gleeson et al. [6], corresponding to the chromium levels in the specimens. The dashed lines represent the phase stability fields in said diagram.

Figure 5.14 shows the path the coating takes after increasing times at 1100°C. This path was used to determine the size of the green NiAl stability fields in figures 5.13 and

5.14. It clearly limits the single phase field towards the aluminium and platinum ends of the phase diagram. The red point in figure 5.14, representing 15 hours at 1100°C was placed on the line surrounding the single phase field, as the SEM micrographs suggest it is mostly 1 phase, but at 10 hours there are clearly still two phases present, so the transition must happen within that timeframe. The results for 20 and 25 hours at 1100°C are both represented with the magenta point in figure 5.14, since there is virtually no difference in composition between the two. The actual EDX analysis the datapoints in figure 5.14 are derived from is given in tables 5.5 to 5.13

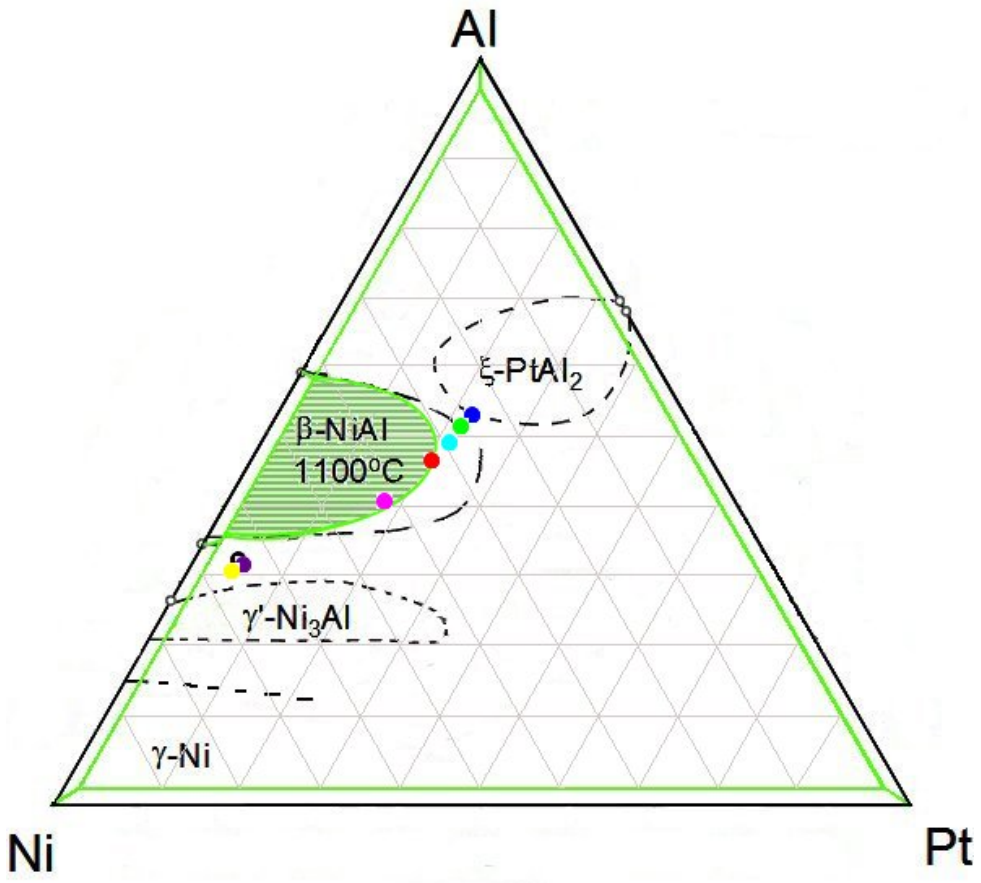

Figure 5.14: The same diagram as in figure 5.13, superimposed are the compositions of the bond coat at different times at 1100°C. Dark blue: 1 hour, green: 5 hours, light blue: 10 hours, red: 15 hours, magenta: 20 and 25 hours, black: 50 hours, purple: 75 hours, yellow: 100 hours.

Spectrum	Al	Cr	Co	Ni	Pt
Spectrum 1	48.6	1.8	5.1	40.2	4.1
Spectrum 2	48.4	1.8	5.6	39.7	4.2
Spectrum 3	48.1	2.6	6.1	39.6	3.3
Spectrum 4	49.8	4.1	3.9	29.7	12.3
Spectrum 5	53.2	6.7	2.3	15.8	21.8
Spectrum 6	52.7	7.1	2.3	15.9	21.8
Spectrum 7	48.7	1.0	5.1	39.2	6.0
Spectrum 8	51.1	3.0	4.1	30.3	11.4
Spectrum 9	50.2	3.4	4.0	30.0	12.2
Spectrum 10	50.8	4.2	3.5	26.0	15.2
Spectrum 11	53.4	7.6	2.2	13.8	22.6
Spectrum 12	53.4	7.9	2.0	13.1	23.3
Spectrum 13	52.0	6.4	3.1	19.7	18.6
Spectrum 14	48.5	1.9	4.9	37.7	6.8
Spectrum 15	52.3	5.9	3.1	21.0	17.4
Spectrum 16	53.4	7.8	1.9	15.4	21.2
Spectrum 17	49.9	4.0	4.2	29.9	11.8
Spectrum 18	51.3	6.3	3.2	23.5	15.5
Spectrum 19	49.3	3.1	4.7	34.7	8.0
Spectrum 20	51.1	6.7	3.9	24.9	13.1
Spectrum 21	48.0	1.6	5.6	39.6	5.1
Spectrum 22	52.5	7.4	2.9	20.1	16.8
Spectrum 23	51.3	5.4	3.8	25.9	13.4
Spectrum 24	50.5	6.0	4.0	26.1	13.2
Spectrum 25	48.0	1.9	5.8	40.0	4.1
Spectrum 26	48.1	1.7	6.1	40.3	3.6

Table 5.5: Actual EDX analysis of the high Pt coating after oxidation for 1 hour at 1100°C. Values given are atomic%.

Spectrum	Al	Cr	Co	Ni	Pt
Spectrum 1	50.9	3.7	2.8	21.3	21.1
Spectrum 2	50.8	3.6	2.8	21.3	21.3
Spectrum 3	50.9	3.3	3.2	22.1	20.3
Spectrum 4	50.7	3.8	2.9	21.8	20.6
Spectrum 5	50.6	3.8	2.9	22.0	20.4
Spectrum 6	50.6	4.0	3.1	21.7	20.4
Spectrum 7	50.6	4.5	2.9	20.8	20.9
Spectrum 8	47.3	1.5	4.2	36.0	10.8
Spectrum 9	49.6	3.9	3.4	26.5	16.4
Spectrum 10	51.1	5.2	2.7	19.3	21.5
Spectrum 11	51.5	5.4	2.5	18.4	22.0
Spectrum 12	48.3	3.1	3.8	31.3	13.3
Spectrum 13	49.6	4.7	3.0	23.8	18.6
Spectrum 14	48.7	3.3	3.7	30.4	13.6
Spectrum 15	49.7	4.6	3.1	23.7	18.7
Spectrum 16	49.3	9.6	2.9	19.9	18.0
Spectrum 17	46.9	2.36	4.7	36.4	9.4
Spectrum 18	49.8	4.9	3.1	23.5	18.4
Spectrum 19	49.9	5.8	2.9	21.3	19.8
Spectrum 20	49.5	5.4	3.6	22.8	18.5
Spectrum 21	46.5	1.5	4.8	38.9	8.1
Spectrum 22	45.9	1.9	5.1	40.3	6.6
Spectrum 23	45.7	1.3	5.3	41.8	5.7
Spectrum 24	45.6	1.5	5.4	42.4	4.9

Table 5.6: Actual EDX analysis of the high Pt coating after oxidation for 5 hours at 1100°C. Values given are atomic%.

Spectrum	Al	Cr	Co	Ni	Pt
Spectrum 1	48.0	2.4	3.9	32.5	12.9
Spectrum 2	47.7	4.5	3.4	25.3	18.8
Spectrum 3	48.2	4.4	3.3	23.8	20.1
Spectrum 4	48.5	4.7	3.0	22.8	20.8
Spectrum 5	48.1	4.1	3.5	24.4	19.7
Spectrum 6	48.1	3.7	3.3	26.0	18.6
Spectrum 7	46.1	2.7	4.1	33.3	13.5
Spectrum 8	47.7	3.3	3.8	27.1	17.9
Spectrum 9	47.8	3.9	3.6	26.0	18.5
Spectrum 10	47.5	4.3	3.4	27.0	17.6
Spectrum 11	43.1	13.1	3.2	24.2	16.1
Spectrum 12	48.7	3.0	3.4	25.2	19.3
Spectrum 13	47.1	4.2	3.7	26.1	18.6
Spectrum 14	52.9	3.4	0.3	24.6	18.5

Table 5.7: Actual EDX analysis of the high Pt coating after oxidation for 10 hours at 1100°C. Values given are atomic%.

Spectrum	Al	Cr	Co	Ni	Pt
Spectrum 1	44.4	2.4	3.2	29.6	20.2
Spectrum 2	44.2	2.2	3.2	29.8	20.4
Spectrum 3	43.9	4.4	3.2	28.4	19.8
Spectrum 4	44.2	3.4	3.4	28.7	20.1
Spectrum 5	44.3	2.8	3.4	29.2	20.0
Spectrum 6	44.1	2.7	3.2	29.5	20.2
Spectrum 7	44.0	3.2	3.5	29.3	19.8
Spectrum 8	44.2	2.8	3.4	29.6	19.8
Spectrum 9	44.1	3.1	3.4	29.7	19.5
Spectrum 10	43.8	3.2	3.5	30.0	19.3
Spectrum 11	43.4	3.6	3.4	30.1	19.2
Spectrum 12	43.6	2.9	3.6	31.1	18.6
Spectrum 13	41.0	8.1	3.4	29.8	17.4
Spectrum 14	43.3	3.0	3.6	31.8	18.0
Spectrum 15	43.8	2.6	3.5	32.1	17.7
Spectrum 16	43.3	3.1	3.7	32.3	17.4
Spectrum 17	43.3	3.1	3.7	32.6	17.0
Spectrum 18	43.4	2.6	3.9	33.3	16.5
Spectrum 19	43.4	2.8	3.7	33.6	16.2
Spectrum 20	43.0	2.9	4.1	34.4	15.4
Spectrum 21	43.3	2.4	4.0	34.9	15.2
Spectrum 22	42.8	2.9	4.1	35.6	14.4
Spectrum 23	42.7	2.7	4.3	36.3	13.8
Spectrum 24	42.8	2.3	4.6	37.1	13.0
Spectrum 25	42.6	2.8	4.7	37.6	12.1
Spectrum 26	42.9	2.6	4.8	38.0	11.5
Spectrum 27	42.6	2.6	5.0	38.9	10.7
Spectrum 28	42.3	2.4	5.1	40.4	9.5
Spectrum 29	42.5	2.5	5.4	41.1	8.3
Spectrum 30	41.3	2.5	5.8	43.1	7.1
Spectrum 31	42.4	2.3	5.6	42.1	7.4

Table 5.8: Actual EDX analysis of the high Pt coating after oxidation for 15 hours at 1100°C. Values given are atomic%.

Spectrum	Al	Cr	Co	Ni	Pt
Spectrum 1	40.1	2.8	4.0	37.7	15.1
Spectrum 2	40.4	2.8	4.1	37.3	15.2
Spectrum 3	40.2	2.7	4.0	37.6	15.30
Spectrum 4	40.3	2.9	4.1	37.4	15.1
Spectrum 5	40.1	2.6	4.0	37.9	15.2
Spectrum 6	40.1	2.7	4.1	38.1	14.7
Spectrum 7	40.1	2.8	4.2	38.1	14.5
Spectrum 8	40.0	2.7	4.3	38.5	14.2
Spectrum 9	40.6	3.0	4.3	38.0	13.8
Spectrum 10	40.3	2.9	4.5	38.6	13.5
Spectrum 11	40.1	2.8	4.5	39.3	13.1
Spectrum 12	40.3	2.7	4.6	39.5	12.6
Spectrum 13	40.1	2.7	4.5	40.0	12.4
Spectrum 14	40.0	2.8	4.5	40.7	11.8
Spectrum 15	39.4	2.7	4.9	41.3	11.5
Spectrum 16	39.7	2.6	5.1	41.5	10.9
Spectrum 17	39.4	3.0	5.0	42.2	10.2
Spectrum 18	39.5	2.7	5.0	42.5	10.1
Spectrum 19	39.6	3.0	5.1	42.5	9.6
Spectrum 20	39.2	2.7	5.4	43.6	8.9
Spectrum 21	39.5	2.7	5.4	43.5	8.6
Spectrum 22	38.9	2.7	5.5	44.8	7.9
Spectrum 23	39.1	2.8	5.7	44.9	7.3
Spectrum 24	38.5	2.8	5.9	45.8	6.6
Spectrum 25	38.5	2.9	5.9	46.46	6.0

Table 5.9: Actual EDX analysis of the high Pt coating after oxidation for 20 hours at 1100°C. Values given are atomic%.

Spectrum	Al	Cr	Co	Ni	Pt
Spectrum 1	40.3	2.8	3.7	35.6	17.3
Spectrum 2	40.3	2.8	3.7	35.6	17.4
Spectrum 3	40.4	2.9	3.8	35.4	17.2
Spectrum 4	40.4	2.8	4.0	35.6	17.1
Spectrum 5	40.2	2.7	3.9	35.8	17.1
Spectrum 6	40.2	2.8	3.9	36.2	16.8
Spectrum 7	40.0	2.8	3.9	36.3	16.7
Spectrum 8	39.8	2.9	4.1	36.8	16.2
Spectrum 9	40.1	2.9	4.1	37.0	15.6
Spectrum 10	40.2	2.8	4.1	37.1	15.4
Spectrum 11	39.9	2.7	4.3	37.9	15.0
Spectrum 12	39.9	2.9	4.4	38.0	14.5
Spectrum 13	39.9	2.8	4.4	38.7	14.0
Spectrum 14	39.7	2.8	4.5	39.2	13.5
Spectrum 15	39.5	2.7	4.9	39.8	12.9
Spectrum 16	39.4	2.7	4.8	40.5	12.3
Spectrum 17	39.3	2.7	5.0	41.3	11.5
Spectrum 18	39.3	2.7	5.0	42.2	10.7
Spectrum 19	39.6	2.7	5.1	42.3	10.1
Spectrum 20	39.3	2.8	5.2	42.7	9.7
Spectrum 21	39.4	2.8	5.5	42.9	9.2
Spectrum 22	38.9	2.7	5.6	44.2	8.3
Spectrum 23	39.0	2.9	5.5	44.8	7.5
Spectrum 24	38.3	2.8	5.7	45.6	7.3
Spectrum 25	39.0	2.9	5.7	45.4	6.8

Table 5.10: Actual EDX analysis of the high Pt coating after oxidation for 25 hours at 1100°C. Values given are atomic%.

Spectrum	Al	Ti	Cr	Co	Ni	Ta	W	Re	Pt
Spectrum 1	31.4	1.0	4.6	7.2	53.2	nd	nd	nd	2.2
Spectrum 2	30.9	0.9	5.0	7.5	52.8	nd	0.4	nd	2.1
Spectrum 3	30.4	1.0	4.9	7.4	53.4	nd	0.7	nd	2.0
Spectrum 4	29.8	1.5	5.0	7.7	52.9	nd	1.0	nd	1.7
Spectrum 5	29.9	1.2	4.8	7.5	53.8	nd	0.8	nd	1.8
Spectrum 6	28.6	1.1	6.3	8.4	51.9	nd	1.7	nd	1.6
Spectrum 7	30.3	1.1	5.4	8.2	52.2	nd	0.9	nd	1.6
Spectrum 8	27.5	1.0	8.5	10.0	48.0	nd	3.3	nd	1.3
Spectrum 9	30.2	1.2	4.7	7.6	54.1	nd	0.5	nd	1.4
Spectrum 10	29.6	1.2	6.6	8.9	50.9	nd	1.4	nd	1.3
Spectrum 11	30.8	1.2	5.4	8.1	52.9	nd	nd	nd	1.3
Spectrum 12	9.6	0.9	14.7	13.7	38.3	5.2	10.8	5.7	0.7
Spectrum 13	27.7	1.2	7.1	9.1	51.0	nd	2.4	nd	1.0
Spectrum 14	24.4	1.5	3.7	8.1	57.8	2.5	0.7	nd	0.9
Spectrum 15	8.8	1.4	9.9	12.4	50.1	5.2	7.7	3.6	0.4
Spectrum 16	13.7	2.2	2.7	9.4	64.4	5.7	1.1	nd	0.4
Spectrum 17	13.8	2.5	3.9	9.6	63.7	3.9	1.9	nd	0.2
Spectrum 18	13.1	2.3	3.8	9.3	64.1	4.7	2.0	nd	0.3
Spectrum 19	10.4	1.5	14.3	13.3	54.6	1.6	2.1	1.7	nd
Spectrum 20	13.6	1.9	7.2	10.0	62.8	1.9	2.1	nd	nd
Spectrum 21	14.2	1.7	5.8	9.0	64.6	2.3	1.9	nd	nd
Spectrum 22	12.8	1.4	8.9	10.3	61.1	2.0	2.2	0.8	nd
Spectrum 23	12.1	1.3	10.0	10.8	60.2	1.8	2.4	1.1	nd
Spectrum 24	13.1	1.3	7.5	9.8	63.9	1.8	2.2	nd	nd
Spectrum 25	10.8	1.2	11.3	11.6	59.6	1.6	2.4	1.2	nd

Table 5.11: Actual EDX analysis of the high Pt coating after oxidation for 50 hours at 1100°C. Values given are atomic%.

Spectrum	Al	Ti	Cr	Co	Ni	Ta	W	Re	Pt
Spectrum 1	32.7	nd	4.1	5.7	51.3	nd	nd	nd	6.0
Spectrum 2	32.7	nd	4.1	5.9	50.9	nd	nd	nd	6.1
Spectrum 3	32.7	nd	4.0	5.6	51.2	nd	nd	nd	6.2
Spectrum 4	32.6	nd	4.2	5.8	51.1	nd	nd	nd	6.2
Spectrum 5	32.7	nd	4.1	5.8	50.9	nd	nd	nd	6.2
Spectrum 6	32.5	nd	4.2	5.9	51.0	nd	nd	nd	6.2
Spectrum 7	32.9	nd	4.0	5.8	51.1	nd	nd	nd	6.0
Spectrum 8	32.8	nd	4.1	5.8	51.1	nd	nd	nd	6.0
Spectrum 9	32.9	nd	4.2	5.9	50.8	nd	nd	nd	5.9
Spectrum 10	32.6	nd	4.1	6.0	51.2	nd	nd	nd	5.9
Spectrum 11	32.5	nd	4.1	6.1	51.2	nd	nd	nd	5.8
Spectrum 12	32.8	nd	4.2	6.0	51.1	nd	nd	nd	5.7
Spectrum 13	32.5	nd	4.2	6.0	51.4	nd	nd	nd	5.6
Spectrum 14	32.4	nd	4.5	6.0	51.3	nd	nd	nd	5.5
Spectrum 15	31.7	nd	4.4	5.8	49.6	nd	2.7	nd	5.6
Spectrum 16	32.3	nd	4.2	6.2	51.7	nd	nd	nd	5.4
Spectrum 17	32.5	nd	4.3	6.2	51.5	nd	nd	nd	5.2
Spectrum 18	32.0	nd	4.3	6.3	51.9	nd	nd	nd	5.2
Spectrum 19	32.2	nd	4.3	6.4	51.9	nd	nd	nd	5.0
Spectrum 20	32.1	nd	4.2	6.4	52.0	nd	nd	nd	5.0
Spectrum 21	32.2	nd	4.2	6.5	52.1	nd	nd	nd	4.8
Spectrum 22	31.8	0.7	4.4	6.4	51.6	nd	nd	nd	4.7
Spectrum 23	31.8	0.9	4.3	6.6	51.6	nd	nd	nd	4.6
Spectrum 24	22.0	0.6	10.3	10.3	42.9	nd	7.0	2.7	3.8
Spectrum 25	31.3	0.9	4.4	6.6	52.2	nd	nd	nd	4.3
Spectrum 26	31.4	0.9	4.4	6.6	52.2	nd	nd	nd	4.2
Spectrum 27	31.5	0.9	4.4	6.6	52.2	nd	nd	nd	4.1
Spectrum 28	31.7	0.9	4.3	6.7	52.2	nd	nd	nd	3.9
Spectrum 29	31.2	1.0	4.8	7.0	51.9	nd	nd	nd	3.8
Spectrum 30	31.3	1.0	4.5	6.8	52.4	nd	nd	nd	3.7
Spectrum 31	27.3	0.8	7.9	9.1	47.4	nd	3.8	nd	3.3
Spectrum 32	31.4	0.9	4.7	7.1	52.2	nd	nd	nd	3.5
Spectrum 33	31.2	1.0	4.9	7.1	52.2	nd	nd	nd	3.4
Spectrum 34	20.0	0.9	10.9	11.5	43.2	nd	8.4	2.31	2.6
Spectrum 35	29.2	0.9	6.5	8.4	49.8	nd	2.0	nd	2.9
Spectrum 36	29.5	1.1	4.7	7.4	52.4	1.2	0.4	nd	2.9
Spectrum 37	26.1	1.0	8.0	9.7	48.2	nd	4.2	nd	2.5

Table 5.12: Actual EDX analysis of the high Pt coating after oxidation for 75 hours at 1100°C. Values given are atomic%.

Spectrum	Al	Ti	Cr	Co	Ni	Ta	W	Re	Pt
Spectrum 1	29.5	0.8	4.4	6.6	54.1	nd	nd	nd	4.2
Spectrum 2	30.0	0.8	4.7	6.7	53.3	nd	nd	nd	4.2
Spectrum 3	14.5	0.6	12.9	12.4	41.1	nd	13.1	3.3	1.8
Spectrum 4	29.8	0.9	4.6	6.8	53.5	nd	nd	nd	4.2
Spectrum 5	27.7	0.7	6.4	8.1	50.3	nd	2.5	nd	3.8
Spectrum 6	16.0	0.6	12.0	11.8	42.6	nd	11.3	2.7	2.5
Spectrum 7	29.9	0.9	4.7	6.8	53.3	nd	nd	nd	4.1
Spectrum 8	29.5	0.9	4.6	6.8	54.0	nd	nd	nd	3.9
Spectrum 9	29.9	0.9	4.8	6.9	53.2	nd	nd	nd	4.0
Spectrum 10	30.0	0.8	4.7	6.9	53.3	nd	nd	nd	4.1
Spectrum 11	29.7	0.8	4.8	6.9	53.4	nd	nd	nd	4.1
Spectrum 12	29.8	0.9	4.8	7.0	53.3	nd	nd	nd	4.0
Spectrum 13	29.6	0.9	4.7	6.9	53.6	nd	nd	nd	4.1
Spectrum 14	29.6	0.9	4.8	6.9	53.6	nd	nd	nd	3.9
Spectrum 15	29.8	0.8	4.8	7.0	53.3	nd	nd	nd	4.0
Spectrum 16	29.1	0.9	4.0	6.6	55.4	nd	nd	nd	3.7
Spectrum 17	26.9	0.7	8.2	9.2	47.3	nd	4.1	nd	3.2
Spectrum 18	30.1	0.9	5.3	7.4	52.2	nd	nd	nd	3.9
Spectrum 19	30.2	0.9	5.1	7.2	52.5	nd	nd	nd	3.8
Spectrum 20	30.1	0.9	4.9	7.0	53.0	nd	nd	nd	3.8
Spectrum 21	29.1	0.8	5.4	7.3	52.3	nd	1.1	nd	3.7
Spectrum 22	29.3	0.8	5.7	7.5	51.5	nd	1.2	nd	3.7
Spectrum 23	28.7	0.8	5.8	7.7	51.5	nd	1.6	nd	3.5
Spectrum 24	24.7	0.8	7.8	9.2	49.2	nd	5.1	nd	2.9
Spectrum 25	30.1	0.8	5.2	7.2	52.6	nd	nd	nd	3.8
Spectrum 26	24.7	0.7	7.7	9.1	49.9	nd	4.6	nd	3.0
Spectrum 27	23.9	0.7	9.6	10.3	46.0	nd	6.4	nd	2.7
Spectrum 28	27.6	1.0	4.8	7.2	56.0	nd	nd	nd	3.1
Spectrum 29	3.8	0.2	21.6	18.8	27.2	nd	23.1	5.0	nd
Spectrum 30	27.9	0.8	6.5	8.2	50.7	nd	2.2	nd	3.4
Spectrum 31	26.2	0.8	8.9	10.1	46.1	nd	4.6	nd	3.1
Spectrum 32	29.6	1.0	4.9	7.2	53.4	nd	nd	nd	3.6
Spectrum 33	29.7	0.9	5.2	7.3	53.0	nd	nd	nd	3.6
Spectrum 34	19.3	1.4	3.2	8.0	60.8	4.2	nd	nd	2.7

Table 5.13: Actual EDX analysis of the high Pt coating after oxidation for 100 hours at 1100°C. Values given are atomic%.

Chapter 6

Conclusions

A series of oxidation experiments where done on 2 different types of bond coat at 1100°C. The coatings differ in thickness as well as platinum content. These were examined to gain a better understanding of the influence of different bond coat phases on oxide formation on the low Pt specimens and to investigate oxidation kinetics and phase transformation in the high Pt specimens.

There are clearly different types of alumina growing, depending on the bond coat composition. Growth rate and comparison with literature, as well as indexing diffraction patterns, points towards the θ alumina growing on $\beta - NiAl$ on the low Pt specimens, though there are still uncertainties with regards to pattern interpretation. The growth rate is the same for the oxide growing on the high Pt zone of the high Pt specimens. The oxide scale on $\gamma' - Ni_3Al$ is much more complex, EDX analysis shows it to consist of 2 layers, the inner being alumina, the outer being either a type of spinel, possibly $(Ni, Co)Al_2O_4$, or γ-alumina. The diffraction patterns can be interpreted either way.

Voids form at the metal/oxide interface on the low Pt specimens due to vacancy congregation. This has been shown to be the case for the interface on $\beta - NiAl$ grains. If the metal/oxide interface is moving inwards however, the vacancies are destroyed and no voids can form, as can be observed at the interface on $\gamma' - Ni_3Al$. Other mechanisms for void formation have been taken into account, like volume reduction due to martensite transformation in the β-grains. These effects, however, do not account for the volume of

voids, even if they may be contributing.

Oxidation kinetics on the high Pt specimens clearly show that the oxide is not growing by a parabolic rate, but is characterised by a time exponent of 0.145. This may be due to θ to α transformation of the oxide.

The high Pt specimens and their development over different times at temperature seem to have shown a discrepancy with the experimental ternary Ni-Al-Pt diagram [6]. It was shown, that this was due to the 5 at % of chromium, that is present in the specimens. Chromium cannot be incorporated into the nickel end of the diagram, as can be done with many other elements. A quarternary system was therefore proposed, showing that chromium shrinks the single phase field for $\beta - NiAl$.

Future work

A lot of results for this study were negative ones. In order to get a better understanding of the mechanisms around high temperature oxidation of different phases within the same coating more detailed studies would have to be done.

1. More electron diffraction and photo-stimulated luminescence spectroscopy alongside EBSD needs to be done, in order to investigate the influence of crystal structure of the underlying bond coat phases.

Further more it needs to be stressed that there are to date no publications on the influence of chromium on the high-Pt end of the Ni-Al-Pt system. The results of this study would need to be expanded upon with extensive experiments.

1. Weight-gain measurements for high Pt specimens, as a second method to calculate their oxidation kinetics and compare them to the results presented here.

2. a series oxidation experiments on samples with different levels of chromium and platinum contents, to fully determine the single phase fields in the Ni-Al-Pt-Cr system presented in this study.

Bibliography

[1] N. Birks, G. Meier, and F. Pettit, "Introduction to the high temperature oxidation of metals," *Cambridge University Press*, 2006.

[2] J. Oudar, "Physics and chemistry of surfaces," *Blackie Academic and Professional*, 1975.

[3] P. Kofstad, "High temperature oxidation of metals, corrosion monograph series.," 1966.

[4] H. Hindam and D. Whittle, "Microstructure, adhesion and growth kinetics of protective scales on metals and alloys," *Oxidation of Metals*, vol. 18, no. 5-6, pp. 245 – 84, 1982/12/.

[5] H. Evans and M. Taylor, "Oxidation of high-temperature coatings," *Proceedings of the Institution of Mechanical Engineers, Part G (Journal of Aerospace Engineering)*, vol. 220, no. G1, pp. 1 – 10, 2006/02/.

[6] B. Gleeson, W. Wang, S. Hayashi, and D. Sordelet, "Effects of platinum on the interdiffusion and oxidation behavior of ni-al-based alloys," vol. 461-464, (Les Embiez, France), pp. 213 – 222, 2004.

[7] K. Bhattacharya, *Microstructure of Martensite*. 2003.

[8] P. Khadkikar, I. Locci, K. Vedula, and G. Michal, "Transformation to ni_5al_3 in a 63.0 at. pct ni-al alloy," *Metallurgical Transactions A (Physical Metallurgy and Materials Science)*, vol. 24A, no. 1, pp. 83 – 94, 1993.

[9] W. Kowalski, B. Grushko, D. Pavlyuchkov, and M. Surowiec, "A contribution to the al-pd-cr phase diagram," *Journal of Alloys and Compounds*, vol. 496, no. 1-2, pp. 129 – 134, 2010.

[10] "http://www.fiz-karlsruhe.de/icsd.html."

[11] F. Kroger, *The Chemistry of Imperfect Crystals*. 1964.

[12] S. Bose. 2007.

[13] C. Wagner, "Theory of tarnishing processes," *Zeitschrift fur Physikalische Chemie*, vol. 21, no. 1-2, pp. 25 – 41, 1933/04/.

[14] H. Evans, "Stress effects in high temperature oxidation of metals," *International Materials Reviews*, vol. 40, no. 1, pp. 1 – 40, 1995//.

[15] H. Evans, D. Norfolk, and T. Swan, "Perturbation of parabolic kinetics resulting from the accumulation of stress in protective oxide layers," *Journal of the Electrochemical Society*, vol. 125, no. 7, pp. 1180 – 5, 1978/07/.

[16] R. Wing, "White hot technology - a turbine revolution," *Materials World*, vol. 8, no. 3, pp. 10 – 12, 2000.

[17] S. Saunders and J. Nicholls, "Coatings and surface treatments for high temperature oxidation resistance," vol. 5, (UK), pp. 780 – 98, 1989/08/.

[18] H. Evans and M. Taylor, "Diffusion cells and chemical failure of mcraly bond coats in thermal-barrier coating systems," *Oxidation of Metals*, vol. 55, no. 1/2, pp. 17–34, 2001.

[19] A. Taylor and R. Floyd, "Constitution of nickel-rich alloys of nickel-chromium-aluminum system," *Institute of Metals – Journal*, vol. 81, no. Part 9, pp. 451 – 464, 1953.

[20] C. Leyens, J.-W. Van Liere, M. Peters, and W. Kaysser, "Magnetron-sputtered ti-cr-al coatings for oxidation protection of titanium alloys," *Surface and Coatings Technology*, vol. 108-109, no. 1-3, pp. 30 – 35, 1998.

[21] C. Leyens, M. Peters, and W. Kaysser, "Oxidation and protection of near-alpha titanium alloys," *Materials Science Forum*, vol. 251-254, no. part 2, pp. 769 – 776, 1997.

[22] H.-P. Martinz and M. Rieger, "High temperature oxidation resistant coatings on molybdenum," *Materials Science Forum*, vol. 251-254, no. part 2, pp. 761 – 768, 1997.

[23] J. Nicholls, N. Simms, S. Neseyif, C. Ponton, H. Evans, and M. Taylor, "Smart overlay coatings - concept and practice," *High Temperature Corrosion and Materials Chemistry*, vol. 99, no. 38, pp. 270 – 281, 2000.

[24] J. Nicholls, N. Simms, W. Chan, and H. Evans, "Smart overlay coatings - concept and practice," *Surface and Coatings Technology*, vol. 149, no. 2-3, pp. 236 – 244, 2002.

[25] A. Crouch and R. Dooley, "Mechanical integrity and protective performance of silica coatings.," *Corrosion Science*, vol. 16, no. 6, pp. 341 – 347, 1976.

[26] J. Nicholls, "Designing oxidation-resistant coatings," *JOM*, vol. 52, no. 1, pp. 28 – 35, 2000/01/.

[27] M. Taylor, W. Pragnell, and H. Evans, "Evidence for the formation of al-rich reservoir phases resulting from interdiffusion between mcraly coating and ni-based substrate," vol. 461-464, (Les Embiez, France), pp. 239 – 246, 2004.

[28] H. Evans and M. Taylor, "Diffusion cells and chemical failure of mcraly bond coats in thermal-barrier coating systems," *Oxidation of Metals*, vol. 55, no. 1-2, pp. 17 – 34, 2001/02/.

[29] V. Tolpygo, D. Clarke, and K. Murphy, "Oxidation-induced failure of eb-pvd thermal barrier coatings," *Surface and Coatings Technology*, vol. 146-147, pp. 124 – 131, 2001.

[30] H. Evans, "High temperature coatings: Protection and breakdown.," 2009.

[31] S. Hayashi, S. Ford, D. Young, D. Sordelet, M. Besser, and B. Gleeson, "-nipt(al) and phase equilibria in the ni-al-pt system at 1150 c," *Acta Materialia*, vol. 53, no. 11, pp. 3319 – 3328, 2005.

[32] G. Lehnert and H. Meinhardt, "Present state and trend of development of surface coating methods against oxidation and corrosion at high temperatures," *Electrodeposition and Surface Treatment*, vol. 1, no. 1, pp. 71 – 6, Sept. 1972. development;surface coating methods;oxidation;corrosion;high temperatures;protective coatings;cracking resistance;.

[33] P. Deb, D. Boone, and R. Streiff, "Platinum aluminide coating structural effects on hot corrosion resistance at 900c," vol. 3, (USA), pp. 2578 – 81, 1985/11/. Pt-Al;superalloy;structural effects;hot corrosion resistance;prealuminizing heat treatment;postcoating heat treatment;IN738;surface degradation;coating thickness;.

[34] J. Fountain, F. Golightly, F. Stott, and G. Wood, "Influence of platinum on the maintenance of alpha -al2o3 as a protective scale.," *Oxidation of Metals*, vol. 10, no. 5, pp. 341 – 345, 1976.

[35] Y. Zhang, W. Lee, J. Haynes, I. Wright, B. Pint, K. Cooley, and P. Liaw, "Synthesis and cyclic oxidation behavior of a (ni,pt)al coating on a desulfurized ni-base superalloy," *Metallurgical and Materials Transactions A (Physical Metallurgy and Materials Science)*, vol. 30A, no. 10, pp. 2679 – 87, 1999/10/.

[36] Y. Zhang, J. Haynes, W. Lee, I. Wright, B. Pint, K. Cooley, and P. Liaw, "Effects of pt incorporation on the isothermal oxidation behavior of chemical vapor deposition aluminide coatings," *Metallurgical and Materials Transactions A (Physical Metallurgy and Materials Science)*, vol. 32A, no. 7, pp. 1727 – 41, 2001/07/.

[37] J. Haynes, B. Pint, K. More, Y. Zhang, and I. Wright, "Influence of sulfur, platinum, and hafnium on the oxidation behavior of cvd nial bond coatings," *Oxidation of Metals*, vol. 58, no. 5-6, pp. 513 – 544, 2002.

[38] H. Tawancy, N. Sridhar, N. Abbas, and D. Rickerby, "Comparative thermal stability characteristics and isothermal oxidation behavior of an aluminized and a pt-aluminized ni-base superalloy," *Scripta Metallurgica et Materialia*, vol. 33, no. 9, pp. 1431 – 8, 1995/11/01.

[39] H. Tawancy, N. Abbas, and T. Rhys-Jones, "Role of platinum in aluminide coatings," vol. 49, (Switzerland), pp. 1 – 7, 1991/12/10.

[40] H. Tawancy, N. Abbas, and T. Rhys-Jones, "Effect of substrate composition on the oxidation behavior of platinum-aluminized nickel-base superalloys," vol. 54-55, (Switzerland), pp. 1 – 7, 1992/11/16.

[41] H. Tawancy and L. M. Al-Hadhrami, "Role of platinum in thermal barrier coatings used in gas turbine blade applications," vol. 4, (Orlando, FL, United states), pp. 765 – 776, 2009. Aluminides;Aluminum oxides;Beta-phase;Bond coats;Ceramic coats;Ceramic top coat;Coating layer;Coating performance;Current technology;Detrimental effects;Electroplated layers;Gamma prime;Gas turbine blades;Interdiffusion;Metallic bonds;Metallic substrate;Microstructural features;Nickel base superalloy;Optical technique;Room temperature;Selective oxidation;Superalloy substrates;Surface layers;Thermal barrier coating systems;Thermal exposure;Thin layers;.

[42] K. A. Marino and E. A. Carter, "The effect of platinum on al diffusion kinetics in -nial: Implications for thermal barrier coating lifetime," *Acta Materialia*, vol. 58, no. 7, pp. 2726 – 2737, 2010.

[43] K. Marino and E. Carter, "The effect of platinum on defect formation energies in -nial," *Acta Materialia*, vol. 56, no. 14, pp. 3502 – 3510, 2008.

[44] E. Felten and F. Pettit, "Development, growth, and adhesion of al2o3 on platinum-aluminum alloys," *Oxidation of Metals*, vol. 10, no. 3, pp. 189 – 223, 1976/06/. growth;adhesion;morphologies;microstructures;oxidation rates;grain

boundaries;Al¡sub¿2¡/sub¿O¡sub¿3¡/sub¿ on Pt-Al alloys;corundum;1000 to 1450 degrees C;.

[45] D. Miracle, "The physical and mechanical properties of nial," *Acta Metallurgica et Materialia*, vol. 41, no. 3, pp. 649 – 84, 1993/03/.

[46] S. Rosen and J. Goebel, "Crystal structure of nickel-rich nial and martensitic nial," *Metallurgical Society of American Institute of Mining, Metallurgical and Petroleum Engineers – Transactions*, vol. 242, no. 4, pp. 722 – 724, 1968.

[47] Y. Zhang, J. Haynes, B. Pint, I. Wright, and W. Lee, "Martensitic transformation in cvd nial and (ni,pt)al bond coatings," *Surface and Coatings Technology*, vol. 163-164, pp. 19 – 24, 2003.

[48] M. Chen, M. Glynn, R. Ott, T. Hufnagel, and K. Hemker, "Characterization and modeling of a martensitic transformation in a platinum modified diffusion aluminide bond coat for thermal barrier coatings," *Acta Materialia*, vol. 51, no. 14, pp. 4279 – 94, 2003/08/15.

[49] E. Lesnikova and V. Lesnikov, "Influence of instability of the β - phase of the aluminide coating on the condition and scale resistance of the surface layer of ni-al alloys," *Metal Science and Heat Treatment*, vol. 28, no. 5-6, pp. 372 – 6, 1986/05/.

[50] D. Sordelet, M. Besser, R. Ott, B. Zimmerman, W. Porter, and B. Gleeson, "Isothermal nature of martensite formation in pt-modified β-nial alloys," *Acta Materialia*, vol. 55, no. 7, pp. 2433 – 41, 2007/04/.

[51] M. Ellner, U. Kattner, and B. Predel, "Constitutional and structural study of aluminium rich phases in the ni-al and pt-al systems," *Journal of the Less-Common Metals*, vol. 87, no. 2, pp. 305 – 25, 1982/10/.

[52] R. Suss, L. Cornish, and M. Witcomb, "Investigation of as-cast alloys in the pt-al-cr system," *Journal of Alloys and Compounds*, vol. 490, no. 1-2, pp. 124 – 144, 2010.

[53] R. Prescott and M. Graham, "The formation of aluminum oxide scales on high-temperature alloys," *Oxidation of Metals*, vol. 38, no. 3-4, pp. 233 – 54, 1992/10/.

[54] R. Klumpes, C. Maree, E. Schramm, and J. de Wit, "The influence of chromium on the oxidation of -nial at 1000c," *Materials and Corrosion*, vol. 47, no. 11, pp. 619 – 24, 1996/11/.

[55] S. Wilson, "Phase transformations and development of microstructure in boehmite-derived transition aluminas," *Proceedings of the British Ceramic Society*, no. 28, pp. 281 – 94, 1979/06/.

[56] I. Levin, T. Gemming, and D. Brandon, "Some metastable polymorphs and transient stages of transformation in alumina," *Physica Status Solidi A*, vol. 166, no. 1, pp. 197 – 218, 1998/03/16.

[57] R.-S. Zhou and R. Snyder, "Structures and transformation mechanisms of the n, and transition aluminas," *Acta Crystallographica, Section B (Structural Science)*, vol. B47, pp. 617 – 30, 1991/10/01.

[58] J. Yang, E. Schumann, I. Levin, and M. Ruehle, "Transient oxidation of nial," *Acta Materialia*, vol. 46, no. 6, pp. 2195 – 2201, 1998.

[59] H. Svensson, J. Angenete, and K. Stiller, "Microstructure of oxide scales on aluminide diffusion coatings after short time oxidation at 1050 c," *Surface and Coatings Technology*, vol. 177-178, pp. 152 – 157, 2004.

[60] M. Brumm and H. Grabke, "The oxidation behaviour of nial. i. phase transformations in the alumina scale during oxidation of nial and nial-cr alloys," *Corrosion Science*, vol. 33, no. 11, pp. 1677 – 90, 1992/11/.

[61] J. Doychak and M. Ruhle, "Tem studies of oxidized nial and ni3al cross sections," *Oxidation of Metals*, vol. 31, no. 5-6, pp. 431 – 52, 1989/06/.

[62] V. Tolpygo and D. Clarke, "Microstructural study of the theta-alpha transformation

in alumina scales formed on nickel-aluminides," vol. 17, (Cambridge, UK), pp. 59 – 70, 2000//.

[63] C. Guerre, R. Molins, and L. Remy, "Study of the coating stability of a tbc system," *Materials at High Temperatures*, vol. 17, no. 2, pp. 197 – 204, 2000.

[64] R. Molins and P. Hou, "Characterization of chemical and microstructural evolutions of a niptal bondcoat during high temperature oxidation," *Surface and Coatings Technology*, vol. 201, no. 7, pp. 3841 – 5, 2006/12/20.

[65] J. Chen and J. Little, "Degradation of the platinum aluminide coating on cmsx4 at 1100 c," *Surface and Coatings Technology*, vol. 92, no. 1-2, pp. 69 – 77, 1997.

[66] R. Molins, I. Rouzou, L. Remy, K. Le Biavant-Guerrier, and F. Jomard, "Study of sulfur distribution in a niptal bondcoat," *Materials at High Temperatures*, vol. 22, no. 3-4, pp. 359 – 66, 2005//.

[67] V. Tolpygo and D. Clarke, "Microstructural study of the theta-alpha transformation in alumina scales formed on nickel-aluminides," vol. 17, (UK), pp. 59 – 70, 2000//.

[68] H. Svensson, P. Knutsson, and K. Stiller, "Formation and healing of voids at the metal-oxide interface in nial alloys," *Oxidation of Metals*, vol. 71, no. 3, pp. 143 – 56, 2009/04/.

[69] N. Vialas and D. Monceau, "Substrate effect on the high-temperature oxidation behavior of a pt-modified aluminide coating. part 1: Influence of the initial chemical composition of the coating surface," *Oxidation of Metals*, vol. 66, no. 3-4, pp. 155 – 89, 2006/10/.

[70] L. Rivoaland, V. Maurice, P. Josso, M. Bacos, and P. Marcus, "The effect of sulfur segregation on the adherence of the thermally-grown oxide on nial-ii: the oxidation behavior at 900c of standard, desulfurized or sulfur-doped nial(001) single-crystals," *Oxidation of Metals*, vol. 60, no. 1-2, pp. 159 – 78, 2003/08/.

[71] J. Angenete, K. Stiller, and V. Langer, "Oxidation of simple and pt-modified aluminide diffusion coatings on ni-base superalloys - i. oxide scale microstructure," *Oxidation of Metals*, vol. 60, no. 1-2, pp. 47 – 82, 2003.

[72] M. Brumm and H. Grabke, "Oxidation behaviour of nial. ii. cavity formation beneath the oxide scale on nial of different stoichiometries," *Corrosion Science*, vol. 34, no. 4, pp. 547 – 61, 1993/04/.

[73] G. Tatlock, H. Al-Badairy, M. Bennett, and J. Nicholls, "Characterisation studies of chromia formation on commercial fecralre alloy foils following chemically induced failure at 900c," *Materials at High Temperatures*, vol. 22, no. 3-4, pp. 467 – 472, 2005.

[74] M. Martinez, B. Viguier, P. Maugis, and J. Lacaze, "Oxidation microstructure of iron aluminides," *Materials at High Temperatures*, vol. 22, no. 3-4, pp. 481 – 484, 2005.

[75] W. Pragnell, H. Evans, D. Naumenko, and W. Quadakkers, "Aluminium depletion in fecraly steel during transitional alumina formation," *Materials at High Temperatures*, vol. 22, no. 3-4, pp. 561 – 6, 2005//.

[76] M. Jackson and J. Rairden, "Protective coatings for superalloys and the use of phase diagrams," vol. 1, (USA), pp. 423–439, 1978.